Nanoparticle-based semiconductor solids: from synthesis to consolidation

by

Mariano Calcabrini

April, 2023

A thesis submitted to the
Graduate School
of the
Institute of Science and Technology Austria
in partial fulfillment of the requirements
for the degree of
Doctor of Philosophy

Committee in charge:

Paul Schanda, Chair

Georgios Katsaros

Maksym Yarema

Maria Ibáñez

The thesis of Mariano Calcabrini, titled *Nanoparticle-based semiconductor solids: from synthesis to consolidation*, is approved by:

Supervisor: Maria Ibáñez, ISTA, Klosterneuburg, Austria

Signature: _____

Committee Member: Georgios Katsaros, ISTA, Klosterneuburg, Austria

Signature: _____

Committee Member: Maksym Yarema, ETH Zürich, Zürich, Switzerland

Signature: _____

Defense Chair: Paul Schanda, ISTA, Klosterneuburg, Austria

Signature: _____

Signed page is on file

ISTA Thesis, ISSN: 2663-337X

ISBN: 978-3-99078-028-2

I hereby declare that this thesis is my own work and that it does not contain other people's work without this being so stated; this thesis does not contain my previous work without this being stated, and the bibliography contains all the literature that I used in writing the dissertation.

I declare that this is a true copy of my thesis, including any final revisions, as approved by my thesis committee, and that this thesis has not been submitted for a higher degree to any other university or institution.

I certify that any republication of materials presented in this thesis has been approved by the relevant publishers and co-authors.

Signature: _____

Mariano Calcabrini

April, 2023

Signed page is on file

Abstract

High-performance semiconductors rely upon precise control of heat and charge transport. This can be achieved by precisely engineering defects in polycrystalline solids. There are multiple approaches to preparing such polycrystalline semiconductors, and the transformation of solution-processed colloidal nanoparticles is appealing because colloidal nanoparticles combine low cost with structural and compositional tunability along with rich surface chemistry. However, the multiple processes from nanoparticle synthesis to the final bulk nanocomposites are very complex. They involve nanoparticle purification, post-synthetic modifications, and finally consolidation (thermal treatments and densification). All these properties dictate the final material's composition and microstructure, ultimately affecting its functional properties. This thesis explores the synthesis, surface chemistry and consolidation of colloidal semiconductor nanoparticles into dense solids. In particular, the transformations that take place during these processes, and their effect on the material's transport properties are evaluated.

About the author

Mariano Calcabrini was born in Quilmes, Argentina. He completed his studies in Chemical Sciences at the University of Buenos Aires in 2017 and graduated with honors. During his Master's degree, he worked on the sol-gel processing of silica nanoparticles and gels. In 2018, he joined the Ibáñez group at ISTA as a Ph.D. candidate studying colloidal nanoparticles and their application in solid-state chemistry.

Acknowledgements

The past years have been particularly intense for me, owing not only to the global situation but also to personal reasons. Nevertheless, I made the most out of them: I got to know amazing people, travelled, learned languages (and a little of Chemistry and Physics), planted a few trees, baked a lot, and even found drinkable Austrian red wines. In the meantime, I spent my hours in the lab, working to make Nature a tiny bit more comprehensible.

That work is summarized here and would not have been possible without the help from others; they deserve acknowledgement.

Firstly, I want to express my gratitude to Maria Ibáñez, for her guidance, teachings and her particular view on Chemistry, which enormously enriched the research presented herein. To the fellow members of the Ibáñez group. In particular, to Magali Lorion, who kept the lab running seamlessly and proved to be invaluable to our work; to Seungho Lee, Tobias Kleinhanns and Christine Fiedler for their extensive help in the experiments and for making the long hours in the lab enjoyable; and to the other group members who collaborated with the research.

I am also grateful to those collaborators, professors and service unit members who contributed to my research and from whom I learned so much.

Finally, I want to thank my family and friends, Barbara Fillips and her family, for the unconditional support over these years.

Last but not least, it would be upmost unfair not to acknowledge the coffee machines, undoubtably the hardest workers in the Institute.

This thesis and the publications within were financially supported by ISTA and the Werner Siemens Foundation. Mariano Calcabrini has received funding from the European Union's Horizon 2020 research and innovation program under the Marie Skłodowska-Curie Grant Agreement no. 665385.

List of publications appearing in the thesis

The Introduction contains concepts and figures of the publication: "*Solution-Processed Inorganic Thermoelectric Materials: Opportunities and Challenges*". Christine Fiedler, Tobias Kleinhanns, Maria Garcia, Seungho Lee, Mariano Calcabrini, and Maria Ibáñez **Chem. Mater. 2022, 34, 19, 8471–8489.** MC's main contribution to this work was on discussing surface chemistry and nanoparticle characterization techniques, and describing the challenges in the field.

Chapter 1.1 contains the publication: '*Ligand Conversion in Nanocrystal Synthesis: The Oxidation of Alkylamines to Fatty Acids by Nitrate*'. Mariano Calcabrini, Dietger Van den Eynden, Sergi Sánchez Ribot, Rohan Pokratath, Jordi Llorca, Jonathan De Roo, and Maria Ibáñez **JACS Au, 2021 1 (11), 1898-1903**. The original observation of the unusual surface chemistry was done by MI and JDR. MC devised and conducted most of the experiments and characterization, drafted and corrected the manuscript with input from other authors.

Chapter 1.2 contains the publication: '*The Importance of Surface Adsorbates in Solution-Processed Thermoelectric Materials: The Case of SnSe*'. Yu Liu*, Mariano Calcabrini*, Yuan Yu, Aziz Genç, Cheng Chang, Tommaso Costanzo, Tobias Kleinhanns, Seungho Lee, Jordi Llorca, Oana Cojocaru-Mirédin, Maria Ibáñez **Adv. Mater., 2021, 33, 2106858**. (∗) YL and MC contributed equally to this work. While synthesis and material characterization were mainly performed by YL, MC proposed and conducted specific characterizations aimed to understand the observed phenomena and actively contributed to data discussion and interpretation. Drafting and correction of the manuscript was done by MC and MI with input from the other authors.

Chapter 2.1 contains the publication: '*Exploiting the Lability of Metal Halide Perovskites for Doping Semiconductor Nanocomposites*'. Mariano Calcabrini, Aziz Genç, Yu Liu, Tobias Kleinhanns, Seungho Lee, Dmitry N. Dirin, Quinten A. Akkerman, Maksym V. Kovalenko, Jordi Arbiol, and Maria Ibáñez. **ACS Energy Lett., 2021, 6, 2, 581–587**. The original observation of the doping effect of metal halide perovskites was done by MI. MC devised and conducted most of the experiments and characterizations, drafted and corrected the manuscript with input from other authors.

Chapter 2.2 contains the co-authored publication: '*Defect Engineering in Solution-Processed Polycrystalline SnSe Leads to High Thermoelectric Performance*'. Yu Liu, Mariano Calcabrini, Yuan Yu, Seungho Lee, Cheng Chang, Jérémy David, Tanmoy Ghosh, Maria Chiara Spadaro, Chenyang Xie, Oana Cojocaru-Mirédin, Jordi Arbiol, and Maria Ibáñez **ACS Nano, 2022, 16, 1, 78–88**. MC contributed to the data interpretation, discussions, correction and proof reading of this publication.

Table of contents

List of abbreviations and acronyms

APT: atom probe tomography

EBSD: electron backscatter diffraction

EDS: energy-dispersive X-ray spectroscopy

HRTEM: high-resolution transmission electron microscopy

ICP-OES: inductively coupled plasma optical emission spectroscopy

CBM: conduction band minimum

CCC: charge carrier concentration

KPFM: Kelvin probe force microscopy

NP: nanoparticle

NC: nanocrystal

NMR: nuclear magnetic resonance

PDF: powder diffraction file

PF: power factor

SEM: scanning electron microscopy

SPS: spark plasma sintering

STEM: scanning transmission electron microscopy

TEM: transmission electron microscopy

VBM: valence band maximum

XRD: X-ray diffraction

XPS: X-ray photoelectron spectroscopy

List of symbols

zT: material's figure of merit

σ: electrical conductivity

S: Seebeck coefficient or thermopower

T: temperature

κ: total thermal conductivity

$\kappa_{lattice}$: lattice contribution to the thermal conductivity

κ_{elec}: electronic contribution to the thermal conductivity

μ_{Hall}: Hall mobility

μ_w: weighted mobility

k_B: Boltzmann constant

E_b: height of the energy barrier for conduction

E_F: Fermi level

h: Plank's constant

e: electron charge

m_e: electrons mass

n: electron density, charge carrier concentration

p: hole density, charge carrier concentration

Introduction

The synthesis of semiconductor nanoparticles (NPs) with controlled size, shape, composition, surface chemistry, and crystalline phase has been progressing at an accelerating pace during the past two decades.[1–3] This has led to an increasing interest in using them to prepare nanocomposites, exploiting the properties that emerge at the nanoscale in macroscopic materials and devices.[4–6]

Among the different strategies to prepare NPs, solution processing is the one that has shown the best compromise between yield, cost, and control over the mentioned NP characteristics. While most reports on solution processed dense semiconducting nanocomposites focus on the low cost, the ability to control the NPs' features with high accuracy has been overseen.[4] As we presented in our recent perspective article, '*Solution-Processed Inorganic Thermoelectric Materials: Opportunities and Challenges*', NPs can be utilized as precursors with well-defined characteristics (namely of the inorganic core, surface and particle organization) that yield solids with targeted features upon consolidating at high temperatures and/or pressures (Figure I.1).

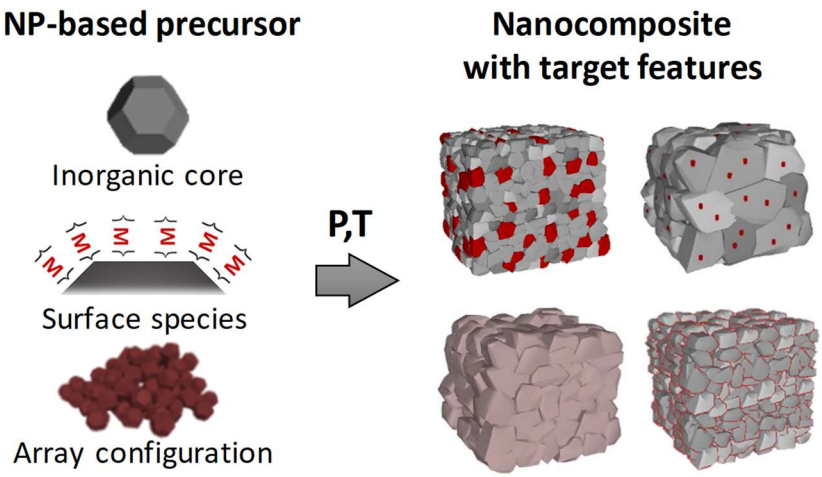

Figure I.1: Conceptual scheme showing different characteristics of the NP-based precursors and the solids with targeted features that could be obtained.

Colloidal NPs can be considered composed of an inorganic core and surface species, either organic or inorganic.[7] The inorganic core defines the most noticeable properties of NPs. For example, NP size, shape and crystal phase are determined by the inorganic core and, in the nanocomposite, these properties translate in distinct grain sizes, grain anisotropy and phases. Besides, the inorganic core of the NPs can be heterostructured or even have metastable crystal structures allowing the introduction of second phases in the final material or even the presence of phases not achievable in the bulk.[8–13]

Given the large surface-to-volume ratio of NPs, surface species are bound to have a strong influence on the final material.[27] The surface chemistry of the NPs is initially defined by the syntheses. 'Surfactant-assisted" syntheses use long, functionalized hydrocarbon surfactants

(ligands) to dissolve the precursors, control nucleation and growth, and to provide colloidal stability to the NPs.[14–16] These insulating surfactants remain bound to the NPs after purification.[17,18] Alternatively, they can be exchanged for other ions, complexes or molecules to further tune the material's structure and functional properties.[19,20] Otherwise, NPs can be synthesized by 'surfactant-free' methods.[21,22] In these cases, the surfaces are often considered 'naked', and the surface species are ignored. However, excess reagents, solvents and byproducts can adsorb on the NPs. As a remarkable example, in electrostatically stabilized colloidal NPs, the adsorption of counterions is unavoidable because the NPs are charged.[23] If such adsorbates do not decompose in the processing, they might remain in the dense polycrystalline semiconductors: inside the crystal lattice, on grain boundaries or forming second phases or nanoprecipitates.[24] On top of that, the surface can also be deliberately functionalized, creating new opportunities to modify the nanocomposite properties.[25,26]

Finally, the organization of the NPs before consolidation offers a further chance to conduct the transformation of the NPs and control the structure of the final solid. For instance, prior to the thermal treatments, NPs could be aligned, organized in layers, or arranged to have long range order.[28–30] By doing so NP sintering could be guided to achieve texturing, control porosity, adjust the distribution of second phases or even induce order in the final solids.

The tunability that colloidal NP precursors offer can be exploited to introduce different defects. Accordingly, by engineering the semiconductor nanocomposites' microstructure, their functional properties can be designed 'on-demand'.[31] On an atomic scale, point defects in the lattice can contribute to doping, scattering of short mean free path phonons, and modifying the bands structure among others. Grain boundaries and complexions, 2D defects, can scatter charge and heat carriers preferentially. And at last, bulk defects such as secondary phases, nanoprecipitates and pores play an important role in scattering long mean free path phonons, can introduce barriers for charge transport, or even have electronic effects. All together these defects contribute to adjusting the transport of phonons and charge carriers in the semiconductors. This is particularly relevant for thermoelectric materials; for other functional materials different properties might be optimized through microstructural control.

As a downside, the transformation of colloidal NPs into bulk nanocomposites is very complex, and understanding it is a difficult task. First, it involves the preparation of a NP powder: synthesis, purification steps to isolate them from unreacted species and side products, and surface treatments. Second, this NP powder needs to be consolidated: thermal treatments and densification methods are required to yield dense polycrystalline semiconductors (Figure I.2).

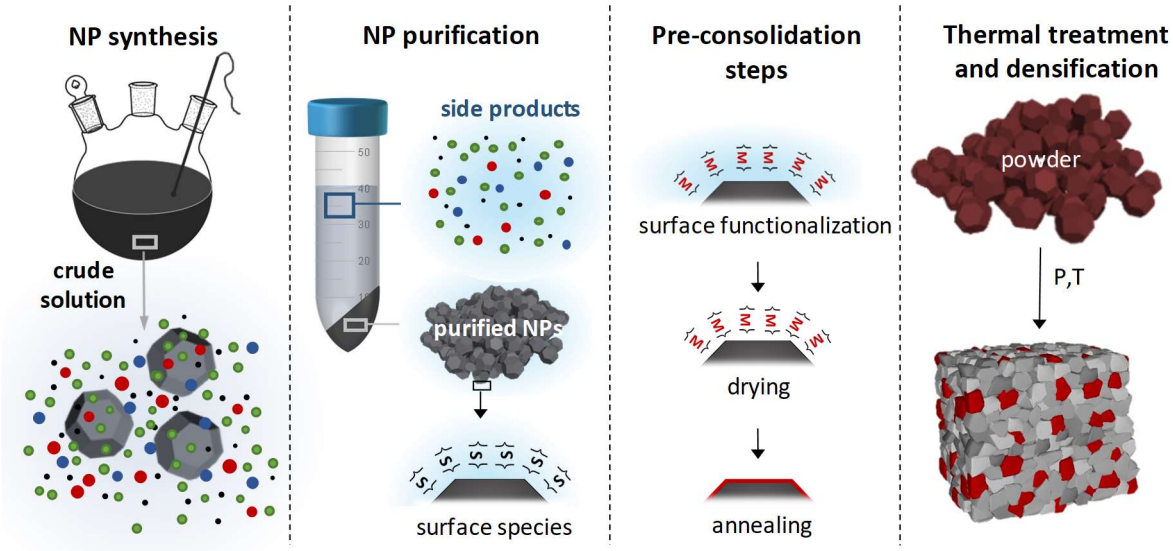

Figure I.2: The multiple steps involved from nanoparticle synthesis to the consolidation into dense polycrystalline solids.

True control of defects through this approach can only be achieved if every one of the steps of the process from synthesis to consolidation are well understood. This is quite challenging, it requires in-depth characterization of the NP precursors (both inorganic core and surface) as-synthesized and after subsequent treatments, the final material (composition, microstructure and transport properties) and, last but not least, of the physical and chemical transformations that take place in each step.

This thesis collects works done during the past years where I studied in detail the synthesis and surface chemistry of different colloidal NPs and further used them as precursors for dense polycrystalline semiconductors. By controlling some features in the nanocomposite such as grain size and the presence and distribution of defects and secondary phases, the semiconductors' electronic and thermal transport properties were successfully modified.

Chapter 1 – Synthesis and Surface Chemistry of Colloidal Nanoparticles

The most prominent advantage of using colloidal nanoparticles as building blocks for bulk nanocomposites is their high tunability of size, composition, morphology, crystal phase, and surface chemistry. These properties are generally defined during the synthesis and hence it is crucial to understand how the starting NPs are formed.

Colloidal nanoparticles can be synthesized in solution with or without surfactants. Both approaches are intensively used to prepare semiconductor nanocomposites. Surfactant-assisted syntheses use long chain organic ligands to dissolve the precursors, control nucleation and growth, and provide colloidal stability by binding to the surface of the NPs preventing their agglomeration (steric stabilization). Besides, surface ligands also affect the particle's chemical reactivity and electronic structure, potentially affecting the final nanocomposite.

Alternatively, syntheses that do not rely on surfactants, can yield colloidally stable particles if they are charged; when colloids of the same charge approach, they are subject to electrostatic repulsion and cannot aggregate (electrostatic stabilization). When such charged particles are removed from solution, counterions are co-precipitated to ensure charge neutrality. These counterions are often part of the semiconductor nanocomposite, altering its charge and heat transport properties among others.

In this chapter, I first present a study on the synthesis and surface chemistry of sterically stabilized metal oxide (CeO_{2-x}, ZnO, NiO, and In_2O_3) nanoparticles with unexpected surface chemistry. We investigate the synthesis of metal oxide nanoparticles from metal nitrate precursors in the presence of oleylamine ligands. Surprisingly, the nanoparticles are capped exclusively with a fatty acid instead of oleylamine. A detailed analysis of the reaction mixtures with nuclear magnetic resonance spectroscopy revealed several reaction byproducts and intermediates that are common to the decomposition of Ce, Zn, Ni and Zr nitrate precursors. Our evidence supports the oxidation of alkylamine and formation of a carboxylic acid, thus unraveling this counterintuitive surface chemistry. These findings addressed an important misconception regarding nanoparticle synthesis with amines, with implications for ligand exchange and colloid stability.

The second section of the chapter deals with the preparation of polycrystalline SnSe using a surfactant-free solution synthesis. In this study, we demonstrated that ionic adsorbates (Na^+) are electrostatically adsorbed on SnSe colloidal NPs synthesized in water and play a crucial role not only in directing the material nano/microstructure but also in determining the transport properties of the dense consolidated solid. These results highlight the importance of considering all the possible unintentional impurities to establish proper structure-property relationships and control material properties in solution-processed thermoelectric materials.

Both studies were published (JACS Au, 2021, 1, 1898−1903; Adv. Mater., 2021, 33, 52, 2106858) and are reproduced here with minor modifications.

1.1 Ligand Conversion in Nanocrystal Synthesis: The Oxidation of Alkylamines to Fatty Acids by Nitrate

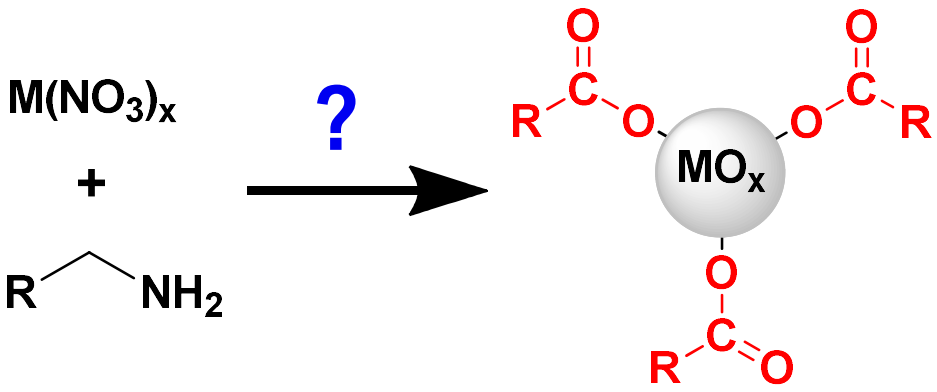

Ligand-assisted syntheses allow preparing colloidally stable nanocrystals (NCs) with controlled size,[32–34] shape,[35–38] and composition.[39–41] In these syntheses, long-chain aliphatic ligands are used to dissolve the precursors and control nucleation and growth.[1,2,7] After the syntheses, some ligands remain bound to the NC surface providing colloidal stability and determining solubility,[42,43] reactivity,[44–48] and electronic structure.[49–53] Therefore, unveiling the structure and binding motif of surface ligands is fundamental to understand NC properties,[54] design ligand exchange strategies,[48,55–58] and envision potential applications.[59,60]

In reactions where several organic ligands can bind to the NCs, the surface chemistry is typically studied in detail by nuclear magnetic resonance (NMR) spectroscopy, e.g., for CdSe,[56,61] PbS,[62–64] and InP[57,65,66] NCs. However, in reactions with only one type of ligand, the NC surface is often assumed to be capped by this particular ligand. Previously, this assumption was proven wrong, with trioctylphosphine oxide decomposing to phosphinic and phosphonic acid ligands during the synthesis of several metal oxides.[67]

In the present work, we disclose an even more extreme example, where alkylamine ligands are oxidized into carboxylic acids during the synthesis of CeO_{2-x} NCs from cerium nitrate. NMR has proved to be a powerful tool to understand reaction mechanisms in NC synthesis. For example, it has been used to explain the reduction of S with amines to prepare metal sulfide NCs,[68] and to unveil the role of H_2Se in the formation of CdSe NCs.[69,70] Here, we use various NMR techniques to investigate the intermediates and reaction byproducts, and propose a reaction path that we cross-examine with rigorous control experiments. We further analyzed the synthesis of other oxide NCs (NiO, ZnO and In_2O_3) from the corresponding nitrates and

found that the amine undergoes the same reactions. In a typical synthesis, $Ce(NO_3)_3{\cdot}6H_2O$ is dissolved under vacuum in oleylamine and 1-octadecene forming a complex, $[Ce(RNH_2)_n(NO_3)_3]$.[35,71] This complex thermally decomposes, yielding CeO_{2-x} NCs.

$$Ce(NO_3)_3 \cdot 6H_2O + n\,RNH_2 \xrightarrow{200°C} [Ce(NH_2R)_n(NO_3)_3]$$

$$[Ce(NH_2R)_n(NO_3)_3] \xrightarrow{300°C} CeO_{2-x} + N_2 + NO_x + ?$$

We use here *n*-octadecane instead of 1-octadecene, due the latter's tendency for spontaneous polymerization.[72] The purified NCs have a quasi-spherical shape, an average crystallite size of 6.5 nm, and a cubic crystallographic phase with space group Fm-3m (Figure 1.1.1).[35,73]

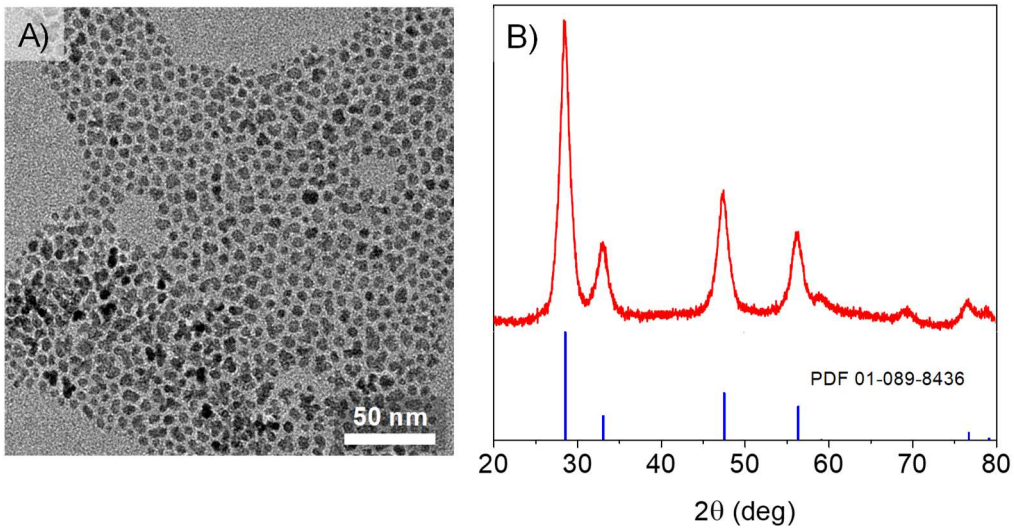

Figure 1.1.1. A) TEM micrographs of NCs synthetized with oleylamine in octadecane. B) Corresponding X-ray diffraction pattern of the NCs.

Using X-ray photoelectron spectroscopy (XPS) we determined that the particles have a composition $CeO_{1.74}$ (Table 1.1.1).[74] Furthermore, we performed thermogravimetric analysis of the NCs and found 15% wt. organics, corresponding to a ligand coverage of 3.3 ligands/nm^2, consistent with values reported for other oxide NCs.[42,75] The broad resonances in the ^{1}H NMR spectrum of the NCs indicate bound ligands (Figure 1.1.2).[76] However, the broadening also prevents their identification. To overcome this limitation, we treated the NCs with trifluoroacetic acid, which strips the original ligands from the surface.[35,40] The stripped ligands exhibit sharp resonances consistent with the fingerprint of a fatty acid (Figure 1.1.2). Especially the **α** resonance is diagnostic, aligning well with the **α** resonance of oleic acid (2.4 ppm) and clearly different from the **α** resonance of protonated oleylamine (2.7 ppm). The alkene resonance **ε** of the fatty acid reveals a mixture of *cis* and *trans* isomers, similar to that observed in commercial oleylamine,[77] suggesting that the acid is formed from the amine.[74]

Table 1.1.1. Atomic composition of the samples obtained from XPS

Ligands used/ sample treatment	C	N	O	Ce	$Ce^{(III)}/Ce^{(IV)}$	Formula
Dioctadecylamine	78.1	0.98	20.2	0.67	0.55	$CeO_{1.73}$
Hexadecylamine	61.2	0.34	36.8	1.67	0.53	$CeO_{1.74}$
Hexadecylamine exposed to air	58.2	0.59	39.1	2.12	0.52	$CeO_{1.74}$

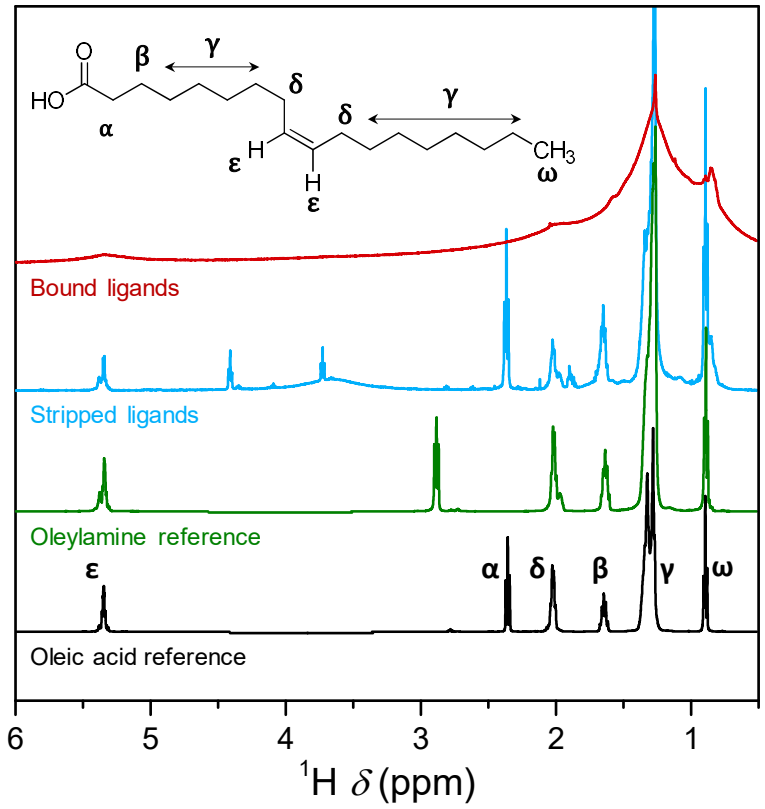

Figure 1.1.2. ^1H NMR spectra of purified NCs in benzene-d_6, the stripped ligands in $CDCl_3$ and the oleylamine and oleic acid references in $CDCl_3$ with additional trifluoroacetic acid added.

We set out to investigate the reaction path leading to the formation of the carboxylic acid. To avoid the reactivity of the double bond, we replaced oleylamine with hexadecylamine. This also simplifies the NMR spectra since hexadeylamine has no alkene resonance. The synthesis with hexadecylamine yields NCs with similar characteristics (size, shape, crystal structure). Also the NC surface is capped by a fatty acid, in this case palmitic acid (hexadecanoic acid) (Figure 1.1.3).

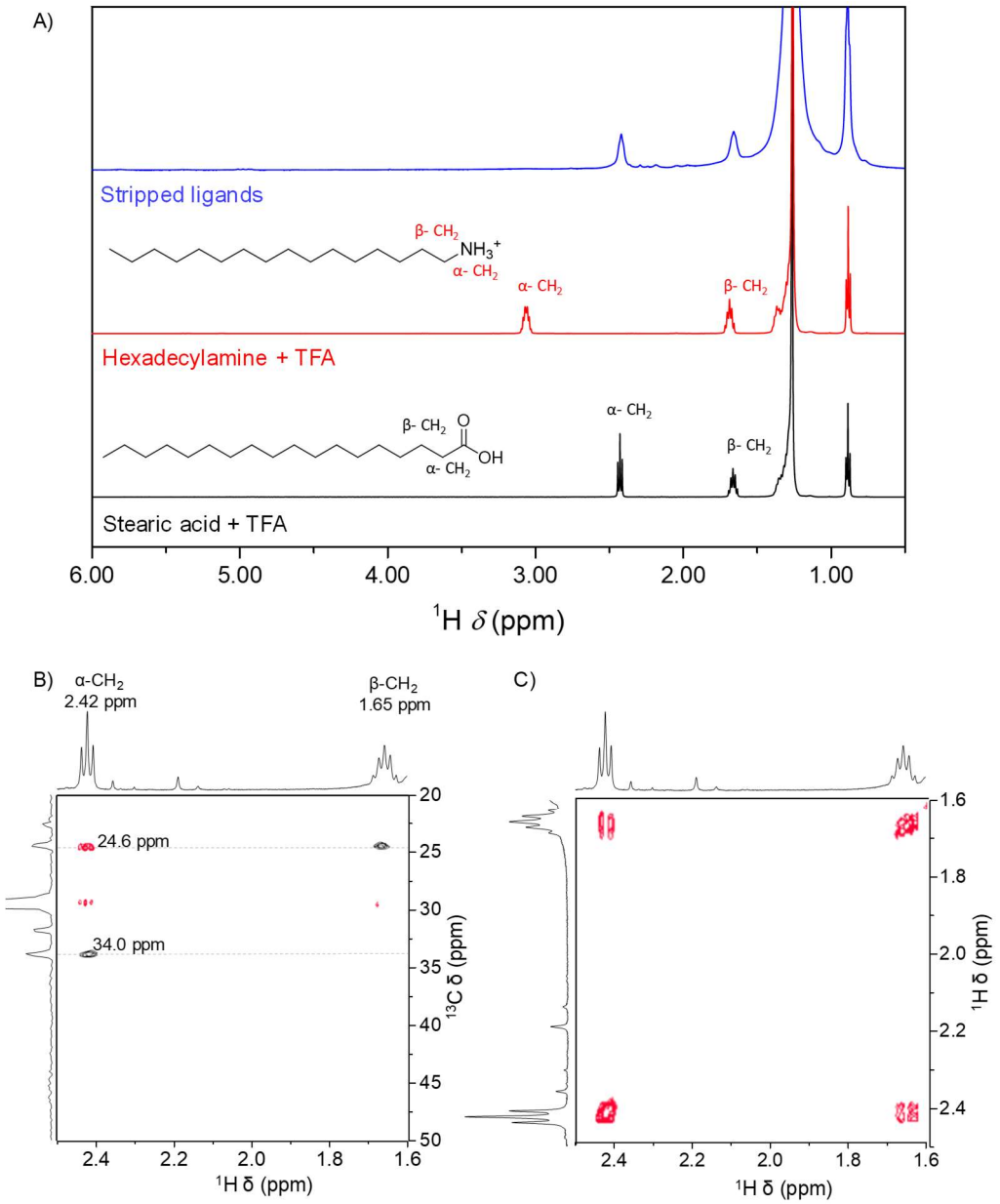

Figure 1.1.3. A) ^{1}H NMR spectra of ligands stripped from CeO_{2-X} nanocrystals in prepared with hexadecylamine (blue), protonated hexadecylamine (red) and protonated stearic acid (black) references in $CDCl_3$. B) HSQC (black) and HMBC (red) spectra of the stripped ligand indicating the chemical shifts of the α and β carbon atoms, and C) COSY spectra of the stripped ligand.

Figure 1.1.4 shows the ^{1}H NMR spectrum of the reaction mixture after completion of the synthesis. Besides the starting alkylamine and the solvent, twelve additional resonances are present in the ^{1}H NMR spectrum, labeled *A* to *M* in Figure 1.1.4. Using advanced NMR spectroscopy, we assigned the resonances to six different compounds derived from hexadecylamine. The reaction mixture contains a secondary aldimine (**6**, resonances *A*, *G* and *K*), a terminal alkene (**2**, resonances *B*, *E* and *M*), an amide (**9**, resonances *D*, *H* and *L*), an alcohol (**3**, resonance *F*), a nitrile (**5**, *J*) and yet unidentified compounds (resonances *C*, *I*). The identification of these compounds was further confirmed by adding either commercial or

synthesized reference compounds to the reaction mixture (spiking experiments). The road map for the assignments, together with the complete data set, can be found in the published manuscript.[74]

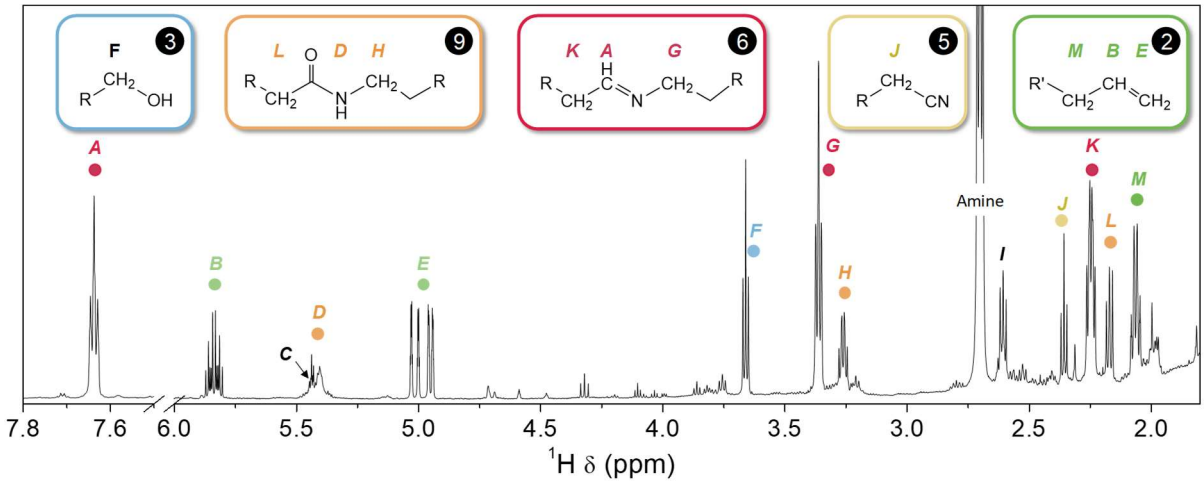

Figure 1.1.4. ^{1}H NMR spectrum of the reaction mixture of NCs prepared with hexadecylamine in octadecane after the completion of the synthesis (in $CDCl_3$). The most intense resonance, labeled 'amine', corresponds to hexadecylamine. Resonances *C* and *I* could not be assigned.

The scheme in Figure 1.1.5 illustrates our proposed reaction path from the alkylamine ligand into the different byproducts and intermediates. The different molecules are labeled **1**-**9**, and color-coded to indicate how these were identified. The amine **1** reacts with nitrates in different ways. The alkene **2** and alcohol **3** and are expected products for the decomposition of alkylamines complexed to metal nitrates, as they have been reported for the decomposition of methylamine and ethylamine copper (II) nitrate complexes.[78] The high reaction temperature could also promote the formation of the alkene **2** by β-elimination of the amine **1** under basic conditions.[79] However, in control experiments with oleylamine and $NaNO_3$ in octadecene the amine did not react suggesting that the formation of the alkene does not proceed through a simple elimination.

The formation of the other identified byproducts involves the oxidation of the amine group. For the formation of the secondary aldimine **6** and the nitrile **5**, we proposed an intermediate: the primary aldimine **4**. We hypothesize that **1** is oxidized to **4** by nitrate. Then, **4** can be further oxidized to the nitrile **5**, which is observed in the reaction mixture.[80] Furthermore, the primary aldimine **4** can condense with a second equivalent of amine **1** forming the more stable secondary aldimine **6.**[81,82] Aldimine **6** is observed in the reaction mixture and is also a common byproduct of the synthesis of nitrides.[83] The formation of **6** entails the evolution of ammonia, which we detected in the gas phase. The intermediate **4** cannot detected in the reaction mixture (Figure 1.1.4), which we attribute to the low stability of primary aldimines.[84] For the formation of the carboxylic acid **8** and the amide **9**, we propose aldehyde **7** as intermediate. This aldehyde is the oxidation product of the alcohol **3**,[78,85] or could be obtained by hydrolysis of either

aldimine with adventitious water.[84] The aldehyde **7** is further oxidized to the carboxylic acid **8**. Finally, the carboxylic acid **8** either binds to the NC surface or condenses with amine **1** to form amide **9,** explaining the absence of free carboxylic acid in the mixture.[86] Aldehyde **7** was not detected in the mixture but it appears as a logical intermediate. At the reaction temperature, it easily reacts with amine **1**, forming the secondary aldimine **6**.

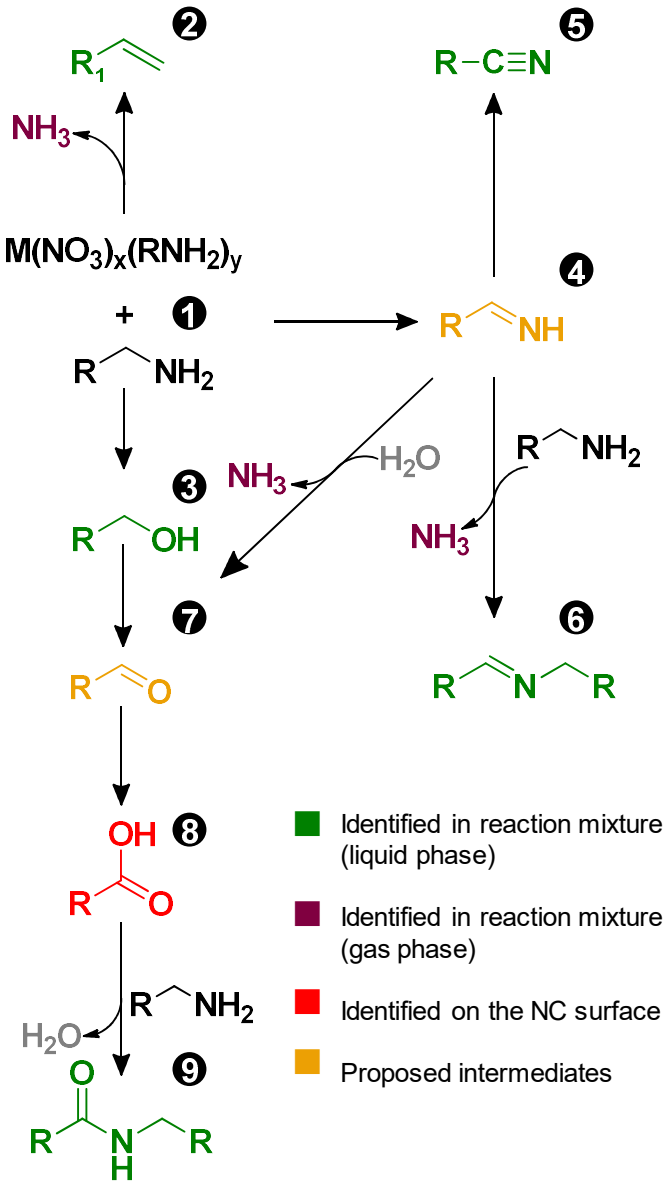

Figure 1.1.5. Proposed reaction path for the formation of carboxylic acid through the oxidation of alkylamines by nitrate

Further insights into the chemical transformations were obtained by analyzing aliquots of the reaction mixture taken at different reaction temperatures during the heating up process (Figures 1.1.6 and 1.1.7).

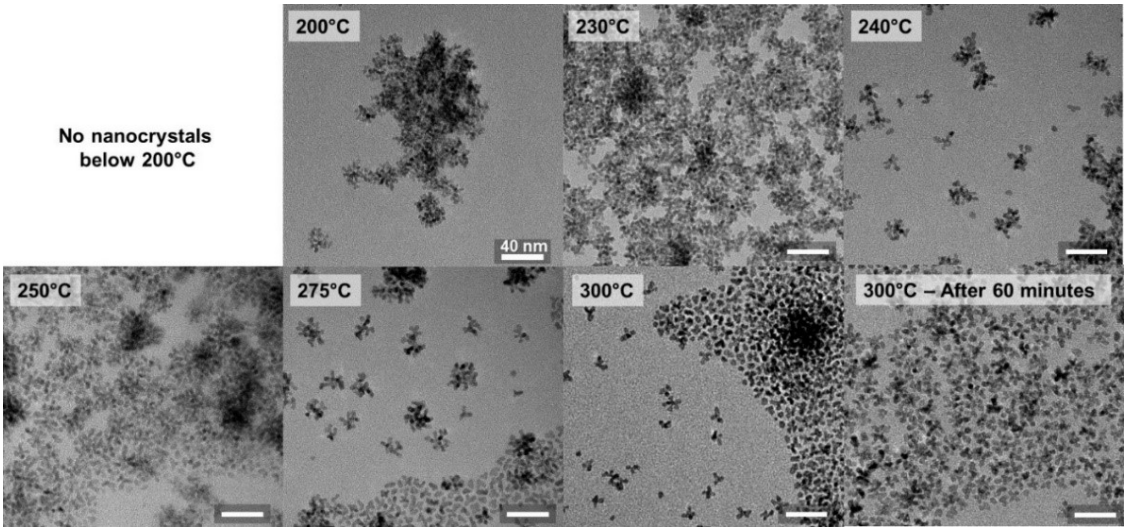

Figure 1.1.6. TEM micrographs of NCs found in aliquots taken at different times. The samples shown here are the same samples studied by NMR. No NCs were observed in aliquots taken below 200 °C. The reaction mixture changes color upon heating up from a light brown suspension at low temperatures to a dark brown solution and stops changing color at 240 °C. The NCs continue to grow until 300 °C.

We analyzed the aliquots by ^{1}H NMR and by transmission electron microscopy (TEM) to correlate the synthesis of the identified byproducts with the formation of the CeO_{2-x} NCs. We observed that at 100 °C the secondary aldimine **6** is already present, before any NCs and other bypodructs are formed (Figure 1.1.7).

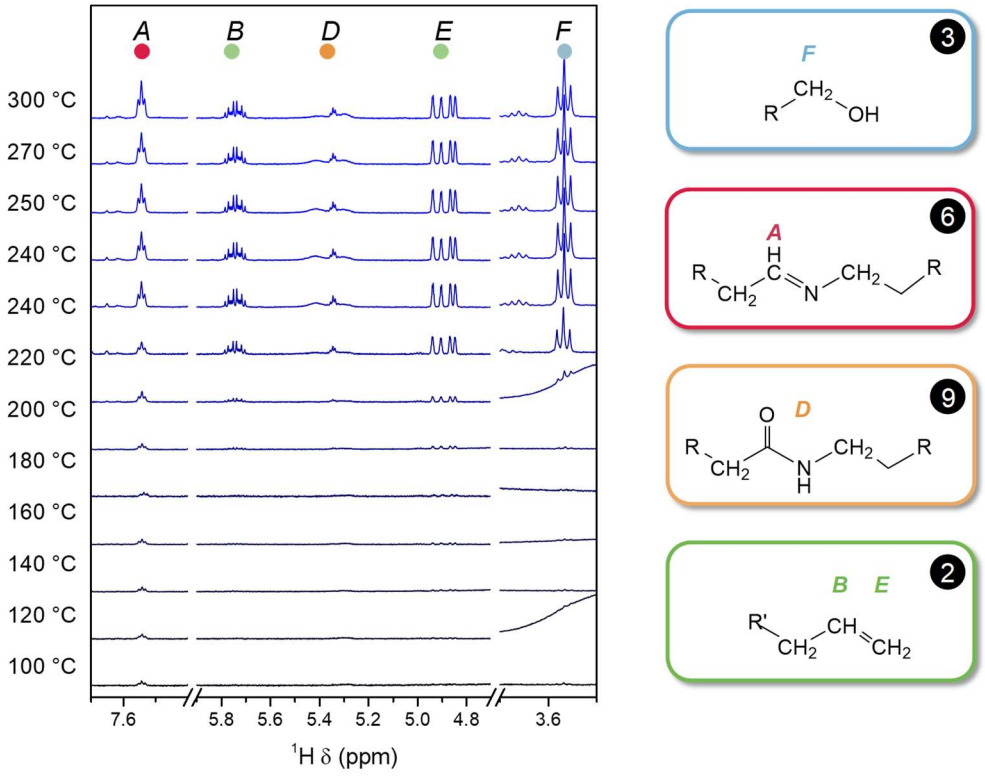

Figure 1.1.7. ^{1}H NMR spectra of aliquots of the reaction mixture in $CDCl_3$ taken at different temperatures during the heat-up. Broad resonances correspond to Ce(III) complexes.

This observation indicates that the formation of the secondary aldimine precedes the oxidation of the amine to alcohol, aldehyde, and carboxylic acid, and suggests that these molecules are formed through an independent path as proposed in Figure 1.1.5. The amide **9**, the alkene **2**, and the alcohol **3** appear only in measurable concentrations above 200 °C when the complex starts decomposing, indicated by strong gas evolution and a darkening of the solution. These changes happen simultaneously with the formation of the NCs, as revealed by TEM (Figure 1.1.6). As the temperature increases to 300 °C, the NCs grow, but no new resonances appear in the ^{1}H NMR spectrum of the reaction mixture (Figure 1.1.7), supporting the hypothesis of nitrate directly oxidizing the amine to alkene and alcohol. To validate the proposed reaction path, we studied the synthesis of CeO_{2-x} NCs using a secondary amine. NCs are still formed with N,N-dioctadecylamine and they have a quasispherical shape and similar size to those prepared with oleylamine. However, the second N-substituent on the ligand has two effects on the reaction path. Firstly, the oxidation of the secondary amine immediately results in the stable, secondary aldimine **6**. Since the primary aldimine **4** is not formed, oxidation to nitrile is prevented.

Secondly, N,N-dioctadecylamine has a more basic leaving group ($pK_bNH_3 > pK_bNH_2R$) and more steric hindrance than hexadecylamine. This severely hinders the formation of elimination and substitution products such as alkenes and alcohols. Indeed, we observe only a significant amount of secondary aldimine **6** in the reaction mixture with N,N-dioctadecylamine. Furthermore, the resulting NCs are capped by amine. To verify that the NCs synthesized with N,N-dioctadecylamine are acid-free, we studied the surface of the particles with XPS. Whereas the carboxylate features are clearly identified in the NCs synthesized with hexadecylamine, the ones synthesized with dioctadecylamine are acid free (Table 1.1.1). Despite the difference in surface chemistry, the change in the ligand used does not affect NCs' stoichiometry, which was determined to be $CeO_{1.73}$. The fact that we do not observe the fatty acid or the amide in the reaction mixture suggests that hydrolysis of the secondary aldimine **6**, is negligible under these conditions. Thus, the aldehyde **7** is most likely the direct oxidation product of the alcohol **3**, and the secondary aldimine does not react further to form the acid or amide.

Finally, to prove the generality of these results, we verified that the oxidation of amines by nitrate is not exclusive to the synthesis of CeO_{2-x} NCs. We decomposed Ni, Zn, Zr and In nitrates in the presence of alkylamines and to form NiO, ZnO and In_2O_3 NCs, and colloidally unstable ZrO_2 particles and found that in all cases, the composition of the reaction mixture is the same as for CeO_{2-x} and that, at least for ZnO NCs, the ligand shell is also composed only of carboxylic acid (Figure 1.1.8).

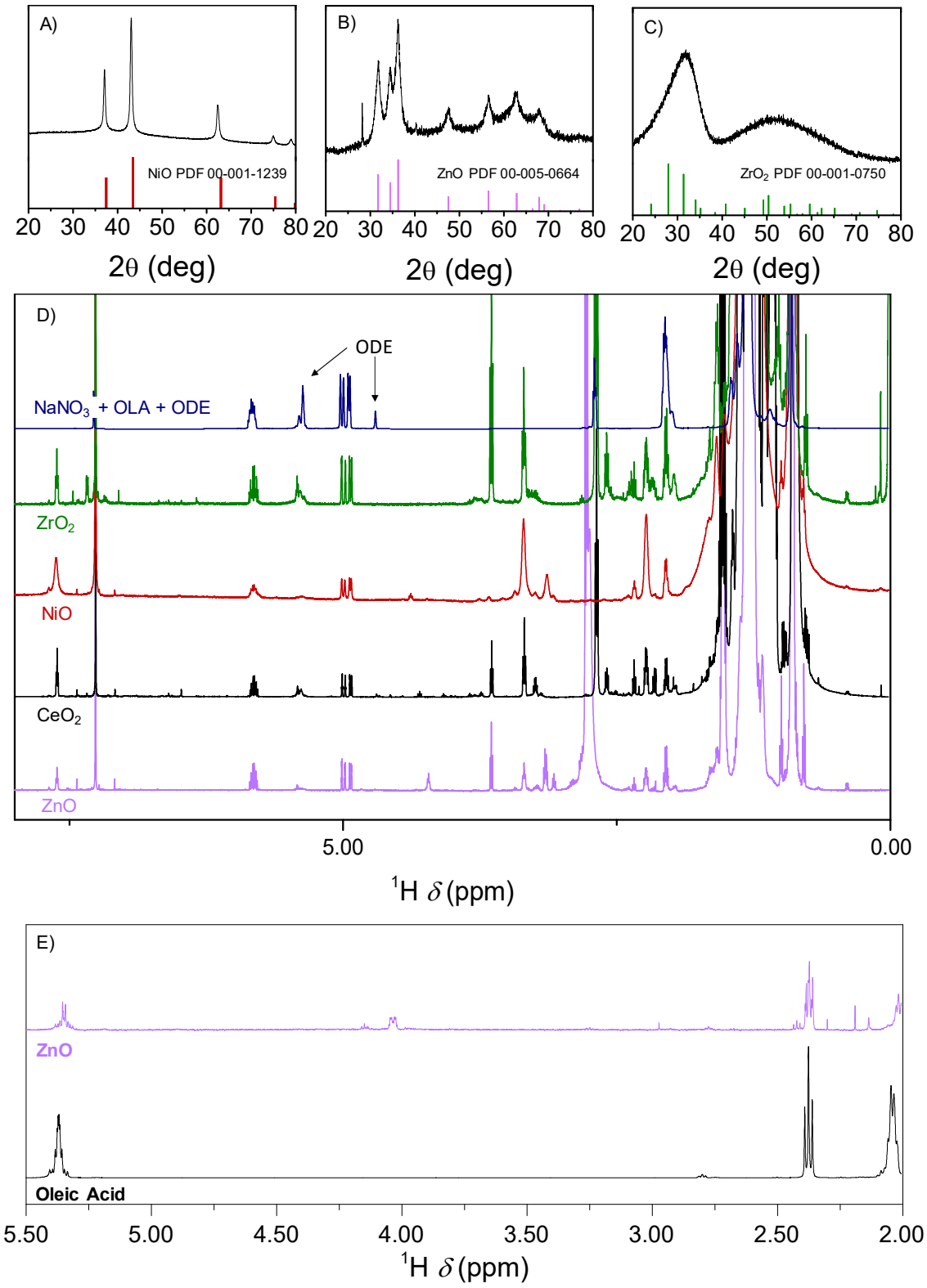

Figure 1.1.8. (A-C) XRD patterns of NiO, ZnO and ZrO_2 formed by the decomposition of the corresponding nitrates. (D) ^{1}H NMR spectra of the reaction mixtures with Zr, Ni, Ce and Zn nitrate precursors in $CDCl_3$. (E) ^{1}H NMR spectra of ligands stripped from ZnO NCs together with an oleic acid reference spectrum.

While there is precedent for alkylamines showing reactivity in NC synthesis (besides their function as ligand), the chemistry shown here is unique. Alkylamines have been used as reducing agents,[68,87,88] or as a source of ammonia.[83] Certain side reactions were reported, such as the oxidation to nitriles,[80,89,90] or the condensation with carboxylic acids.[86] However, none of these previously reported transformations yielded byproducts with high binding affinity for the NC surface. In this work, we show that alkylamines are oxidized by nitrate to carboxylic acids, thus producing *in situ* another potential ligand. This transformation completely alters the final NC surface chemistry since the ligand shell is only composed of carboxylate due to the higher binding affinity of carboxylates to metal oxide NCs, compared to amines.[55]

In summary, we scrutinized the synthesis of metal oxide NCs from metal nitrates in the presence of alkylamine ligands and revealed the oxidation of these amines with a comprehensive reaction scheme. We further proved that these reactions lead to the formation of carboxylic acids, which bind tightly to the NC surface, acting as the only capping ligand. Other NCs like metals and metal nitrides are also often synthesized from metal nitrates. Therefore, our current results might be relevant to understand these systems too.

The current section was adapted from the cited publication (JACS Au, 2021, 1, 1898–1903). Experimental details and supporting information that were not included in this chapter can be found there.

1.2 The Importance of Surface Adsorbates in Solution-Processed Thermoelectric Materials: The Case of SnSe

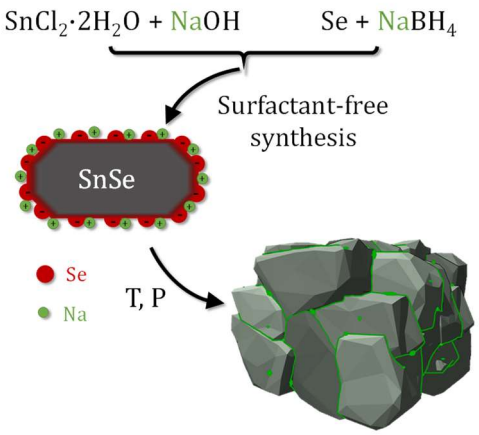

Thermoelectric devices reversibly convert heat into electricity both for power harvesting and for active cooling and heating. The efficiency of a thermoelectric device is determined by the temperature-dependent properties of the materials that constitute it. These are summarized in the thermoelectric figure of merit of each material, $zT = S^2 \sigma \kappa^{-1} T$, that combines Seebeck coefficient (S), electrical conductivity (σ), thermal conductivity (κ) and temperature (T).[4]

Thermoelectric materials are often dense, polycrystalline inorganic semiconductors. Usually, the processing of such materials has two steps: preparation of the semiconductor in powder form and the consolidation of the powder into a dense sample. The most common route to prepare powders among the thermoelectric community is through high-temperature reactions and ball milling.[91] Alternatively, solution methods to produce powders with much less demanding conditions (*e.g.* lower reagent purity, lower temperatures, shorter reaction times) have been explored to reduce the production costs.[4,92] These methods also provide opportunities to produce particles with better-controlled features, such as crystallite size, shape, composition, and crystal phase, which allow modifying the properties of the consolidated material.[8,14,93] Lastly, solution processing facilitates device fabrication versatility, including flexible, conformable, and rigid modules with customized geometries.[94,95] To date, solution synthesis has enabled the production of several materials with state-of-the-art performances, as is the case of PbS,[93] $Bi_{0.5}Sb_{1.5}Te_3$,[96] $Bi_2Te_{3-x}Se_x$,[97] and SnTe,[52] demonstrating the potential of this strategy.

However, when dealing with powders produced in solution, one should pay special attention to potential undesired elements coming from the reactants present as surface adsorbates.[98] The composition, chemical stability, and bonding nature of surface species can influence the sintering process, and reaction byproducts can determine the final properties of the consolidated material. Surface species have been carefully considered in surfactant-assisted colloidal synthesis because of the insulating nature of the long-chain aliphatic surfactants generally used[2] and the consequent detrimental effects on thermoelectric performance.[99] In those cases, the surfactants have to be removed to enhance the electrical conductivity. The most common strategy to do so is thermal decomposition.[17,18,58] Alternatively, surfactants can be

exchanged with volatile compounds[100] or even inorganic species[60] that can further tune material properties.[52,58,101] Conversely, the presence of surface adsorbates is usually neglected in the case of the so-called surfactant-free methods,[92,102–114] the most widely used to produce thermoelectric powders in solution. The vast majority of reports dealing with surfactant-free synthesis do not consider any surface treatments since the particles are considered 'naked'.[112,115,116] This is a misconception since different species might be adsorbed on the particle surface, depending on the particle composition and surface termination.[54,117–119] Such adsorbates need to be identified to unveil if they have a role in the thermoelectric properties.

In this work, we identify the surface species resulting from the aqueous synthesis of SnSe particles and demonstrate their effects on the microstructure and thermoelectric properties of the final material. While this work focuses on SnSe, one of the most studied thermoelectric materials due to its high performance, the presence of surface species in solution-processed materials goes beyond the specific material system and needs to be carefully evaluated to understand the material properties correctly.

The table below shows the most common reactants to synthesize SnSe powders in solution that lead to state-of-the-art performance (Table 1.2.1). SnSe particles are usually prepared in polar media (water or ethylene glycol, EG) using $SnCl_2$ and Se, SeO_2, or Na_2SeO_3 as precursors. Additionally, redox agents and acids or bases are used. Generally, these are Na salts, as highlighted in red in Table 1.2.1.

Table 1.2.1. Summary of the state-of-art thermoelectric performance of *p*-type doped polycrystalline SnSe prepared by consolidating solution-processed particles. The table includes the nominal composition of the consolidated material as reported by the authors, the reactants used, and peak zT values (zT_{max}). '∥' (parallel) and '⊥' (perpendicular) denote the direction with respect to the pressing axis in which the zT was measured.

Material	Precursors, solvent	zT_{max}
$Sn_{0.96}Ga_{0.04}Se$[102]	$SnCl_2{\cdot}2H_2O$, $GaCl_3$, ***NaOH***, Se, H_2O	2.2 (873 K, ∥)
$Sn_{0.98}Pb_{0.01}Zn_{0.01}Se$[109]	$SnCl_2{\cdot}2H_2O$, $PbCl_2$, $ZnCl_2$, ***NaOH***, Se, H_2O	2.2 (873 K, ∥)
$Sn_{0.95}Se$[107]	$SnCl_2{\cdot}2H_2O$, ***NaOH***, Se, H_2O	2.1 (873 K, ∥)
$Sn_{0.97}Ge_{0.03}Se$[92]	$SnCl_2{\cdot}2H_2O$, GeI_4, ***NaOH***, Se, H_2O	2.1 (873 K, ⊥)
$Sn_{0.99}Pb_{0.01}Se$-Se QDs[120]	$SnCl_2{\cdot}2H_2O$, $PbCl_2$, ***NaOH***, Se, H_2O	2.0 (873 K, ∥)
$Sn_{0.96}Pb_{0.01}Cd_{0.03}Se$[104]	$SnCl_2{\cdot}2H_2O$, $PbCl_2$, $CdCl_2$, ***NaOH***, Se, H_2O	1.9 (873 K, ∥)
$Sn_{0.948}Cd_{0.023}Se$[121]	$SnCl_2{\cdot}2H_2O$, $CdCl_2$, ***Na_2SeO_3***, ***NaOH***, EG	1.7 (823 K, ∥)
SnSe-4%$InSe_y$[122]	$SnCl_2{\cdot}2H_2O$, $InCl_3{\cdot}4H_2O$, ***Na_2SeO_3***, ***NaOH***, EG	1.7 (823 K, ∥)
SnSe-1%PbSe[105]	$SnCl_2{\cdot}2H_2O$, $PbCl_2$, ***NaOH***, Se, H_2O	1.7 (873 K, ∥)
NaOH-$Sn_{1-x}Se$[110]	$SnCl_2$, ***Na_2SeO_3***, ***NaOH***, EG	1.5 (823 K, ⊥)
$Sn_{0.882}Cu_{0.118}Se$[114]	$SnCl_2{\cdot}2H_2O$, $CuCl_2$, ***Na_2SeO_3***, ***NaOH***, EG	1.4 (823 K, ⊥)
SnSe-15%Te NWs[123]	$SnCl_2{\cdot}2H_2O$, ***$NaBH_4$***, ***NaOH***, Se, H_2O	1.4 (790 K, ∥)
$Sn_{0.98}Se$[111]	$SnCl_2{\cdot}2H_2O$, ***Na_2SeO_3***, ***NaOH***, EG	1.4 (823 K, ⊥)
$SnSe_{0.90}Te_{0.1}$[124]	$SnCl_2{\cdot}2H_2O$, ***Na_2SeO_3***, ***Na_2TeO_3***, ***NaOH***, EG	1.1 (800 K, ⊥)
$Sn_{0.99}Cu_{0.01}Se$[108]	$SnCl_2{\cdot}2H_2O$, CuCl, ***NaOH***, Se, H_2O	1.2 (873 K, ∥)
$SnSe_{0.9}S_{0.1}$[103]	$SnCl_2{\cdot}2H_2O$, ***Na_2S***, ***$NaBH_4$***, ***NaOH***, Se, H_2O	1.16 (923 K, ⊥)

We selected the simplest and most cost-effective synthetic method, which uses ambient pressure and water as the solvent,[113] as a prototypical reaction. In the chosen procedure, $NaBH_4$ is first dissolved in water, and Se powder is slowly added to form HSe^-. In parallel, NaOH and $SnCl_2{\cdot}2H_2O$ are dissolved in water, and the solution is heated to its boiling point. At this temperature, the freshly prepared Se-solution is rapidly injected. Upon injection, the reaction mixture turns black, indicating particle formation, and it is kept under reflux for two additional hours. The as-synthetized particles are purified by precipitation/redispersion alternating water and ethanol and then dried under vacuum overnight at room temperature. Afterwards, the powder is annealed in forming gas (5 % H_2 in N_2, 1 bar) to remove oxides species.[125] Finally, the annealed powders are consolidated into cylindrical pellets using spark plasma sintering (SPS). Throughout the process, X-ray diffraction (XRD) is used to verify that the product is pure phase orthorhombic SnSe and scanning electron microscopy (SEM) to evaluate the material morphology (Figure 1.2.1).

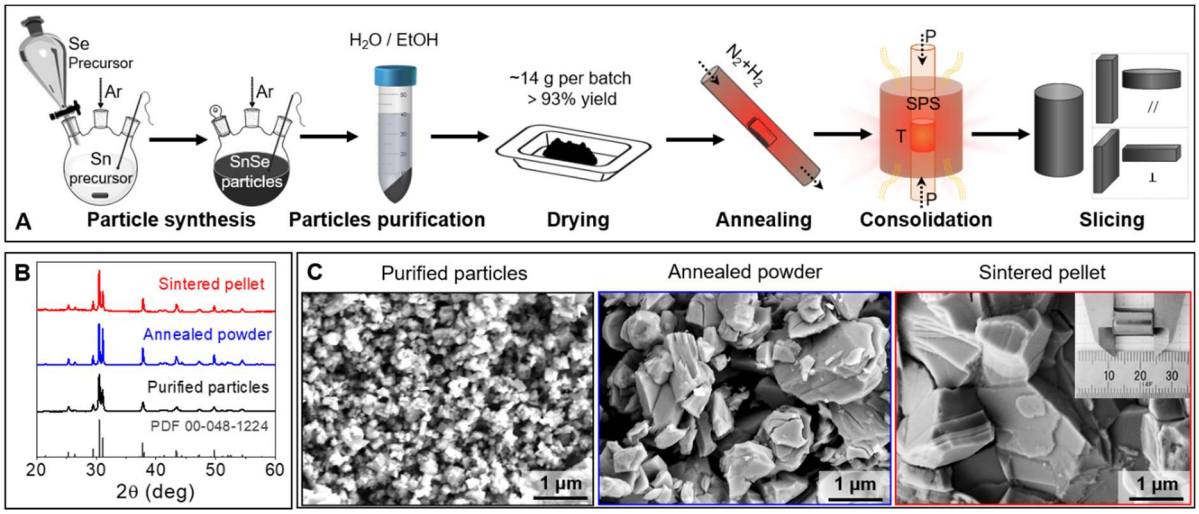

Figure 1.2.1. A) Scheme of the processing steps of SnSe pellets. B) XRD patterns of initial SnSe particles, annealed powder, and sintered pellet along the out-of-plane direction, including the reference PDF 00-048-1224. C) Corresponding representative SEM micrographs of the material in the different processing steps. The inset shows a dense SnSe cylindrical pellet.

We started this study by characterizing the as synthesized particles. SEM and transmission electron microscopy (TEM) images show that the particles have a rectangular shape with an average lateral size of *ca.* 150 ± 50 nm (Figure 1.2.1.C and Figure 1.2.2.A). High-resolution TEM (HRTEM) analysis confirmed the SnSe orthorhombic structure (space group *Pnma*) with lattice parameters a=11.52 Å, b=4.16 Å, and c=4.43 Å. Elemental analysis with energy-dispersive X-ray spectroscopy (EDS) in SEM and scanning transmission electron microscopy (STEM) indicated that the particles are slightly Se-rich and revealed the presence of Na (Figure 1.2.2.B).

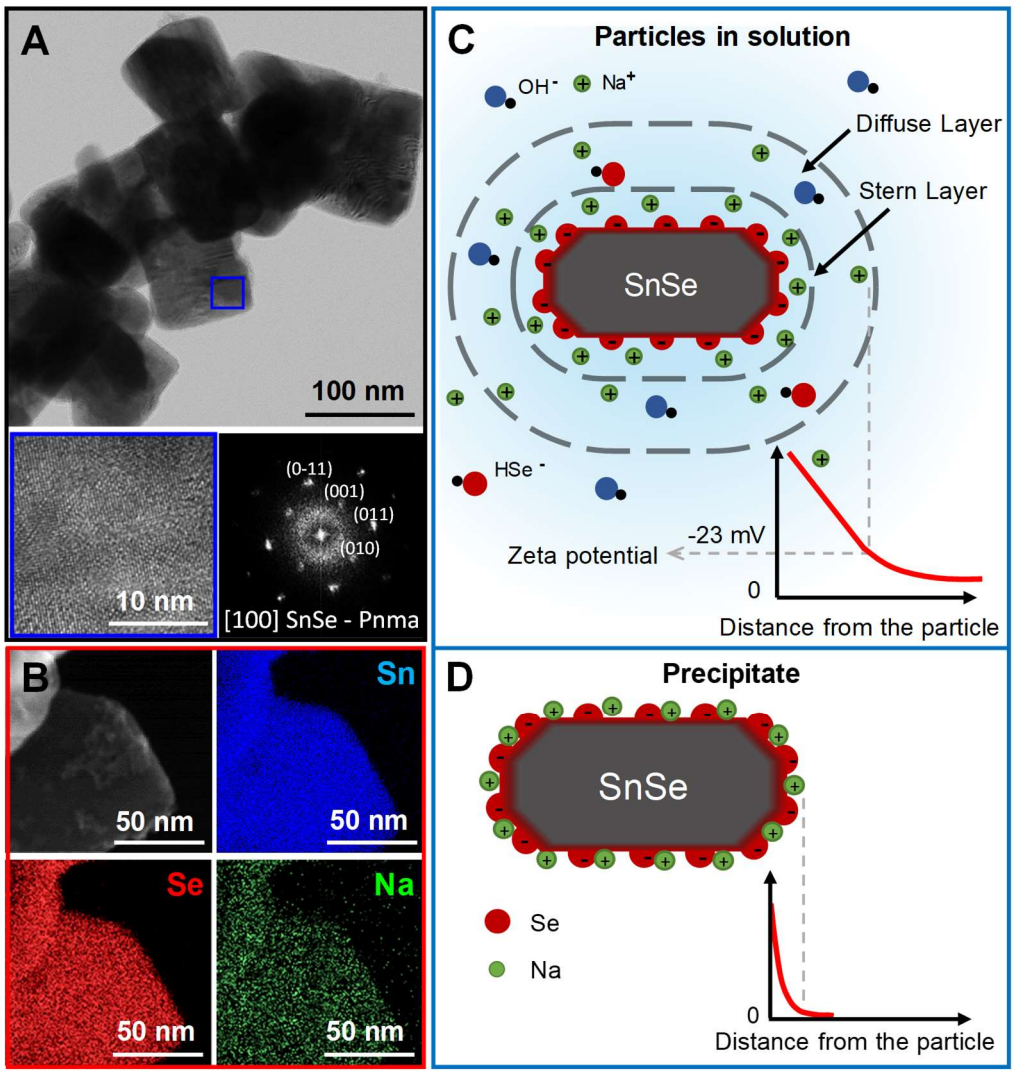

Figure 1.2.2. A) Bright-field TEM micrograph of several SnSe particles, HRTEM micrograph of the particle marked with a blue square, and its corresponding power spectrum. B) STEM-EDS elemental mapping of Sn (blue), Se (red), and Na (green) for SnSe particles. C) Schematic representation of the electrical double layer of a SnSe particle in solution based on the Stern model. D) Schematic representation of a precipitated particle with Na^+ ions adsorbed to promote charge neutrality.

The Na to Sn ratio determined by X-ray photoemission spectroscopy (XPS, Figure 1.2.3) is four times larger than that obtained from EDS, suggesting that Na is mainly at the particle surface, yet we cannot discard its presence within the SnSe particles. In the Se 3d XPS region, four peaks can be deconvoluted. These correspond to the $3d_{3/2}$ and $3d_{5/2}$ emission peaks of Se in two different oxidation states. Se^{2-}, from SnSe, is observed at low binding energies, while at higher energies, more oxidized Se species are present, with an oxidation state closer to 0.[126] We speculate that these species are polyselenides (Se_x^{2-}) formed by partial oxidation of the particle surface during washing, as observed for Cu_2Se nanoparticles.[127–129] During the synthesis, Na^+ ions compensate the charge of the reactive ions (OH^-, BH_4^-, HSe^-, *etc.*) but should not react based on their chemistry.[113] Therefore, we propose that Na^+ ions are adsorbed on the surface, explaining their presence in the particles. To verify this hypothesis and disclose the nature of the adsorption, we performed electrophoretic mobility measurements and determined that SnSe particles are negatively charged (zeta potential = -22 ± 5 mV, Figure 1.2.2.C) consistent

with their Se-rich surface. Based on the electric double layer description, the negatively charged SnSe particles are surrounded by an immobile layer, the Stern layer, of cations (Na^+) and a second layer of loosely bound ions, the diffuse layer, composed mostly of cations (Na^+) and some anions (OH^-, HSe^-).[130] Due to the electrostatic force, cations remain on the particle surface during washing, explaining the presence of Na once the particles are removed from the solution (Figure 1.2.2.D). Furthermore, compositional analysis with inductively coupled plasma - optical emission spectroscopy (ICP-OES) and EDS revealed that the pellets have *ca.* 1.6 at% Na. Such a large Na content, beyond its solubility limit,[131] confirms that Na^+ ions are adsorbed on the particle surface.

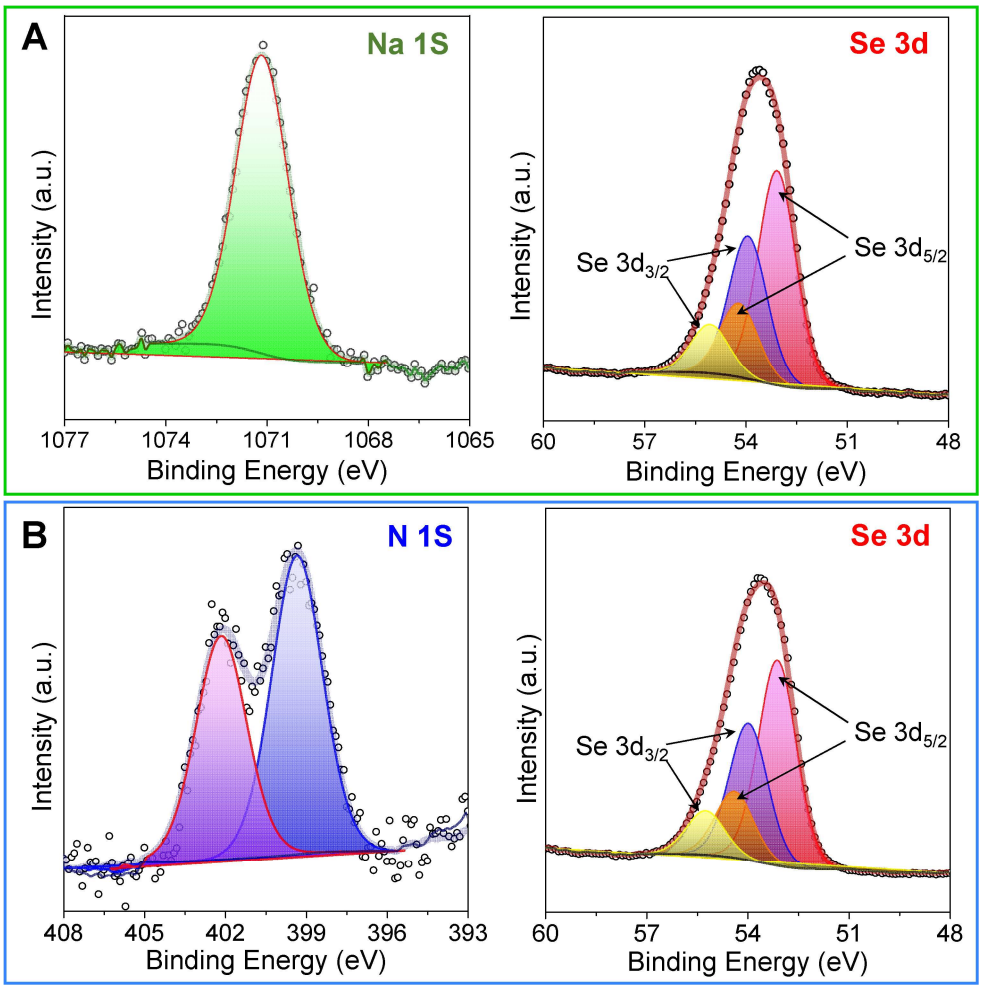

Figure 1.2.3. High resolution XPS spectra obtained from A) Na-SnSe particles and B) Me_4N-SnSe particles, respectively, high-resolution spectrum of Na 1s, Se 3d for Na-SnSe (A) and N 1s, Se 3d for Me_4N-SnSe (B).

We studied the pellet's microstructure using atom probe tomography[132,133] (APT) and STEM (Figures 1.2.4 and 1.2.5) to determine the distribution of Na in the sintered material. Figure 1.2.4 shows the 3D distribution of Na in the pellet illustrated by the 2.0 at% Na isocomposition surfaces. These contour plots delimit the areas where the concentration of Na is ≥ 2 at%.[134] We observe that in the pellet, Na is distributed in four different environments: i) within the crystal lattice, ii) at dislocations, iii) forming grain boundary complexions,[135] and iv) in nanoprecipitates.

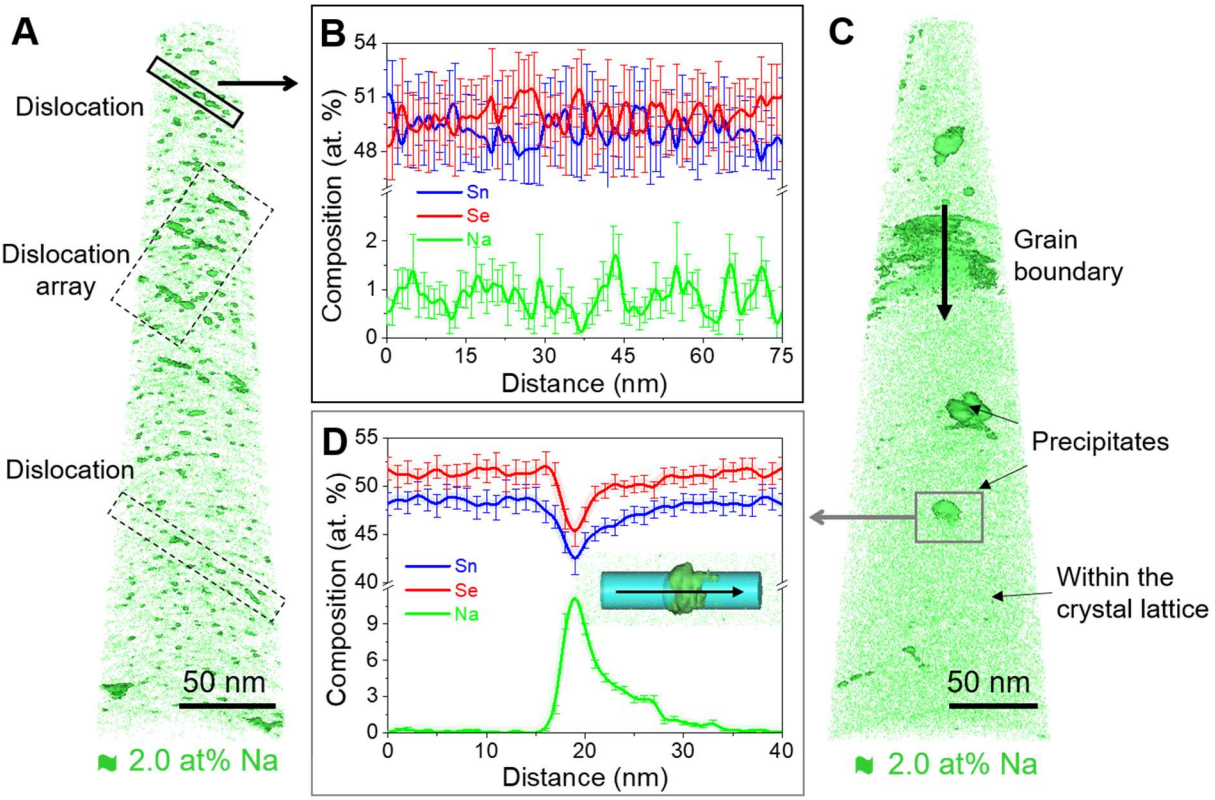

Figure 1.2.4. APT of a Na-containing SnSe pellet. A) 3D distribution of Na showing multiple dislocations highlighted by the Na-2.0 at.% isocomposition surface and indicated by rectangles. B) Composition profile along a dislocation showing the presence of Na at dislocation cores. C) 3D distribution of Na in the same pellet showing Na-rich precipitates, a larger precipitate is observed at the grain boundary. D) Composition profile across a precipitate.

The large number of dislocations observed by TEM can be correlated to the large amount of Sn vacancies in the particles and the annealed powder.[136] Upon annealing, these vacancies diffuse, creating vacancy aggregates of lower energy that collapse into dislocations.[137–139] The composition profile along a dislocation line in Figure 1.2.4.A shows a periodic fluctuation of Na concentration, suggesting that the formation of these dislocations is not only an efficient pathway to relax epitaxial strain but also triggers Na segregation.[140,141] Moreover, the large number of defects in polycrystalline SnSe provides heterogeneous nucleation sites for precipitation,[142–144] explaining the presence of Na-rich precipitates within the grains, at the dislocations, and in grain boundaries (Figure 1.2.4).[145] However, we could not identify the Na-rich phase's exact composition nor crystal structure due to its high air sensitivity, ease of oxidation, and instability under the electron beam.

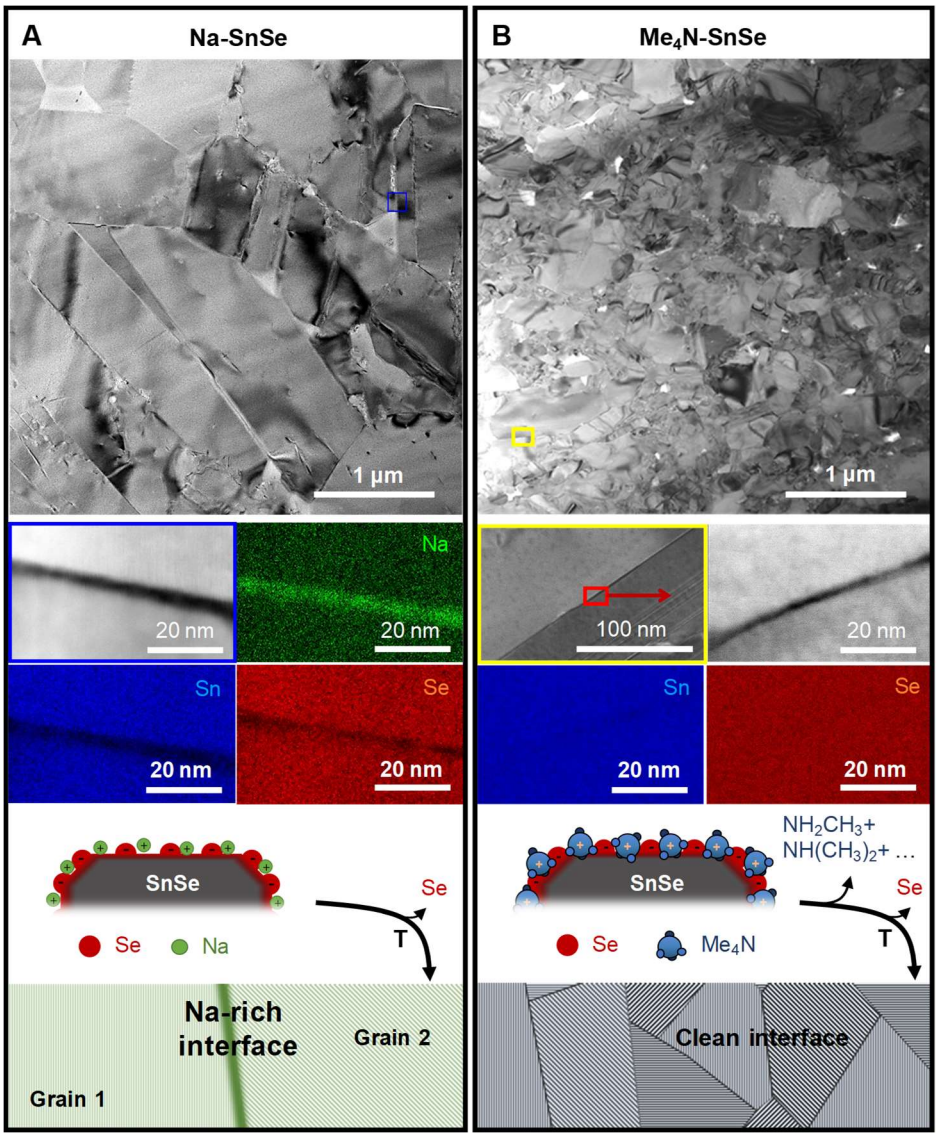

Figure 1.2.5. TEM images representing cross-sections of SnSe pellets. General view (top), together with the corresponding STEM-EDX elemental mapping of a grain boundary (middle), and a scheme of the grain boundary interface (bottom) resulting for the two different cations: A) Na^+ and B) Me_4N^+.

When present in the reaction mixture, Na^+ ions end up on the particle surface and become an involuntary impurity of the consolidated material, referred to as Na–SnSe from now on. To evaluate the effect of Na in the material's microstructure and transport properties, we developed a new synthetic route to obtain Na-free SnSe particles. In this synthesis, we replaced Na^+ for a cation that decomposes during the annealing step. In particular, we used tetramethylammonium salts: Me_4NBH_4 and Me_4NOH, instead of $NaBH_4$ and NaOH. Following the same synthetic and purification process, we obtained pure phase SnSe particles (Figure 1.2.6), referred to as Me_4N-SnSe. XPS analysis of Me_4N-SnSe particles revealed N 1s emission peaks which can be assigned to tetramethylammonium (Figure 1.2.3).[146] None of the elemental analysis techniques used detected Na. Similar to Na-SnSe, Me_4N-SnSe particles show a negative surface charge (zeta potential = -23 ± 5 mV). Based on the above, we conclude that the charge balancing ions are Me_4N^+ as depicted in the scheme in Figure 1.2.5B. We verified the decomposition of adsorbed Me_4N^+ by *in-situ* mass spectrometry analysis, which confirmed the

complete desorption of the organic species at the annealing temperature used, 500 °C, in accordance with previous works.[147] However, by APT and Raman spectroscopy, we detected minor traces of N and C in the final pellet . XRD patterns of the Me_4N–SnSe particles, annealed powder, and final pellet show the same diffraction peaks as Na–SnSe (Figure 1.2.6).

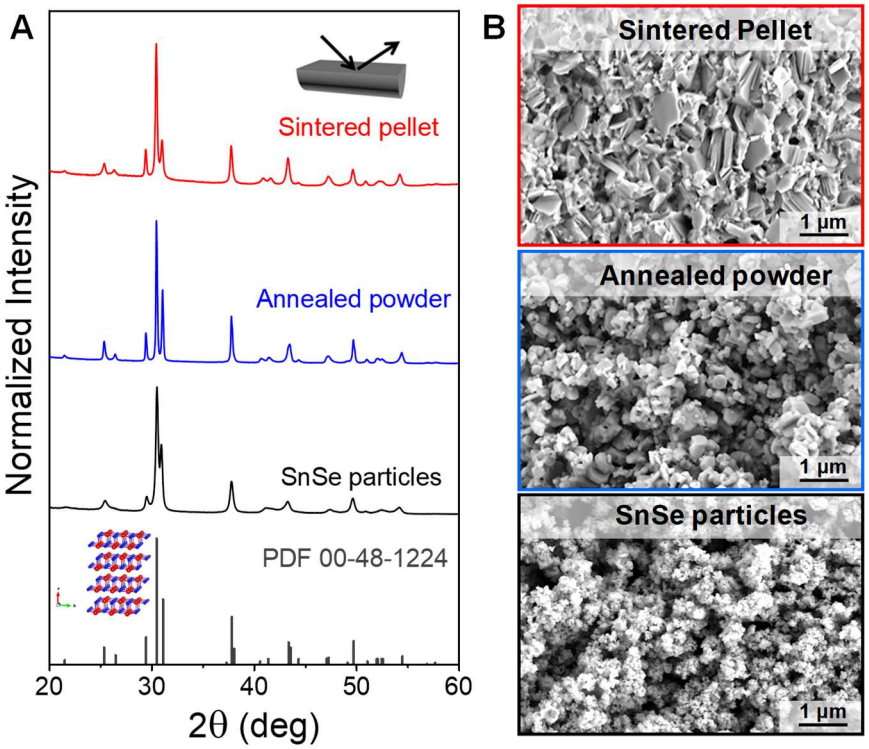

Figure 1.2.6. A) XRD patterns of as-synthesized Me_4N-SnSe particles, annealed powder and sintered pellet along out of plane direction. The inset shows the crystal structure of orthorhombic SnSe. B) the corresponding representative SEM micrographs.

Although both synthetic strategies yield SnSe particles with analogous structural properties, the average grain size of the final pellet is much smaller for Me_4N-SnSe than for Na-SnSe (Figure 1.2.5) despite both having the same density. These results show that the adsorbed ions strongly influence the microstructure of the samples. We propose different reasons for the difference in the microstructures. Firstly, when using Me_4N^+, the aqueous synthesis already yields smaller SnSe particles. While the counterions have the same charge, they differ significantly in size, Me_4N^+ having a radius of 322 pm and Na^+ 98 pm. The larger size of Me_4N^+ allows a smaller number of Me_4N^+ to fit in the Stern layer, increasing the electrostatic repulsion between the particles and therefore yielding smaller particles.[148] Moreover, during the thermal processing, the Se-rich surface reacts with Na producing sodium polyselenides (Na_2Se_x), which through melting provide a capillary force that pulls the grains together.[149,150] Finally, the liquid phase facilitates atomic diffusion between the grains and grain growth.[150] The presence of low melting point Na_2Se_x phases as grain growth promoters has been previously reported in chalcogenide solar cell absorbers.[151–153] In the case of Me_4N-SnSe, Me_4N^+ decomposes into volatile species upon annealing,[154] circumventing the formation of Na_2Se_x and its effects in grain growth during the thermal processing.

The presence of different cations during the material processing also influences the nature of the grain boundaries. STEM-EDS analysis across grain boundaries (Figure 1.2.5) shows Na-rich grain boundary complexions in Na-SnSe while Me_4N-SnSe has clean interfaces.

We evaluated the effects of the Na-SnSe and Me_4N-SnSe distinct microstructure and composition in the transport properties, by measuring the electrical conductivity and Seebeck coefficient of the respective pellets from room temperature until 833 K (Figure 1.2.7). The measurements were performed both in the direction parallel and perpendicular to the pressing axis. Here, we exclusively discuss the properties in the direction parallel to the pressing axis. Measurements in the perpendicular direction show the same trends and can be found original publication.[23]

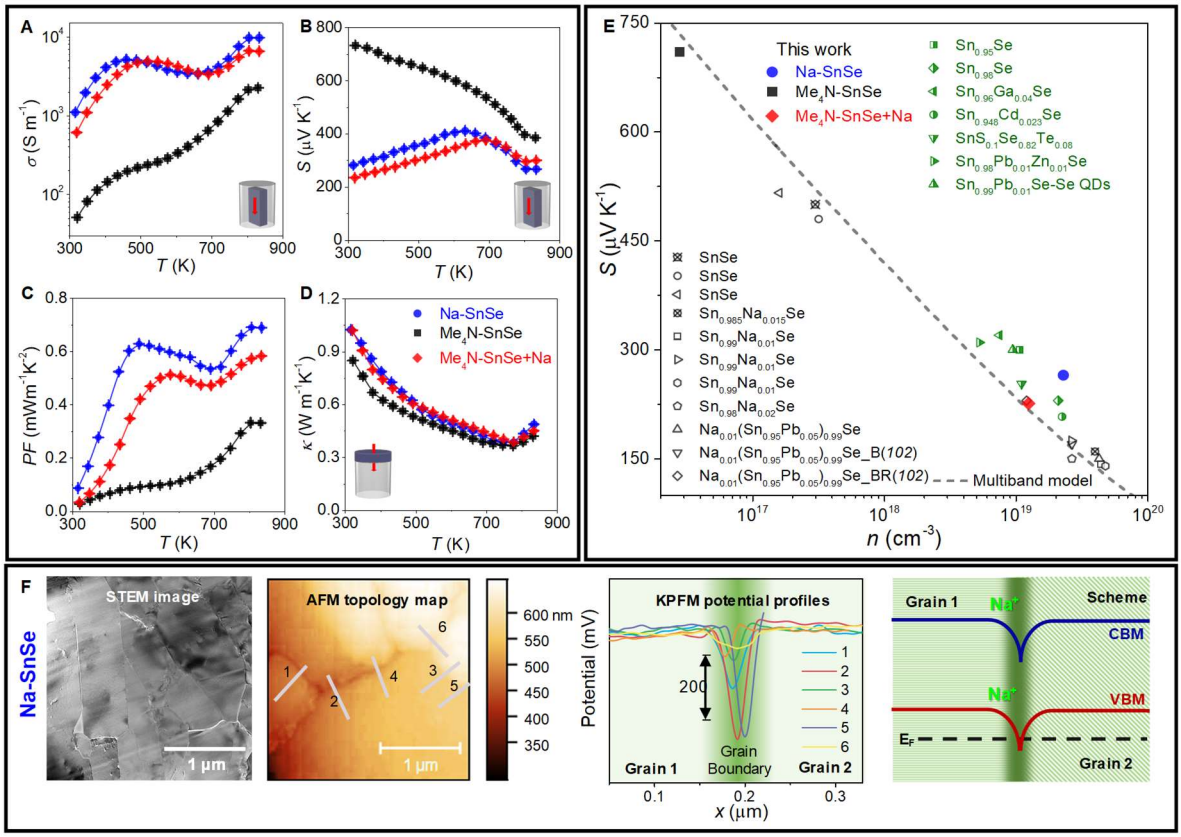

Figure 1.2.7. A) Electrical conductivity, σ; B) Seebeck coefficient, *S*; C) power factor, *PF*; D) thermal conductivity, κ; Na–SnSe, Me_4N–SnSe, and Me_4N–SnSe + Na samples measured in the direction parallel to the pressing axis. E) Pisarenko plot at 300 K. Green dots are references from solution-processed materials[102,107,109,111,120,121,155] and black dots from solid-state synthetic methods,[125,131,156–158] including single crystals.[159,160] The dashed line was calculated using a multiple band model.[161] F) STEM image, atom probe microscopy (AFM) topology maps, KPFM potential profiles across the lines indicated in the AFM topology map, and scheme showing the band bending at the grain boundary in Na–SnSe. CBM, VBM, and E_F indicate the conduction band minimum, valence band maximum, and Fermi level, respectively.

Na-SnSe has higher electrical conductivity than Me_4N-SnSe over the whole temperature range. Hall effect measurements revealed this difference is caused by the three orders of magnitude higher hole concentration of Na-SnSe, ~2.3 $\times 10^{19}$ cm^{-3}, than Me_4N-SnSe, ~2.8 $\times 10^{16}$ cm^{-3}. Na is frequently used as a *p*-type dopant in SnSe due to its tendency to replace lattice Sn^{2+}.[156,158,162] In

Na–SnSe samples, part of the Na diffused into the crystal lattice (Figure 1.2.4), either during the particle synthesis or through the consecutive thermal processes to produce the pellet, thus explaining the high carrier concentration measured.

The electrical conductivities of both Na-SnSe and Me_4N-SnSe show a thermally activated behavior, typical of polycrystalline SnSe.[92,107,156,163] We calculated the weighted mobilities (μ_W) from the Seebeck coefficient and electrical conductivity values[164] to understand the underlying transport phenomenon. In the low-temperature range, the increase of mobility with temperature indicates the presence of energy barriers at the grain boundaries.[165,166] The barrier height (E_b; $\sigma \propto T^{-1/2} \exp(-E_b/k_B T)$) for the Na-SnSe sample (~172 meV) is more than double that for the Me_4N-SnSe (~75 meV). This is also consistent with Na–SnSe lower hall mobility at room temperature, ca. 2.3 $cm^2V^{-1}s^{-1}$ versus ca. 21.2 $cm^2V^{-1}s^{-1}$ for Me_4N–SnSe. As the temperature increases, the effect of the potential barriers diminishes due to thermal carrier excitations.

We observed that the Seebeck coefficient of the Na-SnSe samples is higher than those of polycrystalline samples obtained through melting and annealing, despite the similar charge carrier densities. To illustrate this, we plotted the Seebeck coefficient as a function of charge carrier concentration (Pisarenko plot) at 300 K and compared it with reported experimental data and first-principles calculations using a multiple band model[161] in Figure 1.2.7.E. The plot reveals that not only our Na-SnSe sample but also many other solution-processed SnSe (half-filled green symbols)[102,107,109,111,120,121,155] have Seebeck coefficients exceeding the value expected, a tendency not observed in Na-doped solid-state synthesized SnSe (black open symbols,[125,131,156–158] including single crystals[159,160]).

The high carrier concentration in the Na–SnSe samples comes from the partial diffusion of ionically adsorbed Na into the SnSe crystal lattice during the thermal processing (annealing + spark plasma sintering). However, the amount of Na in the final material cannot be precisely controlled when using Na salts during the particle synthesis, as the Na content is determined by the electrostatic adsorption of Na^+ ions at the particle surface. The amount of Na introduced through surface adsorbates in Na–SnSe exceeds its solubility limit,[131] resulting in partial segregation of Na forming Na-rich dislocations, grain boundaries, and nanoprecipitates (Figures 1.2.4 and 1.2.5). Kelvin probe force microscopy (KPFM) measurements of the surface potential across Na-rich grain boundaries in the Na–SnSe sample revealed charge accumulation and downward band bending at the grains interface (Figure 1.2.7.F).[167,168] These results suggest that the Na-rich interfaces act as potential barriers,[167,168] filtering low energy holes and enhancing the Seebeck coefficient.[169–171] In contrast, for Me_4N–SnSe, which has no detectable secondary phases at the grain boundaries (Figure 1.2.5), the Seebeck coefficient fits the value expected by the calculated Pisarenko relation (Figure 1.2.7.E).

To better understand the role of excess Na, we developed a doping strategy using Me_4N–SnSe particles and adding Na^+ after particle purification. This strategy allows us to control the Na concentration in the final material. We adjusted the content of Na^+ to have carrier concentrations comparable to those obtained for Na–SnSe, but significantly lower content of Na, ≈1%. The Na-doped Me_4N–SnSe sample, named Me_4N –SnSe + Na shows a trend for the

electrical conductivity similar to Na–SnSe, with carrier concentration of ca. 10^{19} cm^{-3}, yet lower Seebeck coefficient (Figure 1.2.7.B) at low temperatures. The room temperature Seebeck coefficient of Me_4N –SnSe+Na fits perfectly with the values expected from the Pisarenko relation calculated using a multiband model (Figure 1.2.7.E, red rhombus), indicating no energy filtering effects in this sample.

Despite the significant difference in the microstructures, the three samples (Na–SnSe, Me_4N–SnSe, and Me_4N–SnSe + Na) have very similar lattice thermal conductivity (Figure 1.2.8). We attribute this to the strong lattice anharmonicity in SnSe as the dominant effect contributing to the thermal conductivity.[160] Overall, we find that the calculated zT is doubled for Na–SnSe compared to Me_4N–SnSe. By increasing the carrier concentration by carefully adding Na after the Me_4N–SnSe particle synthesis, the resulting Me_4N–SnSe + Na sample shows slightly inferior zT than Na–SnSe. We attribute this to a favorable energy filtering effect in Na–SnSe compared to Me_4N–SnSe + Na. However, to estimate the ideal degree of filtering, further work is necessary.

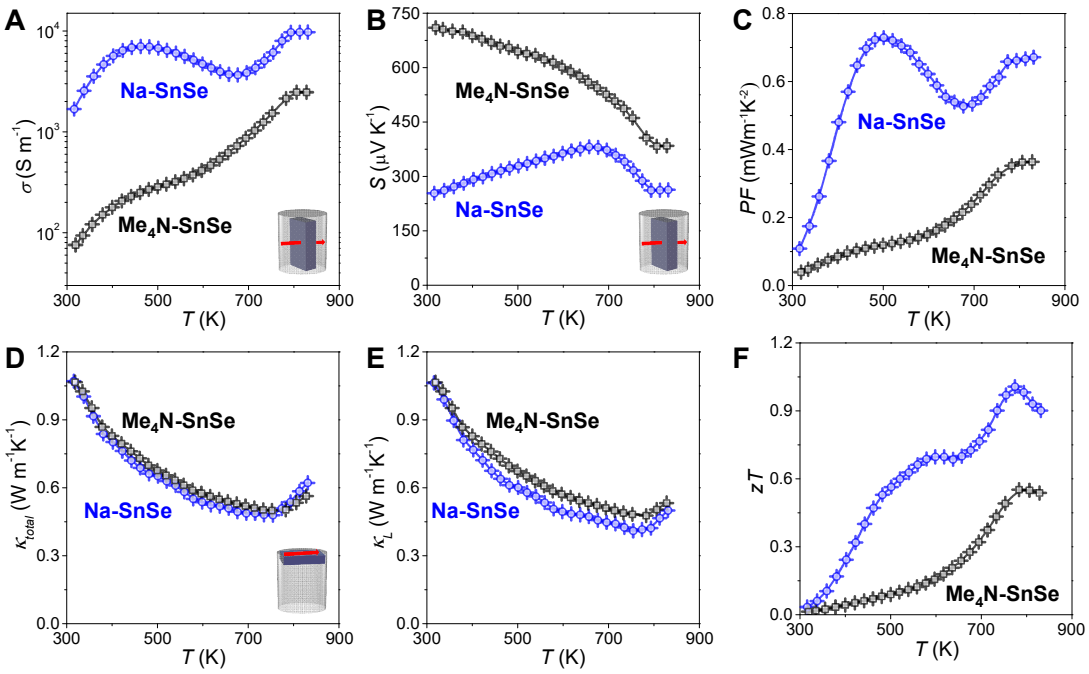

Figure 1.2.8. Thermoelectric properties of Na-SnSe (black) and Me_4N-SnSe (blue) measured in perpendicular direction: A) electrical conductivity, σ; B) Seebeck coefficient, S; C) power factor, PF; D) thermal conductivity, κ_{total}; E) lattice thermal conductivity, κ_L; and F) figure-of-merit, zT.

We investigated the role of surface ion adsorbates in polycrystalline SnSe produced from surfactant-free SnSe particles. We found that when incorporating Na salts in the reaction mixture, Na^+ ions are electrostatically adsorbed on the particle surface and remain there after the particles are removed from the solution. Moreover, Na remains in the material during the annealing and sintering steps, playing an important role in the microstructure evolution and the final material functional properties. In the sintered pellets, Na is present within the matrix, in dislocations, precipitates, and forming grain boundary complexions. Due to the tendency of Na^+ to occupy Sn^{2+} sites, Na–SnSe samples exhibit high carrier concentrations. Moreover, the

interface between Na-rich segregates and SnSe grains induces energy barriers, leading to charge carrier energy filtering and enhancing the Seebeck coefficient.

This work reveals the presence of surface adsorbates in solution-processed surfactant-free methods and their effect on the transport properties. Furthermore, we explain the rationale behind their presence based on the fundamentals of colloidal science. These findings are relevant because they go beyond the specific system studied. They highlight the importance of evaluating possible unintentional impurities and their origin to i) establish the proper structure–property relationships and ii) redefine synthetic protocols to tune material properties controllably.

An example where the lack of impurity awareness has limited our capability to optimize material properties is *n*-type SnSe. Contrary to *p*-type, where solution methods have reached state-of-the-art thermoelectric performance at high temperature, for *n*-type SnSe, zT is much lower than half of the highest reported value (zT of 1.1 for solution-processed material compared to 2.8 for single crystal).[172,173] We believe this is correlated to the fact that all synthetic methods use Na salts to produce SnSe particles. Hence, when *n*-type dopants are introduced, the presence of Na can establish a pinning problem.

The current section was adapted from the cited publication (Adv. Mater. 2021, 33,52, 2106858). Experimental details and supporting information that were not included in this chapter can be found there.

Chapter 2 – Transformation of Nanoparticle-Based Precursors

The examples presented in Chapter 1 illustrate that we require a comprehensive understanding of the synthesis and surface chemistry to use nanoparticles as precursors for solids with targeted features. However, even if those details are known, it might not be possible to establish relationships between the characteristics of the nanoparticle precursor and the properties of the consolidated solid, since the precursors generally undergo transformations upon processing. Chapter 2 deals with such transformations.

In the first section of this chapter I present the results of work I coauthored concerning surface engineering of the electrostatically stabilized colloids presented in 1.2. In particular, SnSe nanoparticles synthesized in solution are coated with CdSe and PbS molecular complexes that crystalize during the transformation of the powders into the dense nanocomposites. The presence of CdSe on the surface inhibits grain growth of SnSe by pinning the boundaries, counteracting the effect of the residual Na impurities on the grain size and yielding a material with a high density of grain boundaries. The resulting SnSe-CdSe nanocomposites present multiple defects at different length scales, which significantly reduce the thermal conductivity and enhance the material's thermoelectric performance.

The second section of this chapter includes a study of the transformation of sterically stabilized nanoparticles into nanocomposites. Given that cesium lead halides have intrinsically unstable crystal lattices and easily transform between perovskite and non-perovskite structures, we explore the conversion of the perovskite $CsPbBr_3$ into Cs_4PbBr_6 in the presence of PbS at 450 °C to produce doped nanoparticle-based composites with embedded Cs_4PbBr_6 nanoprecipitates. We show that $PbBr_2$ is extracted from $CsPbBr_3$ and diffuses into the PbS lattice with a consequent increase in the concentration of free charge carriers. This work exemplifies how the transformation of nanoparticle-based precursors plays an important role in defining the properties of the final nanocomposite. As this transformation is understood it can be exploited, for instance, as a new doping strategy for adjusting the density of charge carriers between 10^{19} and 10^{20} cm^{-3}, the range where PbS shows its best thermoelectric performance.

Both studies were published (ACS Nano, 2022, 16, 1, 78–88; ACS Energy Lett., 2021, 6, 2, 581–587) and are reproduced here with minor modifications.

2.1 Defect Engineering in Solution-Processed Polycrystalline SnSe Leads to High Thermoelectric Performance

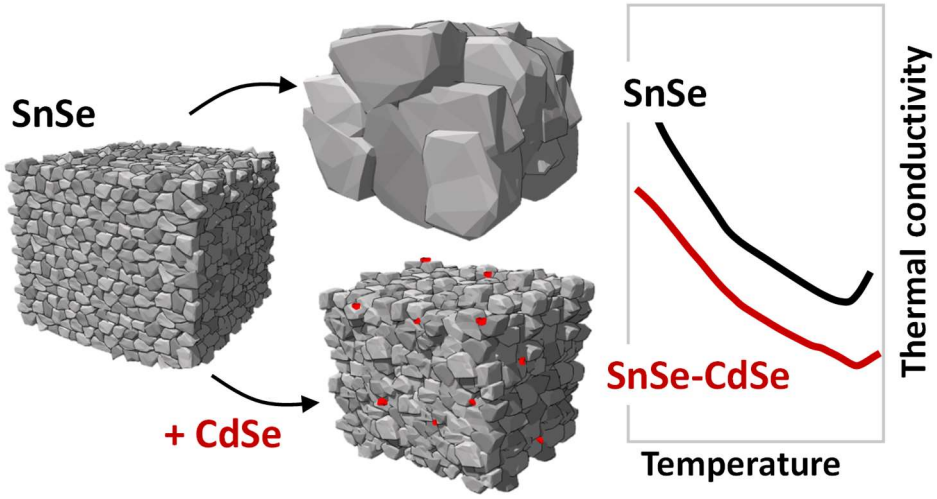

The efficient conversion of heat into electricity by thermoelectric materials necessitates high electrical conductivity (σ), high Seebeck coefficient (*S*), and low thermal conductivity (κ). A tradeoff between these strongly interrelated properties to optimize the performance of thermoelectric materials entails tuning the electronic structure and the charge and phonon scattering mechanisms.[4,93,174,175]

Zhao et al. discovered in 2014 that SnSe has an outstanding thermoelectric performance, originating an outburst of research on the material.[176–183] The highest thermoelectric figure of merit ($zT=\sigma S^2 T\kappa^{-1}$) obtained to date in *p*-type SnSe is ~2.6 at 650 °C along the *b*-axis in pristine SnSe single crystals;[160] and ~2.8 at 500 °C along the *a*-axis in Br-doped *n*-type SnSe single crystals.[173] Despite their outstanding performance, the high cost and stagnant production of single crystals, together with their poor mechanical properties, limit the large-scale use of SnSe in thermoelectric devices.[176] A potential solution is shifting to polycrystalline SnSe-based materials; however, polycrystalline SnSe suffers from lower thermoelectric performance, due to oxidation allegedly leading to higher thermal conductivities,[184] partial loss of anisotropy diminishing electrical conductivity, and imprecise control of the doping level.[125,185]

Different approaches to overcome these limitations include reduction of oxide species;[125,185] liquid-phase compaction[123] and hot deformation processes that promote texture;[186] and doping control with different alkali (K, Na, Li)[131,156,187] and transition metals (Ag, Cu, Zn, Cd).[104,109,114,121,188–190] Additionally, approaches to further enhance the performance of polycrystalline materials have been scrutinized, such as alloying with SnS,[191] Pb,[163] Ge[92] and the

introduction of different nanofeatures such as nanopores or nanoprecipitates (*i.e.* $InSe_y$,[122] $AgSnSe_2$,[192] PbSe,[105] Ag_8SnSe_6[157]).

Herein, we report a simple and scalable synthesis to produce SnSe–CdSe nanocomposites based on the aqueous synthesis of SnSe particles and their surface treatment with CdSe molecular complexes. Such surface treatment allows engineering of the material microstructure promoting defect formation at all length scales. In particular, during the processing, CdSe complexes crystallize, forming CdSe nanoparticles (NPs) at the surface of SnSe particles. CdSe NPs hinder grain growth during consolidation yielding a material with a high density of defects at multiple scales (point defects, dislocations, planar defects, and nanostructures). The presence of CdSe NPs together with the significantly higher defect content in the nanocomposite result in a reduction of the thermal conductivity by 2-fold with respect to bare SnSe produced with untreated SnSe particles. Overall, the strategy presented here produces inexpensive and highly stable polycrystalline SnSe with a zT of ca. 2.2 at 786 K.

SnSe particles were synthesized in water, using selenium and tin chloride as precursors.[113] The obtained SnSe particles were purified to remove unbound ionic impurities by washing them with water and ethanol. To produce the dense SnSe polycrystalline solids, the purified particles were dried under vacuum, annealed in forming gas (5 % H_2 in N_2)[125,185] at 500 °C, and consolidated into cylindrical pellets through spark plasma sintering. In the case of SnSe-CdSe nanocomposites, SnSe particles were first treated with CdSe molecular complexes (x: nominal Cd/Sn ratio; x= 1, 2, 3 and 4%) in N-methyl formamide for 48 h, then washed, dried and annealed. The CdSe solution was prepared by dissolving stoichiometric amounts of CdO and Se powder in mixture of ethylenediamine and 1,2-ethaneditiol (Figure 2.2.1).[193] On the basis of previous studies of hydrazinium-based CdSe solutions, we hypothesize that the molecular solute is composed of a variety of chalcogenidocadmates such as $(Cd_2Se_3)_n^{2n-}$ or $CdSe_2^{2-}$.[194–196] The originally intense orange CdSe solution becomes more clear after the treatment, indicating the adsorption on the SnSe particles. The complete material fabrication process is illustrated in Figure 2.2.1.

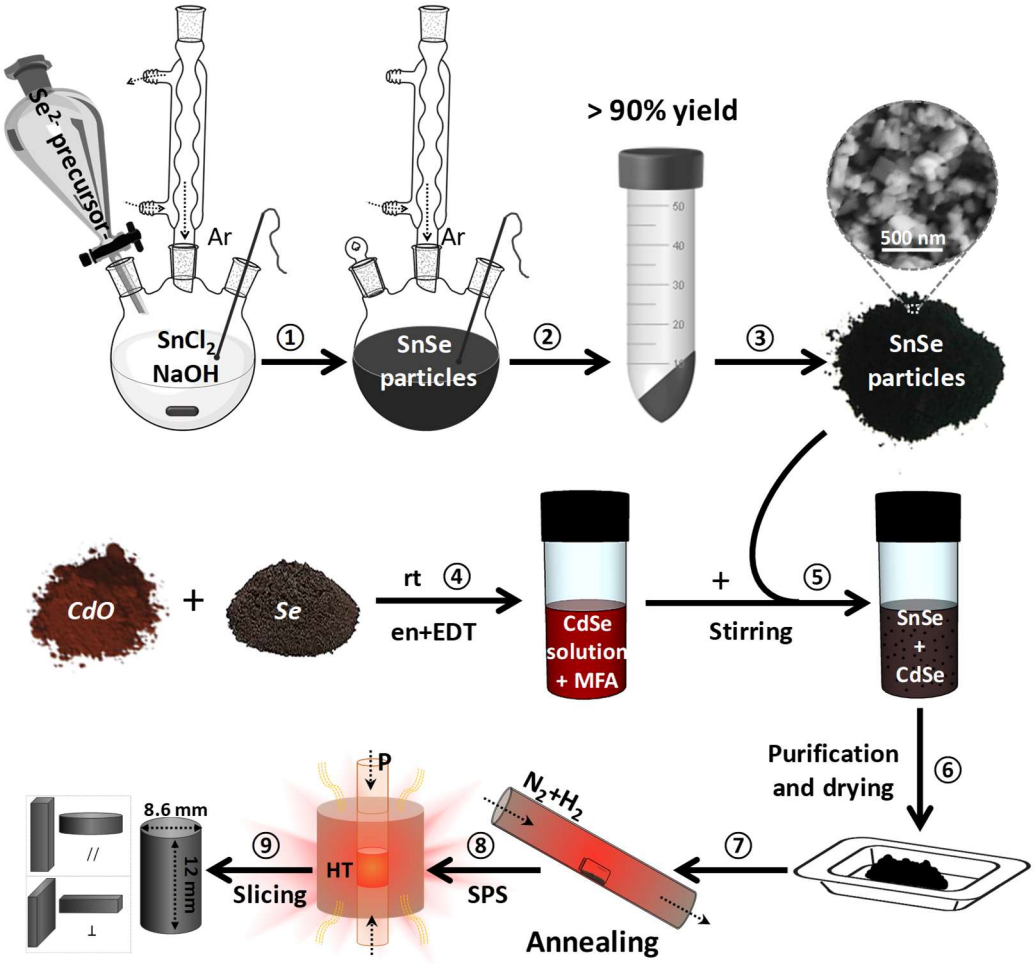

Figure 2.2.1. Scheme of the fabrication process of SnSe–CdSe nanocomposites. (1–3) Aqueous synthesis and purification of SnSe particles; (4) preparation of CdSe molecular solution (CdSe ink); (5) blending the CdSe ink with SnSe particles; (6) purification of the CdSe surface-treated SnSe particles and SnSe–CdSe powder vacuum drying; (7) annealing; (8) spark plasma sintering (SPS) for producing cylinders (⌀ = 8.6 mm × h = 12 mm); and (9) slicing for transport measurements.

Figure 2.2.2.A shows scanning electron microscopy (SEM) images of the pellets obtained from SnSe-x%CdSe particles with different content of CdSe. In the presence of CdSe, the sintered materials develop smaller crystal domains than bare SnSe despite all samples having similar densities. In the case of a CdSe content lower than the estimated to coat the whole SnSe particles (ca. 1 mol %) the resulting samples present large grain sizes, but still smaller than untreated SnSe. Above 2 mol %, the final grain size of the pellets is practically the same regardless of the CdSe content.

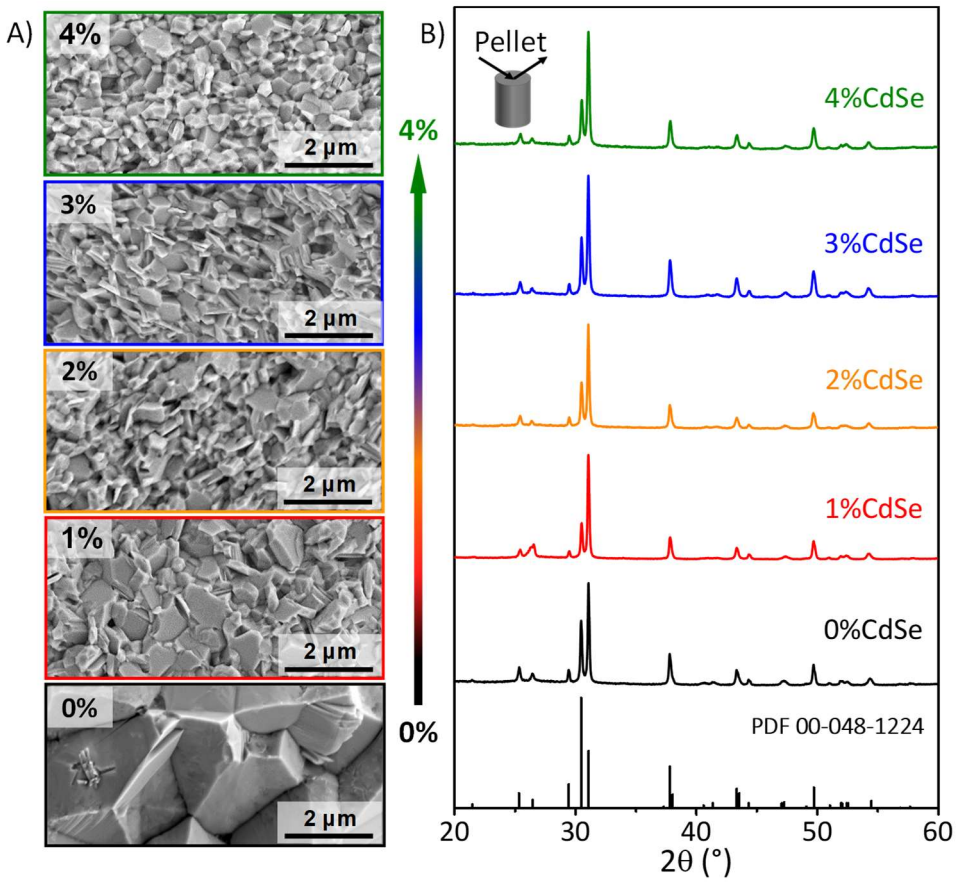

Figure 2.2.2. A) Representative SEM images of the pellets obtained from SnSe-*x*%CdSe (*x* = 0, 1, 2, 3, and 4) particles. B) the corresponding XRD patterns in the direction perpendicular to the pressing axis including the SnSe reference pattern PDF 00–048–1224.

X-ray diffraction (XRD) data showed no evidence of the presence of secondary phases in any of the nanocomposite (Figure 2.2.2 B). Moreover, the grain size of the nanocomposites is stable and hardly changes after the consolidation step, as observed in the structural analysis of the pellets subjected to further thermal treatment such as the heating and cooling cycles from room temperature to 823 K carried out during the transport measurements (Figure 2.2.3). These results evidence the high grain size stability of these materials.

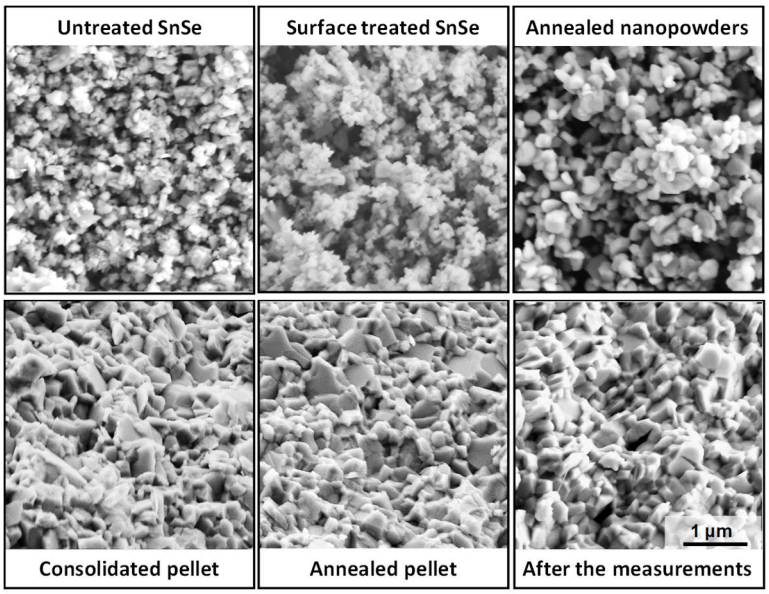

Figure 2.2.3. SEM images of the SnSe-3%CdSe materials at the different stages of the process. Top: as-synthesized SnSe particles, surface treated (3%CdSe) particles, and annealed SnSe-3%CdSe nanopowder. Bottom: the corresponding consolidated SnSe-3%CdSe pellet, the annealed SnSe-3%CdSe pellet, and the SnSe-3%CdSe pellet after the heating and cooling cycles of the transport measurements.

To understand the mechanism that inhibits grain growth in the presence of CdSe, we analyzed the bare SnSe and SnSe-3%CdSe samples after surface treatment, annealing, and consolidation (Figure 2.2.4). SEM images indicate that the particle morphology is barely affected by the CdSe surface treatment. Differences appear between the CdSe treated and the untreated samples upon annealing. Even though grain coarsening occurs in both materials during annealing, the average grain size of bare SnSe increases from 150 ± 50 nm to 680 ± 400 nm, which is 2.5 times more than that in the presence of CdSe. The difference in grain sizes is more evident after the pressure-assisted sintering step through spark plasma sintering (45 MPa, 500 °C). In the presence of CdSe, grain growth is hindered, resulting in relatively smaller crystal domains (Figure 2.2.4.A) and, consequently, in a higher volume fraction of grain boundaries for the SnSe–CdSe nanocomposites compared to bare SnSe. SnSe samples have an average grain size of ca. 3.5 ± 3.0 µm while SnSe-3%CdSe nanocomposites display grain sizes of ca. 0.3 ± 0.1 µm as shown by electron backscattering diffraction (EBSD) inverse pole figure maps (Figure 2.2.4.B).

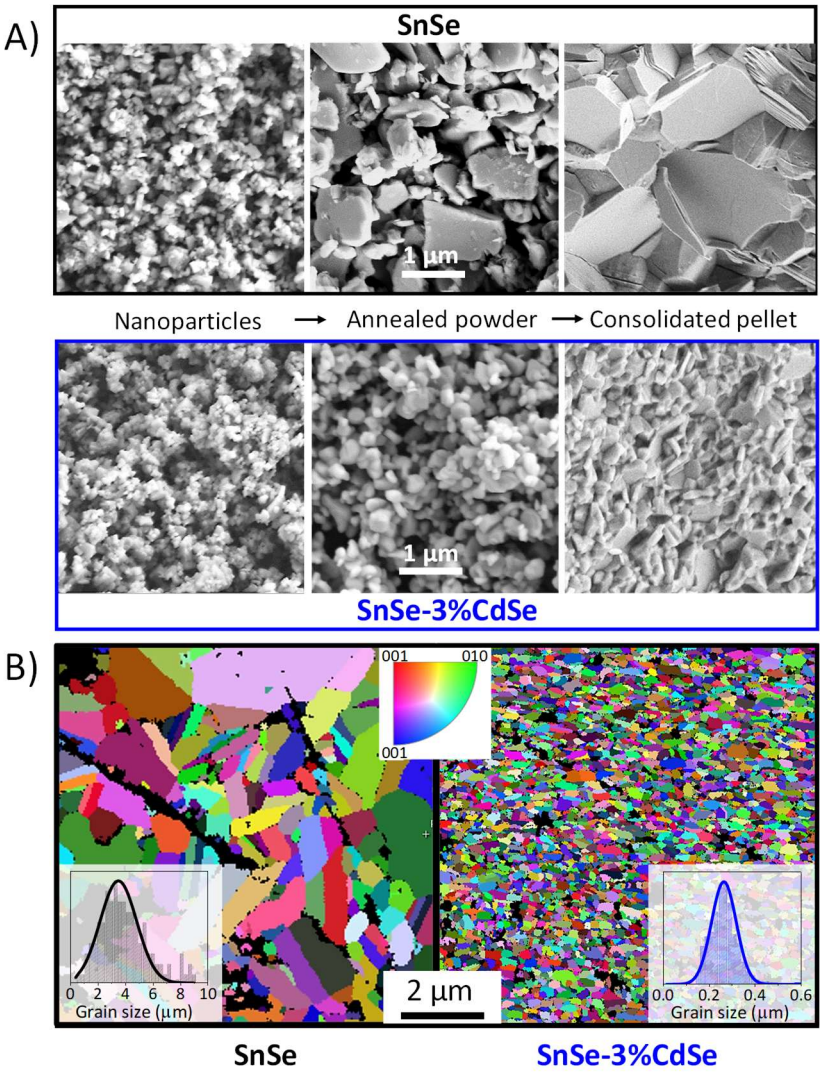

Figure 2.2.4. A) SEM images of SnSe particles, the corresponding annealed powder, and the consolidated pellet without (top, black) and with (bottom, blue) the CdSe-surface treatment. B) EBSD inverse pole figure maps for bare SnSe (left) and SnSe-3%CdSe (right) pellets; insets show the grain size histograms.

The sintering process of surface-treated SnSe particles involves the crystallization of CdSe complexes into CdSe NPs.[193] Control experiments revealed that the complete crystallization of CdSe complexes occurs at 350 °C, yielding ca. 4 nm CdSe NPs. At this same temperature, untreated SnSe particles hardly show any difference in grain size compared to the as-synthesized SnSe particles. Considering that the CdSe crystallization temperature is unaffected by the presence of SnSe particles, we conclude that at 350 °C, there is a homogeneous distribution of CdSe NPs at the surface of SnSe particles.[197] On the basis of the CdSe and SnSe average particle sizes, we estimate that CdSe NPs cover approximately 70% of the total surface of SnSe for the SnSe-3%CdSe sample. Therefore, the corresponding powder densification and coarsening are strongly affected by the presence of secondary phase CdSe NPs.

In the classical theory of grain growth, the average grain growth rate is proportional to the average rate of grain boundary movement.[150] When second-phase particles are present at the grain boundaries, the driving force for boundary migration is reduced, hindering grain

growth.[198] This is known as the Zener pinning effect.[199] Zener pinning occurs when a grain boundary is intersected by a second-phase particle, as the particle removes part of the grain boundary area of greater energy than the interior of the grain, it exerts a drag force on the grain boundary.[200] In such a situation, the growing grain is subject to two opposing pressures: the driving pressure for growth and the Zener pinning pressure (drag) arising from the particles, kinetically retarding grain growth.[201]

The effect of CdSe NPs in the microstructure of SnSe–CdSe nanocomposites is in accordance with grain growth stagnation predicted by the Zener pinning effect. Figure 2.2.2 shows that as the content of CdSe increases, the average grain size is reduced. Moreover, considering that bare SnSe and all SnSe–CdSe pellets have the same density despite their difference in grain sizes, we believe that the presence of CdSe NPs does not affect atomic diffusion along the grain boundaries, i.e., the densification rate. In contrast, grain boundary mobility is hampered, limiting grain growth. The result is a material with the same density but much smaller grain domains than bare SnSe.[150]

One key point to achieving grain growth inhibition through such a surface treatment is the proper selection of the metal chalcogenide complex. During the thermal processing, the material selected should crystallize as a secondary phase at the SnSe particle surface instead of diffusing into its crystal structure creating a solid solution. To satisfy this condition is necessary to choose a material with a positive enthalpy of mixing and a miscibility gap over the processing temperature and pressure range. In other words, the high enthalpic contribution of mixing the secondary phase drives its segregation, preventing the formation of a solid solution.[150] As observed in the phase diagram,[202] CdSe and SnSe are immiscible in the whole range of processing temperatures (Figure 2.2.5). The immiscibility of CdSe and SnSe is corroborated by our XRD data showing that there is no difference in the lattice parameters of bare SnSe and SnSe–CdSe nanocomposites.

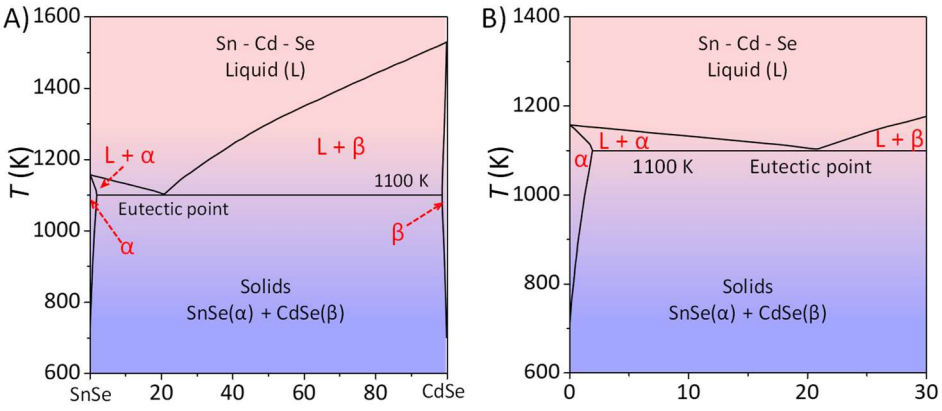

Figure 2.2.5. A, B) Phase diagram of the system SnSe-CdSe adapted from literature.[203]

To prove this idea, we chose a different semiconductor that is highly soluble in SnSe (no miscibility gap) to prepare the molecular complexes and treat the particles. PbS is known to form a stable solid solution with SnSe up to concentrations of 20%.[204] When comparing the two composite materials at different processing stages, we observe that in the presence of PbS the grain coarsening is enhanced significantly already in the annealing step and yields pellets with grains as large as those in bare SnSe (Figure 2.2.6). XRD analysis of the SnSe-3%PbS pellet corroborates the solid-solution formation as the lattice parameter changes, from a = 11.494 Å to a = 11.515 Å (Figure 2.2.6.E).

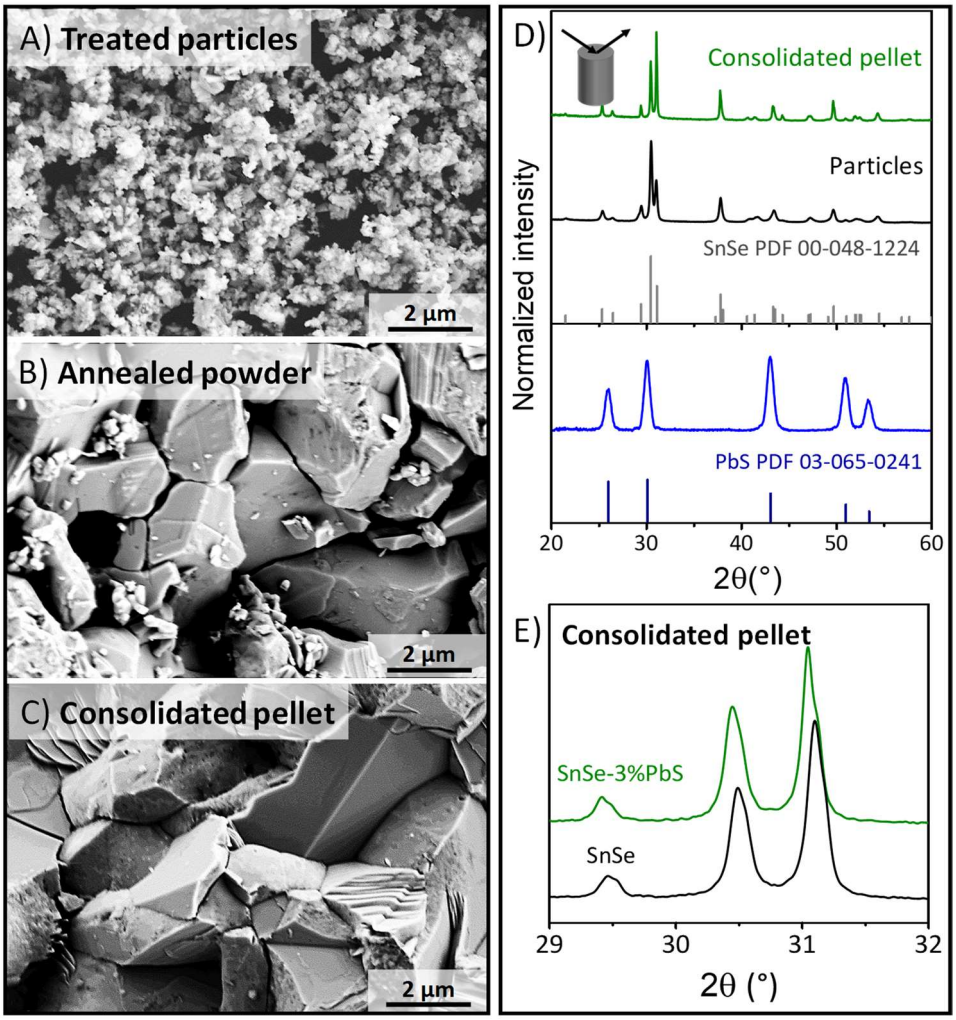

Figure 2.2.6. Representative SEM images of A) PbS-surface-treated SnSe particles, B) the corresponding annealed powder, and C) consolidated pellet. D) XRD diffraction patterns of recrystallized PbS molecular complexes (blue), the surface-modified particles (black), and consolidated pellet measured in the direction perpendicular to the pressing axis (green). The SnSe reference pattern PDF 00–048–1224 is shown in gray and the PbS reference pattern PDF 03–065–0241 in dark blue. E) Main peaks of the XRD pattern of the consolidated pellets with (green) and without (black) PbS surface treatment showing the peak shift due to partial alloying of PbS.

The electrical conductivity, Seebeck coefficient, thermal conductivity, and calculated figure of merit of bare SnSe and SnSe–CdSe nanocomposites with different content of CdSe were measured in the direction parallel and perpendicular to the pressure axis and show the same trends in both directions. We limit the discussion to the transport properties in the parallel

direction because the *zT*s in that direction are the largest ones. Moreover, for clarity the discussion focuses on comparing bare SnSe and the best performing SnSe–CdSe nanocomposite, which corresponds to 3 mol %, referred to as SnSe-3%CdSe (Figure 2.2.7).

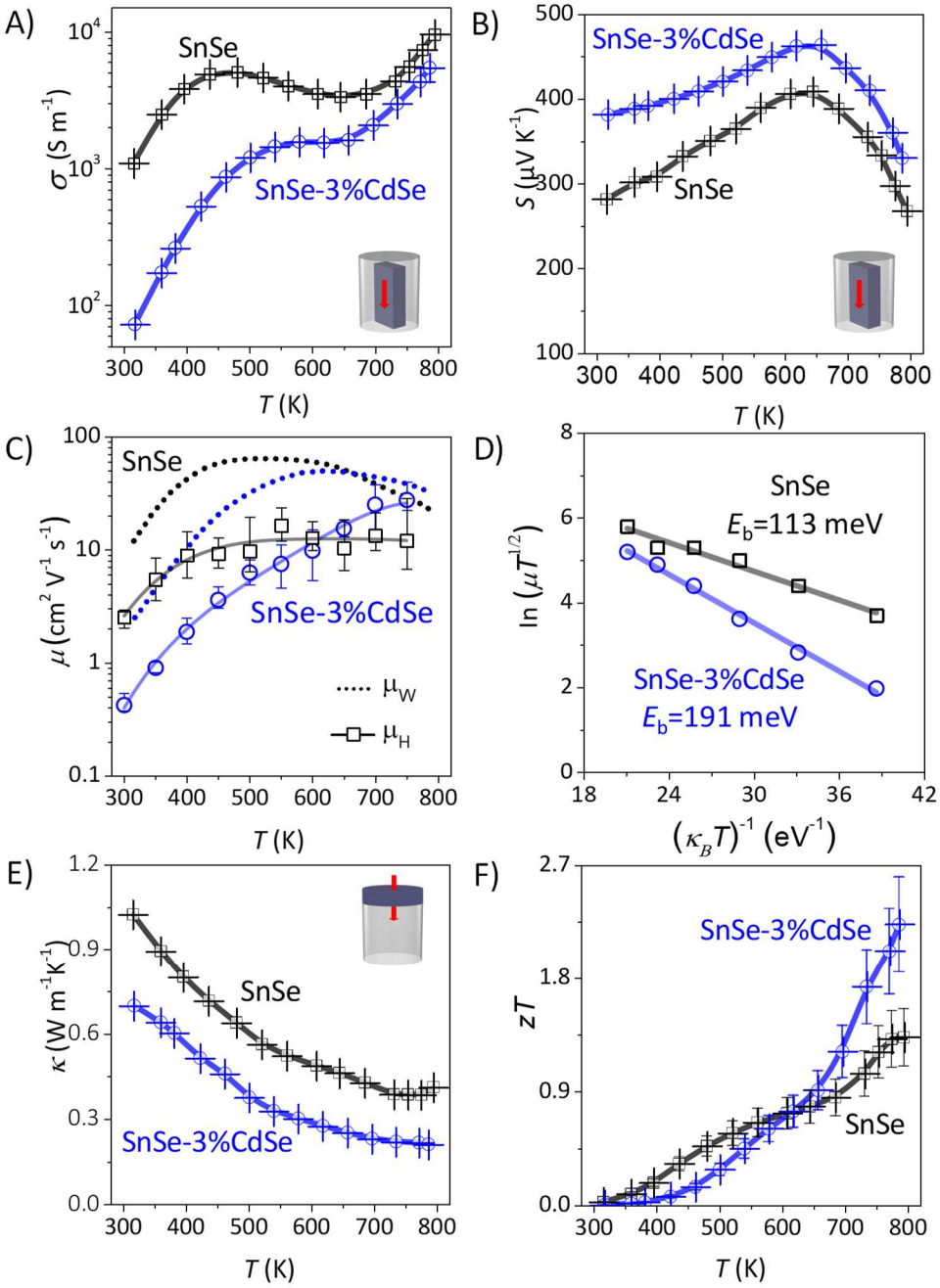

Figure 2.2.7. Temperature dependent transport properties of bare and CdSe treated SnSe. A) Electrical conductivity, σ. B) Seebeck coefficient, *S*. C) fitting for the energy barrier, E_b, ($\mu \propto T^{-1/2} \exp(-E_b/k_BT)$). D) Hall and weighted mobilities, μ_H and μ_w respectively. E) total thermal conductivity, κ. F) figure of merit, *zT*, for bare SnSe (black) and the SnSe-3%CdSe nanocomposite (blue).

Bare SnSe shows a higher electrical conductivity and a lower positive Seebeck coefficient than those of SnSe-3%CdSe in the whole temperature range (Figures 2.2.7.A and B). The Hall carrier

concentration (p_H) of SnSe-3%CdSe is lower (ca. $p_H = 9 \times 10^{18} cm^{-3}$) than that of bare SnSe (ca. $p_H = 2 \times 10^{19} cm^{-3}$). CdSe is generally an *n*-type semiconductor,[205] and it has a much lower electron affinity than that of *p*-type SnSe. Thus, within the SnSe matrix, CdSe injects free electrons to SnSe, inducing band bending in the regions close to CdSe domains. Furthermore, owing to the small size of the CdSe crystal domains, its Fermi level becomes pinned near the valence band edge, thus trapping holes from the SnSe matrix. Thus, the hole carrier concentration is reduced in the presence of CdSe, which directly translates into an increase of the Seebeck coefficient. Moreover, the presence of larger energy barriers at the interface between CdSe and SnSe allows for even higher Seebeck coefficients due to the filtering of high energy carriers.[169]

The temperature dependence of the electrical conductivity and the Seebeck coefficient of both materials are similar to those previously reported polycrystalline SnSe.[92,107,156,163] To understand the underlying transport mechanism, we compare the hall mobilities with the calculated weighted mobilities (μ_W, Figure 5c) according to the equation:[164]

$$\mu_W = \frac{3h^3\sigma}{8\pi e(2m_e k_B T)^{3/2}}\left[\frac{exp\left[\frac{e|S|}{k_B} - 2\right]}{1 + exp\left[\frac{-5e|S|}{k_B} + 5\right]} + \frac{\frac{3}{\pi^2}\frac{e|S|}{k_B}}{1 + exp\left[\frac{5e|S|}{k_B} - 5\right]}\right]$$

where h, k_B, e, and m_e, are the Planck's constant, Boltzmann's constant, electron charge, and electrons mass. Both mobilities have the same behavior, indicating the reliability of the Hall effect measurements.

Bare SnSe and SnSe-3%CdSe nanocomposites show thermally activated conductivity from room temperature up to ca. 500–600 K. In this temperature range, the increase of mobility with temperature reflects the presence of potential barriers due to charge accumulation at the grain boundaries.[165,206] The energy barrier height (E_b; $\mu \propto T^{-1/2}\exp(-E_b/k_B T)$) for SnSe–CdSe nanocomposites is 190 meV, while for SnSe, it is 113 meV (Figure 2.2.7.D). The larger energy barrier of the SnSe-3%CdSe material results in lower mobility at room temperature.[165,207] At high temperatures, the difference in mobility between both materials is practically negligible. With increasing temperature, the thermally excited carriers reduce the effect of the potential barriers on mobility, and the dominant scattering mechanism in both materials is acoustic phonon scattering.

The Seebeck coefficient in both materials peaks at ca. 650 K, indicating the onset for bipolar conduction. As the material transitions from the *Pnma* to the *Cmcm* phase, the changes in the local bonding translate into differences in the electronic structure, including a reduction of the bandgap from 0.61 to 0.39 eV that favors the thermal excitation of minority carriers.[160,163] Above 800 K, the material is fully converted to *Cmcm* and both the Seebeck coefficient and electrical conductivity stabilize.

The thermal conductivities of both nanomaterials follow the same trend in the whole temperature range. From room temperature up to ca. 790 K, the values decrease monotonically. At higher temperatures, due to the SnSe phase transition to the higher symmetry *Cmcm* phase, the thermal conductivity increases. The temperature at which the *Pnma* fully converts into the *Cmcm* phase was analyzed by differential scanning calorimetry and temperature-dependent XRD, both analyses indicate a complete phase transition at 800 K.

In the whole temperature range, the thermal conductivity of SnSe-3%CdSe nanocomposites is almost 50% lower than that of bare SnSe. At the temperature where the thermal diffusivity is minimum (786 K), the C_p measured for the SnSe-3%CdSe nanocomposite is 0.263 J g^{-1} K^{-1} leading to a thermal conductivity of 0.20 W m^{-1} K^{-1} ($\kappa_{lattice}$= 0.14 W $m^{-1}K^{-1}$). This value is similar to the lowest reported values for polycrystalline SnSe.[92,109,125]

To comprehend the origin of such low thermal conductivities, the microstructure of bare SnSe and SnSe–CdSe nanocomposites were further investigated by transmission electron microscopy (TEM) and atom probe tomography (APT, Figures 2.2.8).[132,133]

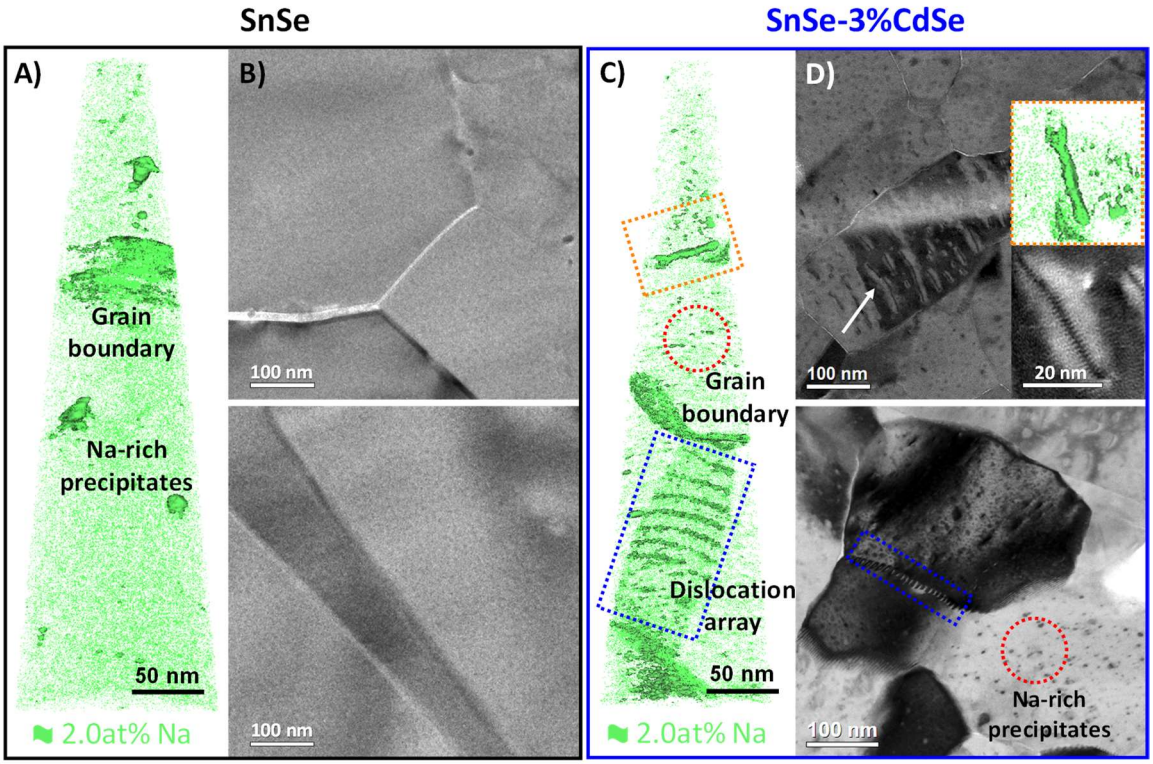

Figure 2.2.8. A) APT characterization showing the 3D distribution of Na and B) TEM images of different grain boundaries in bare SnSe. C) APT characterization showing the 3D distribution of Na and D) TEM images of SnSe-3%CdSe nanocomposites. The correspondence between defects in APT and TEM is highlighted with red, blue, and orange dashed boxes.

Na is an unavoidable impurity due to the nature of the aqueous-based synthesis and the use of Na salts in the reaction, yet it is beneficial for doping. Figures 2.2.8.A and C show the 3D

distribution of Na with the isocomposition surface of 2.0 at% Na. In both materials, bare SnSe and SnSe-3%CdSe, Na is found within the grains, at dislocations and grain boundaries, and in Na-rich precipitates (Figures 2.2.8.A, C and 2.2.9). Elemental analysis by inductively coupled plasma optical emission spectroscopy (ICP-OES) and energy-dispersive X-ray spectrometry (EDS) indicate that both samples contain the same amount of Na, but the defects associated with Na differ in their concentration. The comparison between low-magnification TEM images (Figures 2.2.8.B, D) and APT data clearly reveals the different microstructure of the materials. SnSe-3%CdSe nanocomposites present a larger density of grain boundaries, dislocations, planar defects, and Na-rich precipitates (Figure 2.2.8.D).

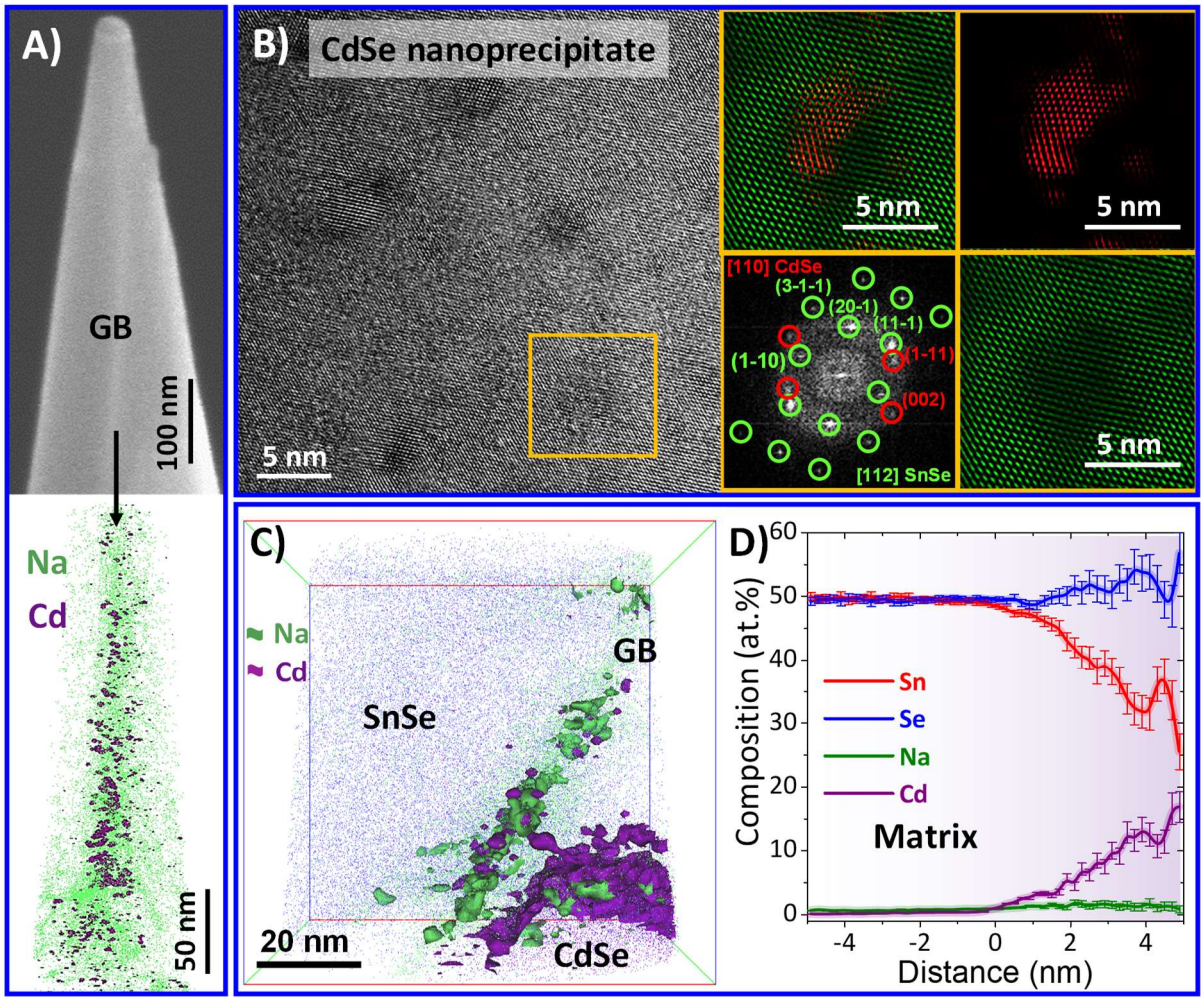

Figure 2.2.9. A) SEM image of the tip (top) used for the APT elemental analysis (bottom) showing the enhanced presence of Na and Cd at the grain boundary. B) CdSe NP with *Fm3m* cubic phase with the corresponding indexed power spectrum from the region marked in yellow and the phase filtered images highlighting the CdSe NPs (red) and the SnSe matrix (green). C) 3D distribution of elements from APT analysis in a region containing a grain boundary and a CdSe NP. D) composition profile across a CdSe NP.

Figure 2.2.9 shows the analysis carried out with APT and HRTEM for the sample SnSe-3%CdSe. Both techniques revealed the presence of CdSe NPs in the range between 1 and 20 nm. In particular, the spectrum analysis allowed to the identify that CdSe NP possesses a *Fm3m* cubic structure (Figure 2.2.9.B). Finally, APT uncovered the presence of Cd at the grain boundaries together with the segregation of Na and depletion of Sn. Due to the variation of chemical composition and likely the structure at the grain boundary, the most accurate way to describe the interfacial material at the grain boundary would be in the terms of grain boundary complexions,[135] which can generally scatter phonons more strongly than a clean boundary.[208] Such grain boundary complexions are also associated with the enhanced energy barrier for holes that reduces carrier mobility and enhances the Seebeck coefficient through energy filtering effects as seen in the charge transport analysis.

The dominant phonon modes in SnSe have mean free paths of a similar length to the spacing between the defects found in the SnSe-3%CdSe nanocomposite, such as atomic Na and Cd impurities, CdSe NPs and Na-rich precipitates ranging from 1 to 20 nm, and grain boundary complexions.[209] This explains the significant reduction in the overall thermal conductivity with respect to bare SnSe, where the density of defects is significantly lower. Moreover, the surface treatment with the CdSe molecular complexes may reduce the overall content of oxide species in the final composite, which is presumed to have a positive effect on the thermal conductivity.[125,184] Such reduction of the thermal conductivity leads to a state-of-the-art figure of merit in solution-processed SnSe of 2.2 at 786 K, comparable to the best performing polycrystalline SnSe.

In summary, this study lea to a scalable, simple, and economical method to produce high-performance polycrystalline SnSe thermoelectric materials. Specifically, we optimized a water-based synthesis protocol to obtain large quantities of SnSe particles and developed a surface treatment to (i) inhibit grain growth during consolidation and operation, (ii) introduce CdSe NPs within the range 1–20 nm, (iii) create grain boundary complexions, and (iv) enhance the number of defects at multiple length scales, such as atomic impurities, planar defects, dislocations, and Na-rich precipitates. The presence of scattering sources at all relevant length scales improved the figure of merit from $zT = 1.3$ in bare SnSe to $zT = 2.2$ in SnSe–CdSe nanocomposites. We believe that the strategy presented here for inhibiting grain growth is of great significance beyond the thermoelectric field because it tackles grain coarsening in semiconductor nanocomposites.

The current chapter was adapted from the cited publication (ACS Nano 2022, 16, 1, 78–88). In particular: the format of the figures was adapted, the discussion on grain growth was amended to distinguish grain boundary mobility from diffusion across grain boundaries, and comments were added to include the most recent findings on the role of oxides in the high thermal conductivity of polycrystalline SnSe. Experimental details and supporting information that were not included in this chapter can be found there.

2.2 Exploiting the Lability of Metal Halide Perovskites for Doping Semiconductor Nanocomposites

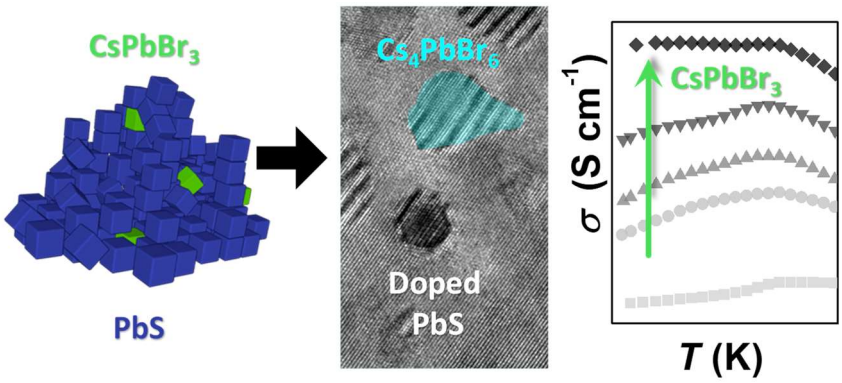

Research on metal halide perovskites is advancing rapidly, owing to the compelling electronic, optical and structural properties of these ionic semiconductors, such as long diffusion lengths and lifetimes of carriers,[210–212] low exciton binding energies,[213] low number of trap states despite the high concentration of vacancies,[210,214] composition-tunable bandgap,[215,216] and ease of processibility.[217–220] Due to the relatively labile crystal structure of metal halide perovskites, the understanding and control of the chemical and structural transformations that these compounds readily undergo are some of the most pressing questions.[221]

Cesium lead halides can adopt perovskite and non-perovskite structures with different dimensionalities. Perovskites are composed of Cs^+ cations stabilizing $[PbX_6]^{4-}$ octahedra in a cubic or, upon slight distortion, tetragonal or orthorhombic phases, where all the corners of the $[PbX_6]^{4-}$ octahedra are shared.[222] All these compounds adopt regular $CsPbX_3$ stoichiometry (3D). Non-perovskite structures include polymorphs with various stoichiometries, but all of them lose the corner-sharing motif in the lattice. The first example of these structures is a polymorph that despite having the same $CsPbX_3$ stoichiometry crystallizes in an orthorhombic phase (δ-phase) with chains of edge-sharing octahedra (1D).[223] Another example is the lead-depleted Cs_4PbX_6 structure where the $[PbX_6]^{4-}$ octahedra are isolated (0D).[222,224–226] A third closely related non-perovskite structure that has lower Cs^+ content and does not contain $[PbX_6]^{4-}$ octahedra, $CsPb_2X_5$, can be described as layers (2D) of $[Pb_2X_5]^-$ clusters separated by Cs^+ ions.[222,224–226] Due to a large difference in the involved atoms' electronegativities, all these cesium lead halides exhibit mixed bonding nature. The lead halide framework is dominated by covalent bonds and balanced by ionically bound Cs^+ cations. The lack of covalency between Cs^+ and the anionic units enable crystal lability.[227] As a direct consequence, the ions move easily and allow transformation between the different structures- provided that the stoichiometry is compensated.

Very common are the transformations between $CsPbBr_3$ and Cs_4PbBr_6 structures especially in nanocrystals (NCs). The transformation of Cs_4PbBr_6 into $CsPbBr_3$ is achieved by adding $PbBr_2$ to the structure[228] or by extracting CsBr by chemical complexation or intercalation,[229] or diffusion and dissolution of CsBr in water.[230] The chemical transformation from $CsPbBr_3$ to Cs_4PbBr_6 can be induced by removing $PbBr_2$ from the crystal lattice by its complexation with

thiols or amines.[231–233] In all these reactions purification of the NCs is required to separate the undesired byproducts: either CsBr or $PbBr_2$. PbS NC-based solids find applications in various fields including transistors,[234–237] solar cells,[238–241] photodetectors,[240,242,243] and thermoelectrics.[58,93,244] In most of these applications adjusting the number of free charge carriers to control charge transport is crucial. The conventional *n*-type dopants for bulk lead chalcogenides are halides. Incorporation of halide ions (X= Cl^-, Br^-, I^-) in the chalcogenide (Y= S^{2-}, Se^{2-}, Te^{2-}) sublattice results in the addition of one electron in the conduction band per halide to compensate for the different valency of halides and chalcogenides.[245] Strategies to dope bulk semiconductors require control over the composition at the impurity level; the straightforward translation into doping bottom-up assembled NC solids is to use doped NCs. However, impurity doping of NCs is energetically[246] and kinetically unfavorable, since the diffusion path of impurity atoms to the surface is short.[247] Although tuning NC's composition has been attempted[235,248] the introduction of a controlled amount of impurities in small structures is problematic for the preparation of heavily doped semiconductors.[249–251] Alternative approaches to dope NC-based solids have focused on changing the NC surface chemistry,[58,239,245,252–255] inducing partial cation exchange,[256,257] and blending with other NCs.[93,258,259]

PbY – perovskite nanocomposites have been used in photodetectors,[260,261] LEDs[262,263] and photovoltaics.[264,265] Remarkably, PbS NC inclusions can provide stability to the cubic phase of perovskites suppressing the cubic-orthorhombic phase transition,[266] and perovskite passivation layers enhance charge carrier separation in PbS NCs by providing adequate energy alignment.[267] Furthermore, PbY nanocomposites with secondary phases might be of great importance for thermoelectrics.[93,268]

Herein we propose a strategy to produce doped PbS nanocomposites that makes use of the byproduct of the transformation of $CsPbBr_3$ into Cs_4PbBr_6, $PbBr_2$, upon heating a mixture of $CsPbBr_3$ and PbS NCs (Figure 2.1.1). Our approach simultaneously introduces dopant ions (Br^-) and a secondary phase (Cs_4PbBr_6) in PbS nanocomposites.

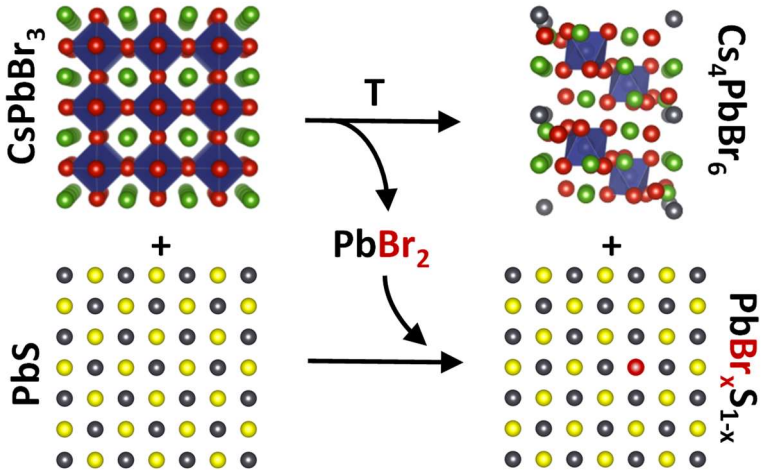

$$4\ CsPbBr_3 + PbS \longrightarrow [Cs_4PbBr_6 + 3PbBr_2 + PbS] \longrightarrow Cs_4PbBr_6 + PbBr_xS_{1-x}$$

Figure 2.1.1. Chemical transformation of $CsPbBr_3$ into Cs_4PbBr_6 triggered by the dissolution of $PbBr_2$ in PbS.

We prepared nanocomposites by mixing PbS NCs with a controlled amount of $CsPbBr_3$ NCs in toluene. This NCs' blend was dried under vacuum and annealed with forming gas (5 % H_2 in N_2, 1 bar) to yield a powder that was then pressed into pellets with relative densities of ~92 % using spark plasma sintering (Figure 2.1.2).

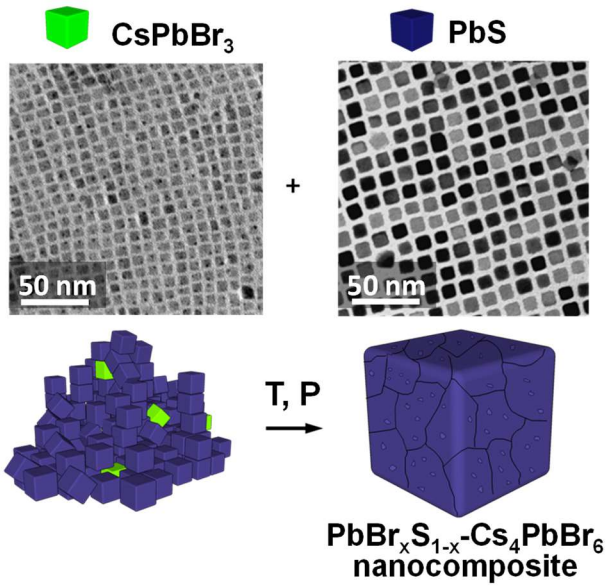

Figure 2.1.2. TEM images of the used NCs and scheme of the bottom-up assembly processes to produce doped PbS-Cs_4PbBr_6 nanocomposites. The nanocomposites are prepared by blending the NCs in solution, annealing to remove the organic ligands, and finally consolidating at 45 MPa and 500 °C.

To follow the chemical transformation of the perovskites, we performed *in-situ* temperature-dependent X-ray diffraction (XRD) measurements of a mixture of PbS NCs and 30% wt. $CsPbBr_3$ NCs (Figure 2.1.3). This mixture was heated up to 450 °C and kept at that temperature for 60 minutes, as long as the annealing. Upon heating to 150 °C, $CsPbBr_3$ NCs show strong sharpening of the reflections explained by accelerated ion migration between particles causing grain growth.[269–271] After reaching 450 °C, $CsPbBr_3$ reflections progressively lose intensity, and peaks corresponding to Cs_4PbBr_6 become visible, shifted to lower angles because of thermal expansion of the lattice. This experiment demonstrates that $CsPbBr_3$ converts to Cs_4PbBr_6 necessarily releasing $PbBr_2$. This reaction could be enhanced by the binding affinity of $PbBr_2$ to PbS surface dangling bonds.[272,273] Control experiments with $CsPbBr_3$ and Cs_4PbBr_6 pure phases showed that both phases are recovered after heating up to 500 °C and cooling down to room temperature, and do not undergo any transformation on their own. Besides, annealing induces crystal grain growth in pure PbS NCs, evidenced by the narrowing of the XRD reflections and scanning electron microscopy (SEM) images (Figure 2.1.4). The addition of $CsPbBr_3$ enhances the growth of the PbS crystal domains leading to even narrower reflections. This enhancement can be explained by the presence of $PbBr_2$, a phase with high solubility in PbS[274] and a large difference in melting point, which lowers the activation energy for diffusion.[275–277] Since no reflections associated with $PbBr_2$ are visible, we considered the possibility of other phases in the PbS-$PbBr_2$ phase diagram being formed. Still, $Pb_7S_2Br_{10}$, the only stable phase, was not observed in the diffraction patterns.[274] Recently the metastable phase $Pb_4S_3Br_2$ was reported in NCs, this phase is not present in the XRD patterns and we disregarded it because of the high temperature

and long reaction time, not compatible with such a kinetically stabilized phase.[278] Previous studies showed pure $CsPbBr_3$ NCs undergo partial transformation to the lead-rich $CsPb_2Br_5$, this phase is neither present in our experiments.[271] These observations suggest that bromide substitutes sulfide in PbS doping the matrix as expressed in the chemical reactions in Figure 2.1.1.

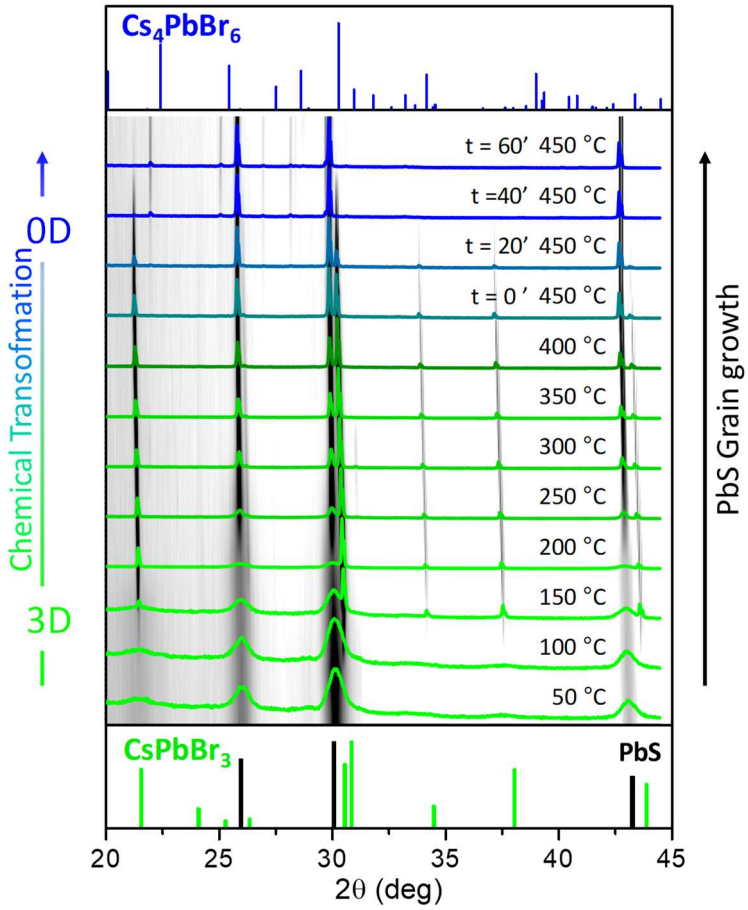

Figure 2.1.3. X-ray diffraction patterns of a mixture of PbS NCs and $CsPbBr_3$ NCs at different temperatures together with the reference patterns for the different crystal phases. In the 450 °C patterns '*t*' indicates the time held at 450 °C before measurement. The patterns are overlapped with a 2D intensity plot to help to identify low intensity reflections (PbS PDF 00-002-0699, $CsPbBr_3$ PDF 00-054-0753, Cs_4PbBr_6 PDF 01-075-0412).

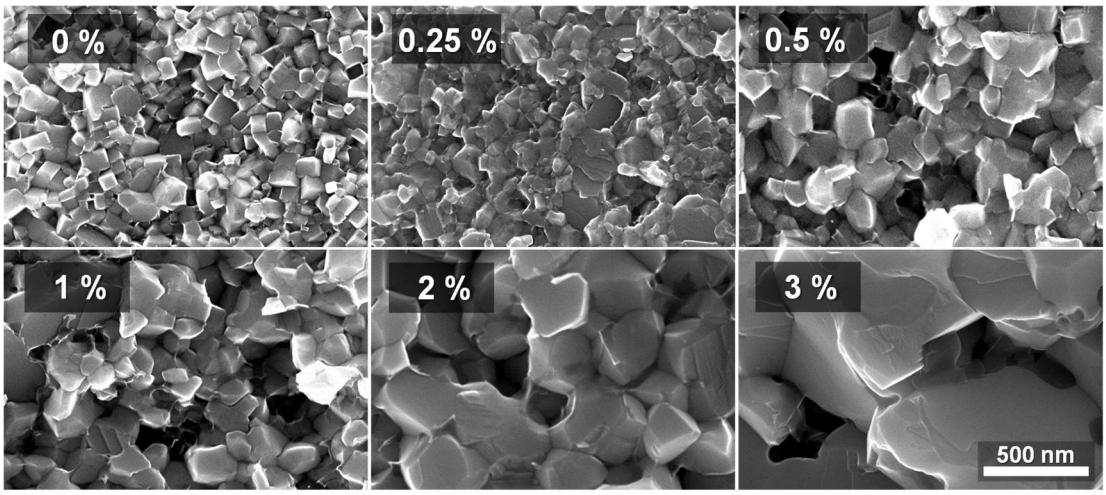

Figure 2.1.4: SEM of cleaved PbS pellets with increasing perovskite concentration.

To test the doping efficiency, we prepared pellets with the proper nominal $CsPbBr_3$ concentrations to achieve charge carrier concentrations between 10^{19} and 10^{20} cm^{-3}, which is close to the optimal charge carrier concentration for thermoelectrics.[4,279] The nominal molar amount of Br introduced is referred to the amount of S, X% = 0.25, 0.50, 1, 2, 3.

Figure 2.1.5.A and B show electrical conductivity and Seebeck coefficient of the samples between room temperature and 900 K, respectively. The absolute value of the Seebeck coefficient decreases and the electrical conductivity increases with the starting concentration of $CsPbBr_3$, proving the doping effect of the transformation.[279] Besides, the negative sign of the Seebeck coefficient confirms the *n*-type character of the obtained nanocomposites. These results are consistent with the charge carrier concentrations measured by Hall effect (Table 2.1.1) which correspond exactly to one-half of the total Br concentration, as expected from the reaction in Figure 2.1.1. As the temperature increases the absolute value of the Seebeck coefficient initially increases until a certain temperature at which changes its trend. This is related to the thermal excitation of minority carriers (bipolar effect). The higher the doping level the higher is the temperature at which this effect starts occurring.[268] The doping effect of $CsPbBr_3$ is independent of the use of NCs, ground perovskite crystals react with PbS in the same way. However, NCs provide a much shorter ion diffusion path and better mixing with PbS which leads to faster kinetics.

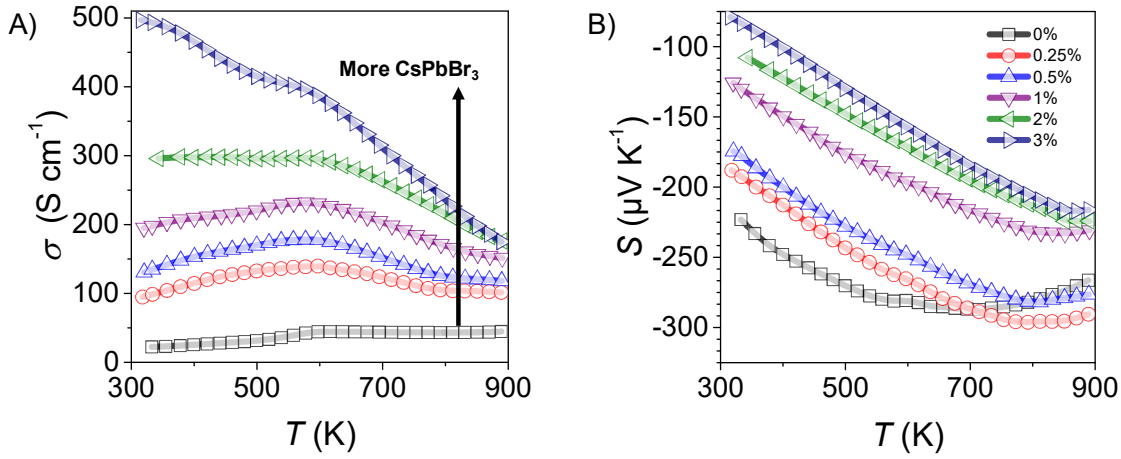

Figure 2.1.5. A) Electrical conductivity and B) Seebeck coefficient of the nanocomposites with increasing starting $CsPbBr_3$ concentration.

Table 2.1.1: Hall effect measurements of charge carrier concentration of the nanocomposites with low perovskite content.

% Br	*T* (K)	*n* (cm^{-3})	μ ($cm^2V^{-1}s^{-1}$)
0%	296	1.5×10^{17}	84
0.25 %	443	2.1×10^{19}	23
0.5 %	428	4.6×10^{19}	17

The XRD patterns of the produced pellets show no $CsPbBr_3$ nor Cs_4PbBr_6 reflections, which we associate with the low content of perovskite required for the doping level targeted. To demonstrate that the pelletized material contains Cs_4PbBr_6, we evaluated the microscopic structure of the bulk nanocomposites (Figure 2.1.6) by high-resolution transmission electron microscopy (HRTEM). A 0.5 % pellet was thinned to electron transparency by Ar^+ polishing to produce a self-suspended lamella. Figure 2.1.6.D shows an HRTEM micrograph obtained from a large PbS grain (defined as the matrix) containing multiple precipitates. The power spectrum of the highlighted area shows diffraction spots of the matrix and the precipitates, along with satellite spots of the Moiré fringes, which are formed due to orientation differences between the matrix and precipitates. Inverse Fourier (frequency) filtering of the power spectrum allowed mapping the matrix and the nanodomains. The matrix phase (in red) is identified as FCC PbS (Space group Fm3m) with a lattice parameter a = 0.5936 nm visualized along its [011] axis. The nanodomain (in green) corresponds to the same PbS phase visualized along the [001] zone axis. We performed the same analysis on the precipitate marked in Figure 2.1.6.E. The diffraction spots observed in the power spectrum correspond to the matrix phase (in red) visualized along its [011] axis. The spots of the precipitate correspond to the hexagonal Cs_4PbBr_6 phase (space group R-3c:H) with lattice parameters a = 1.373 nm and c = 1.732 nm, which is visualized along their [1-102] zone axis. Due to the difficulty to analyze all the precipitates crystallographically, to evaluate their nature we performed energy dispersion X-ray line scans across many precipitates. We found that they show no difference in composition with the matrix, proving that the vast majority of precipitates are PbS. The scans also show a small content of Br evenly distributed through the nanocomposites as expected in its role as a dopant. In short, HRTEM revealed that the doped samples are composed of a PbS matrix with a large amount of PbS

nanodomains and randomly distributed Cs_4PbBr_6 nanoprecipitates confirming the chemical transformation observed by XRD.

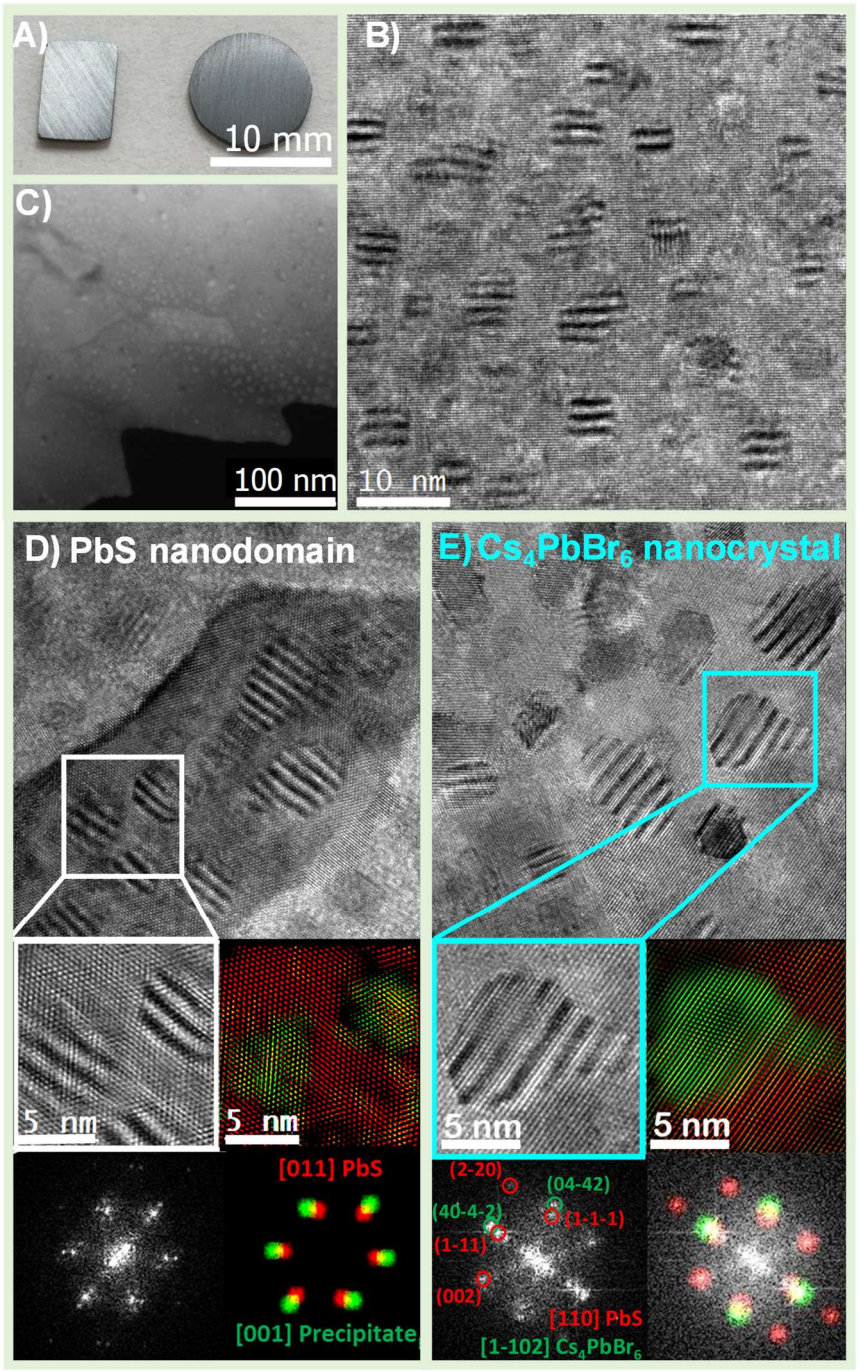

Figure 2.1.6. Structural analysis of a PbS-Cs_4PbBr_6 nanocomposite. The TEM sample is a self-suspended lamella prepared by Ar^+ ion milling. A) Photograph of the pellets used to measure the electrical conductivity and the Seebeck coefficient. B) HRTEM micrograph and C) low magnification high-angle annular dark field scanning transmission microscopy (HAADF-STEM) micrograph revealing the presence of small precipitates along the grains. D) PbS nanodomains, detail of the white squared area and its corresponding power spectrum and structural maps of the PbS matrix (in red) and nanodomains (in green) along with the applied maps for inverse Fourier filtering. E) detail of a Cs_4PbBr_6 nanoprecipitate and its corresponding power spectrum and structural maps of the PbS matrix (in red) and a Cs_4PbBr_6 precipitate (in green) are shown along with the applied maps for inverse Fourier filtering.

In summary, we showed that $CsPbBr_3$ and PbS react to give the lead depleted Cs_4PbBr_6 phase. The byproduct of the transformation, $PbBr_2$, dissolves in the PbS matrix leading to doped nanocomposites and inducing grain growth while Cs_4PbBr_6 forms nanoprecipitates. We made use of this transformation to simultaneously dope and introduce a secondary phase in *n*-type PbS nanocomposites. These results validate this new doping strategy for nanocomposites based on NC blending that involves the reaction of one of the components. This approach is not limited to the preparation of bulk samples at high pressures but could also be applied to the preparation of films or other nanocomposites since the reaction that leads to doping is also demonstrated at ambient pressure. Finally, our results reassess the intrinsic instability of metal halide perovskites and are therefore of high relevance for applications where these materials are exposed to high energy densities.

The current chapter was adapted from the cited publication (ACS Energy Lett. 2021, 6, 2, 581–587). Experimental details and supporting information that were not included in this chapter can be found there.

Conclusions

The use of colloidal nanoparticles (NPs) as precursors for dense polycrystalline solids became well-established during the past decade as the advantages of this approach were proved.[93,97,179,280–283] Different from powders produced by conventional methods, such as solid-state synthesis, particles synthesized in solution allow precise control over particle size, shape, composition, crystal phase and surface chemistry. In this thesis I explore the synthesis, surface chemistry and consolidation of colloidal particles and the transformations that they undergo during their processing into dense polycrystalline solids.

Firstly, I present the studies on the surface chemistry of two orthogonally different systems. Chapter 1.1 dives into the synthesis of sterically-stabilized metal oxide NPs by a well-established surfactant-assisted method. In these systems, the particles are known to be stabilized by surfactants, often by those present in the starting reaction mixture. However, we find that these particles have a very counterintuitive surface chemistry; the surface species are a byproduct of the reaction. This shows that even in simple systems we need to take a second look at the ligands since **the surface chemistry cannot be simply 'guessed'**.

Chapter 1.2 elaborates on electrostatically stabilized colloidal particles that are used extensively in thermoelectrics because they are free of insulating organic surfactants. Given that the synthesis is surfactant-free, the **particles were generally considered 'naked'**, in other words, without any particular surface species. We prove that in electrostatically stabilized particles, **the presence of ionic surface adsorbates is unavoidable**. These ions balance the charge of the colloids and remain on the particles during annealing and consolidation, profoundly altering the microstructure and the transport properties. It was this realization that led to the use of labile charge balancing ions, which can decompose during the annealing and are not present in the final material. In the combination of these two works, where I focus on the synthesis and surface chemistry of colloidal NPs, I learn that even in long-established syntheses, there are unexpected impurities. The surface, in particular, is a place where these impurities can 'hide', since they are studied with different methods than the core of the particles. Consequently, **studies of the surface chemistry of colloids are imperative to complement our understanding of the syntheses and of the composition and structure of the materials**.

In the second chapter, I present results on the transformation of colloidal NPs into dense polycrystalline semiconductors. I first show results on how the electrostatically stabilized colloids introduced in Chapter 1.2 can be surface engineered to incorporate multiscale defects in the consolidated solid. Such defects reduce the thermal conductivity of the material and lead to a record-high thermoelectric figure of merit. This work demonstrates how **carefully chosen surface treatments can be used to modulate the microstructure evolution** during the thermal processing. Besides, this work opened questions regarding coarsening in semiconductors and how it can be controlled.

In Chapter 2.2, I present a work on mixtures of colloidal NPs. Here, I exploit the intrinsic instability of lead halide perovskite NPs to dope NP-based nanocomposites. During annealing and consolidation, the perovskite reacts, and the byproduct increases the charge carrier concentration of the host material. **Besides devising a new doping strategy, we unravel an unknown reaction path of perovskites, contributing to the understanding of their stability**. In this case, the chemical lability (instability) of lead halide perovskite NPs was known, but the products were not. Only through a detailed characterization of the transformations we learned what happens to these materials, how they dope, and how this could be translated to other systems.

Overall, the work contained in this thesis shows that every step in the processing of NPs into dense nanocomposites can be a determining factor for the microstructure, composition, and properties of the materials. Therefore, the chemistry of each step of the process needs to be carefully studied for every material system. This might seem cumbersome, but in this complexity lies the beauty of the field: **by carefully adjusting the intricated chemistry of the systems we could create new materials and learn about their physics.**

Perspective

Finally, despite the enormous potential of NP-based solids, I believe that the community still faces some important obstacles:

1- **Lack of understanding of the chemistry of solution-processed particles**.
I showed that even in 'well-established' and widespread syntheses, there is often a lack of understanding of the chemical composition and surface chemistry of the starting NPs. NP-based solids attract the attention of researchers with very different backgrounds. Thus, the chemistry is frequently simplified and sometimes misinterpreted. One needs to bear in mind that, different from solid-state syntheses, in solution-based syntheses, not all the precursors used remain after processing and not all the byproducts can be effectively washed away. This calls to re-evaluate the syntheses used, to understand the role of each chemical, if they can be replaced, and if they have any unwanted or unexpected effect on the materials. While most of the work presented here uses NPs to produce thermoelectric materials, this also applies to other fields using NPs as precursors, such as catalysis, photovoltaics and (opto-) electronics.

2- **Misconceptions and ambiguous use of terminology.**
As a further consequence of the convergence of different fields, it is common to find mixed terminology to explain experimental observations. For example, the term 'sintering' can refer to a densification method or to the formation of grain boundaries between isolated grains ('necking'). A further example is the use of 'grain growth' to refer to any coarsening phenomenon, when it specifically refers to coarsening through grain boundary migration. This often leads to the incorrect interpretation of results and literature and hinders the communication with researchers from other fields such as metallurgy and ceramics.

3- **Grain growth and coarsening are almost unexplored in semiconductors.**
In the studied systems, we observed that the surface species in the precursor particles have a strong impact on the final grain size of the materials. A literature search on the topic reveals that while grain growth and other coarsening phenomena are well studied in metals and oxide ceramics, there is very little research done in semiconductors. As a consequence, we lack the theoretical bases to discuss coarsening. Fundamental and systematic studies on the effect of composition (intrinsic defects) and doping (extrinsic defects) on semiconductor coalescence, sintering, and grain growth are required. Such studies are imperative to achieve the goal of preparing materials with tailored, targeted features and ensuring their long-term stability.

In my opinion, any effort in overcoming these hurdles will enrich the research on colloidal nanoparticle-based solids. Given that the field is still in an infant stage, understanding the limits set by the materials' chemistry and physics might be even more significant than merely seeking marginal improvements in the material performances.

References

(1) Van Embden, J.; Chesman, A. S. R.; Jasieniak, J. J. The Heat-up Synthesis of Colloidal Nanocrystals. *Chem. Mater.* **2015**, *27* (7), 2246–2285.

(2) Heuer-Jungemann, A.; Feliu, N.; Bakaimi, I.; Hamaly, M.; Alkilany, A.; Chakraborty, I.; Masood, A.; Casula, M. F.; Kostopoulou, A.; Oh, E.; Susumu, K.; Stewart, M. H.; Medintz, I. L.; Stratakis, E.; Parak, W. J.; Kanaras, A. G. The Role of Ligands in the Chemical Synthesis and Applications of Inorganic Nanoparticles. *Chem. Rev.* **2019**, *119* (8), 4819–4880.

(3) Lesnyak, V.; Yarema, M.; Miao, S. *Colloidal Semiconductor Nanocrystals: Synthesis, Properties, and Applicationsnull*; 2020.

(4) Ortega, S.; Ibáñez, M.; Liu, Y.; Zhang, Y.; Kovalenko, M. V.; Cadavid, D.; Cabot, A. Bottom-up Engineering of Thermoelectric Nanomaterials and Devices from Solution-Processed Nanoparticle Building Blocks. *Chem. Soc. Rev.* **2017**, *46* (12), 3510–3528.

(5) Sargent, E. H. Colloidal Quantum Dot Solar Cells. *Nature Photonics*. Nature Publishing Group 2012, pp 133–135.

(6) Kovalenko, M. V.; Manna, L.; Cabot, A.; Hens, Z.; Talapin, D. V.; Kagan, C. R.; Klimov, V. I.; Rogach, A. L.; Reiss, P.; Milliron, D. J.; Guyot-Sionnnest, P.; Konstantatos, G.; Parak, W. J.; Hyeon, T.; Korgel, B. A.; Murray, C. B.; Heiss, W. Prospects of Nanoscience with Nanocrystals. *ACS Nano* **2015**, *9* (2), 1012–1057.

(7) Yin, Y.; Alivisatos, A. P. Colloidal Nanocrystal Synthesis and the Organic-Inorganic Interface. *Nature* **2005**, *437* (7059), 664–670.

(8) Ibáñez, M.; Zamani, R.; Li, W.; Cadavid, D.; Gorsse, S.; A. Katcho, N.; Shavel, A.; M. López, A.; Ramon Morante, J.; Arbiol, J.; Cabot, A. Crystallographic Control at the Nanoscale To Enhance Functionality: Polytypic Cu2GeSe3 Nanoparticles as Thermoelectric Materials. *Chem. Mater.* **2012**, *24* (23), 4615–4622.

(9) Soriano, R. B.; Wu, J.; Kanatzidis, M. G. Size as a Parameter to Stabilize New Phases: Rock Salt Phases of $Pb_mSb_{2n}Se_{M+3n}$. *J. Am. Chem. Soc.* **2015**, *137* (31), 9937–9942.

(10) Mainz, R.; Singh, A.; Levcenko, S.; Klaus, M.; Genzel, C.; Ryan, K. M.; Unold, T. Phase-Transition-Driven Growth of Compound Semiconductor Crystals from Ordered Metastable Nanorods. *Nat. Commun. 2014 51* **2014**, *5* (1), 1–10.

(11) Zhang, G.; Fang, H.; Yang, H.; Jauregui, L. A.; Chen, Y. P.; Wu, Y. Design Principle of Telluride-Based Nanowire Heterostructures for Potential Thermoelectric Applications. *Nano Lett.* **2012**, *12* (7), 3627–3633.

(12) Figuerola, A.; Huis, M. Van; Zanella, M.; Genovese, A.; Marras, S.; Falqui, A.; Zandbergen, H. W.; Cingolani, R.; Manna, L. Epitaxial CdSe-Au Nanocrystal Heterostructures by Thermal Annealing. *Nano Lett.* **2010**, *10* (8), 3028–3036.

(13) Zhang, G.; Wang, W.; Li, X. Enhanced Thermoelectric Properties of Core/Shell Heterostructure Nanowire Composites. *Adv. Mater.* **2008**, *20* (19), 3654–3656.

(14) Hens, Z.; De Roo, J. Atomically Precise Nanocrystals. *J. Am. Chem. Soc.* **2020**, *142* (37), 15627–15637.

(15) Loiudice, A.; Buonsanti, R. Reaction Intermediates in the Synthesis of Colloidal Nanocrystals. *Nat. Synth.* **2022**, *1* (5), 344–351.

(16) Calvin, J. J.; Brewer, A. S.; Alivisatos, A. P. The Role of Organic Ligand Shell Structures in Colloidal Nanocrystal Synthesis. *Nat. Synth.* **2022**, *1* (2), 127–137.

(17) Mohapatra, P.; Shaw, S.; Mendivelso-Perez, D.; Bobbitt, J. M.; Silva, T. F.; Naab, F.; Yuan, B.; Tian, X.; Smith, E. A.; Cademartiri, L. Calcination Does Not Remove All Carbon from Colloidal Nanocrystal Assemblies. *Nat. Commun.* **2017**, *8* (1), 2038.

(18) Cargnello, M.; Chen, C.; T. Diroll, B.; V. T. Doan-Nguyen, V.; J. Gorte, R.; B. Murray, C. Efficient Removal

of Organic Ligands from Supported Nanocrystals by Fast Thermal Annealing Enables Catalytic Studies on Well-Defined Active Phases. *J. Am. Chem. Soc.* **2015**, *137* (21), 6906–6911.

(19) Nag, A.; Kovalenko, M. V.; Lee, J. S.; Liu, W.; Spokoyny, B.; Talapin, D. V. Metal-Free Inorganic Ligands for Colloidal Nanocrystals: S^{2-}, HS^{-}, Se^{2-}, HSe^{-}, Te^{2-}, HTe^{-}, TeS_3^{2-}, OH^{-}, and NH^{2-} as Surface Ligands. *J. Am. Chem. Soc.* **2011**, *133* (27), 10612–10620.

(20) Owen, J. S.; Park, J.; Trudeau, P. E.; Alivisatos, A. P. Reaction Chemistry and Ligand Exchange at Cadmium-Selenide Nanocrystal Surfaces. *J. Am. Chem. Soc.* **2008**, *130* (37), 12279–12281.

(21) Zaberca, O.; Gillorin, A.; Durand, B.; Chane-Ching, J. Y. A General Route to the Synthesis of Surfactant-Free, Solvent-Dispersible Ternary and Quaternary Chalcogenide Nanocrystals. *J. Mater. Chem.* **2011**, *21* (18), 6483–6486.

(22) Pinna, N.; Niederberger, M. Surfactant-Free Nonaqueous Synthesis of Metal Oxide Nanostructures. *Angewandte Chemie - International Edition*. John Wiley & Sons, Ltd July 7, 2008, pp 5292–5304.

(23) Liu, Y.; Calcabrini, M.; Yu, Y.; Genç, A.; Chang, C.; Costanzo, T.; Kleinhanns, T.; Lee, S.; Llorca, J.; Cojocaru-Mirédin, O.; Ibáñez, M.; Liu, Y.; Calcabrini, M.; Chang, C.; Costanzo, T.; Kleinhanns, T.; Lee, S.; Ibáñez, M.; Yu, Y.; Cojocaru-Mirédin, O.; Aachen, R.; Genç, A. The Importance of Surface Adsorbates in Solution-Processed Thermoelectric Materials: The Case of SnSe. *Adv. Mater.* **2021**, 2106858.

(24) Liu, Y.; Calcabrini, M.; Yu, Y.; Lee, S.; Chang, C.; David, J.; Ghosh, T.; Spadaro, M. C.; Xie, C.; Cojocaru-Mirédin, O.; Arbiol, J.; Ibáñez, M. Defect Engineering in Solution-Processed Polycrystalline SnSe Leads to High Thermoelectric Performance. *ACS Nano* **2022**, *16* (1), 78–88.

(25) Purkayastha, A.; Kim, S.; Gandhi, D. D.; Ganesan, P. G.; Borca-Tasciuc, T.; Ramanath, G. Molecularly Protected Bismuth Telluride Nanoparticles: Microemulsion Synthesis and Thermoelectric Transport Properties. *Adv. Mater.* **2006**, *18* (22), 2958–2963.

(26) Dirmyer, M. R.; Martin, J.; Nolas, G. S.; Sen, A.; Badding, J. V. Thermal and Electrical Conductivity of Size-Tuned Bismuth Telluride Nanoparticles. *Small* **2009**, *5* (8), 933–937.

(27) Roduner, E. Size Matters: Why Nanomaterials Are Different. *Chem. Soc. Rev.* **2006**, *35* (7), 583–592.

(28) Cherniukh, I.; Rainò, G.; Stöferle, T.; Burian, M.; Travesset, A.; Naumenko, D.; Amenitsch, H.; Erni, R.; Mahrt, R. F.; Bodnarchuk, M. I.; Kovalenko, M. V. Perovskite-Type Superlattices from Lead Halide Perovskite Nanocubes. *Nature* **2021**, *593* (7860), 535–542.

(29) Coropceanu, I.; Janke, E. M.; Portner, J.; Haubold, D.; Nguyen, T. D.; Das, A.; Tanner, C. P. N.; Utterback, J. K.; Teitelbaum, S. W.; Hudson, M. H.; Sarma, N. A.; Hinkle, A. M.; Tassone, C. J.; Eychmüller, A.; Limmer, D. T.; de la Cruz, M. O.; Ginsberg, N. S.; Talapin, D. V. Self-Assembly of Nanocrystals into Strongly Electronically Coupled All-Inorganic Supercrystals. *Science* **2022**, *375* (6587), 1422–1426.

(30) Boles, M. A.; Engel, M.; Talapin, D. V. Self-Assembly of Colloidal Nanocrystals: From Intricate Structures to Functional Materials. *Chem. Rev.* **2016**, *116* (18), 11220–11289.

(31) Fiedler, C.; Kleinhanns, T.; Garcia, M.; Lee, S.; Calcabrini, M.; Ibáñez, M. Solution-Processed Inorganic Thermoelectric Materials: Opportunities and Challenges ∇. *Chemistry of Materials*. 2022, pp 8471–8489.

(32) Gomes, R.; Hassinen, A.; Szczygiel, A.; Zhao, Q.; Vantomme, A.; Martins, J. C.; Hens, Z. Binding of Phosphonic Acids to CdSe Quantum Dots: A Solution NMR Study. *J. Phys. Chem. Lett.* **2011**, *2* (3), 145–152.

(33) Jansons, A. W.; Hutchison, J. E. Continuous Growth of Metal Oxide Nanocrystals: Enhanced Control of Nanocrystal Size and Radial Dopant Distribution. *ACS Nano* **2016**, *10* (7), 6942–6951.

(34) Geisenhoff, J. Q.; Tamura, A. K.; Schimpf, A. M. Using Ligands to Control Reactivity, Size and Phase in the Colloidal Synthesis of WSe_2 Nanocrystals. *Chem. Commun.* **2019**, *55* (60), 8856–8859.

(35) Berestok, T.; Guardia, P.; Blanco, J.; Nafria, R.; Torruella, P.; López-Conesa, L.; Estradé, S.; Ibáñez, M.; De Roo, J.; Luo, Z.; Cadavid, D.; Martins, J. C.; Kovalenko, M. V.; Peiró, F.; Cabot, A. Tuning Branching in Ceria Nanocrystals. *Chem. Mater.* **2017**, *29* (10), 4418–4424.

(36) An, K.; Kwon, S. G.; Park, M.; Na, H. Bin; Baik, S. I.; Yu, J. H.; Kim, D.; Son, J. S.; Kim, Y. W.; Song, I. C.; Moon, W. K.; Park, H. M.; Hyeon, T. Synthesis of Uniform Hollow Oxide Nanoparticles through Nanoscale Acid Etching. *Nano Lett.* **2008**, *8* (12), 4252–4258.

(37) Soon, G. K.; Hyeon, T. Colloidal Chemical Synthesis and Formation Kinetics of Uniformly Sized Nanocrystals of Metals, Oxides, and Chalcogenides. *Acc. Chem. Res.* **2008**, *41* (12), 1696–1709.

(38) Kim, K.; Reimnitz, L. C.; Cho, S. H.; Noh, J.; Dong, Z.; Gibbs, S. L.; Korgel, B. A.; Milliron, D. J. Effect of Nonincorporative Cations on the Size and Shape of Indium Oxide Nanocrystals. *Chem. Mater.* **2020**, *32* (21), 9347–9354.

(39) Sytnyk, M.; Kirchschlager, R.; Bodnarchuk, M. I.; Primetzhofer, D.; Kriegner, D.; Enser, H.; Stangl, J.; Bauer, P.; Voith, M.; Hassel, A. W.; Krumeich, F.; Ludwig, F.; Meingast, A.; Kothleitner, G.; Kovalenko, M. V.; Heiss, W. Tuning the Magnetic Properties of Metal Oxide Nanocrystal Heterostructures by Cation Exchange. *Nano Lett.* **2013**, *13* (2), 586–593.

(40) Liu, Y.; Cadavid, D.; Ibáñez, M.; De Roo, J.; Ortega, S.; Dobrozhan, O.; Kovalenko, M.; Cabot, A. Colloidal $AgSbSe_2$ Nanocrystals: Surface Analysis, Electronic Doping and Processing into Thermoelectric Nanomaterials. *J. Mater. Chem. C* **2016**, *4* (21), 4756–4762.

(41) Yarema, O.; Yarema, M.; Wood, V. Tuning the Composition of Multicomponent Semiconductor Nanocrystals: The Case of I-III-VI Materials. *Chem. Mater.* **2018**, *30* (5), 1446–1461.

(42) De Roo, J.; Van Den Broeck, F.; De Keukeleere, K.; Martins, J. C.; Van Driessche, I.; Hens, Z. Unravelling the Surface Chemistry of Metal Oxide Nanocrystals, the Role of Acids and Bases. *J. Am. Chem. Soc.* **2014**, *136* (27), 9650–9657.

(43) Yang, Y.; Qin, H.; Jiang, M.; Lin, L.; Fu, T.; Dai, X.; Zhang, Z.; Niu, Y.; Cao, H.; Jin, Y.; Zhao, F.; Peng, X. Entropic Ligands for Nanocrystals: From Unexpected Solution Properties to Outstanding Processability. *Nano Lett.* **2016**, *16* (4), 2133–2138.

(44) Knowles, K. E.; Tagliazucchi, M.; Malicki, M.; Swenson, N. K.; Weiss, E. A. Electron Transfer as a Probe of the Permeability of Organic Monolayers on the Surfaces of Colloidal PbS Quantum Dots. *J. Phys. Chem. C* **2013**, *117* (30), 15849–15857.

(45) Shi, M.; Kwon, H. S.; Peng, Z.; Elder, A.; Yang, H. Effects of Surface Chemistry on the Generation of Reactive Oxygen Species by Copper Nanoparticles. *ACS Nano* **2012**, *6* (3), 2157–2164.

(46) Gabka, G.; Bujak, P.; Gryszel, M.; Kotwica, K.; Pron, A. Anchor Groups Effect on Spectroscopic and Electrochemical Properties of Quaternary Nanocrystals Cu-In-Zn-S Capped with Arylamine Derivatives. *J. Phys. Chem. C* **2015**, *119* (17), 9656–9664.

(47) Irtem, E.; Arenas Esteban, D.; Duarte, M.; Choukroun, D.; Lee, S.; Ibáñez, M.; Bals, S.; Breugelmans, T. Ligand-Mode Directed Selectivity in Cu-Ag Core-Shell Based Gas Diffusion Electrodes for CO_2 Electroreduction. *ACS Catal.* **2020**, *10* (22), 13468–13478.

(48) Elimelech, O.; Aviv, O.; Oded, M.; Banin, U. A Tale of Tails: Thermodynamics of CdSe Nanocrystal Surface Ligand Exchange. *Nano Lett.* **2020**, *20* (9), 6396–6403.

(49) Kroupa, D. M.; Vörös, M.; Brawand, N. P.; McNichols, B. W.; Miller, E. M.; Gu, J.; Nozik, A. J.; Sellinger, A.; Galli, G.; Beard, M. C. Tuning Colloidal Quantum Dot Band Edge Positions through Solution-Phase Surface Chemistry Modification. *Nat. Commun.* **2017**, *8* (1), 1–8.

(50) Anderson, N. C.; Owen, J. S. Soluble, Chloride-Terminated CdSe Nanocrystals: Ligand Exchange Monitored by ^{1}H and ^{31}P NMR Spectroscopy. *Chem. Mater.* **2013**, *25* (1), 69–76.

(51) Wei, J.; Schaeffer, N.; Pileni, M. P. Ag Nanocrystals: 1. Effect of Ligands on Plasmonic Properties. *J. Phys. Chem. B* **2014**, *118* (49), 14070–14075.

(52) Ibáñez, M.; Hasler, R.; Genç, A.; Liu, Y.; Kuster, B.; Schuster, M.; Dobrozhan, O.; Cadavid, D.; Arbiol, J.; Cabot, A.; Kovalenko, M. V. Ligand-Mediated Band Engineering in Bottom-up Assembled SnTe Nanocomposites for Thermoelectric Energy Conversion. *J. Am. Chem. Soc.* **2019**, *141* (20), 8025–8029.

(53) Vale, B. R. C.; Mourão, R. S.; Bettini, J.; Sousa, J. C. L.; Ferrari, J. L.; Reiss, P.; Aldakov, D.; Schiavon, M. A. Ligand Induced Switching of the Band Alignment in Aqueous Synthesized CdTe/CdS Core/Shell Nanocrystals. *Sci. Rep.* **2019**, *9* (1), 1–12.

(54) Boles, M. A.; Ling, D.; Hyeon, T.; Talapin, D. V. The Surface Science of Nanocrystals. *Nat. Mater.* **2016**, *15* (2), 141–153.

(55) De Roo, J.; Justo, Y.; De Keukeleere, K.; Van Den Broeck, F.; Martins, J. C.; Van Driessche, I.; Hens, Z. Carboxylic-Acid-Passivated Metal Oxide Nanocrystals: Ligand Exchange Characteristics of a New Binding Motif. *Angew. Chemie - Int. Ed.* **2015**, *54* (22), 6488–6491.

(56) Drijvers, E.; De Roo, J.; Martins, J. C.; Infante, I.; Hens, Z. Ligand Displacement Exposes Binding Site Heterogeneity on CdSe Nanocrystal Surfaces. *Chem. Mater.* **2018**, *30* (3), 1178–1186.

(57) Calvin, J. J.; O'Brien, E. A.; Sedlak, A. B.; Balan, A. D.; Alivisatos, A. P. Thermodynamics of Composition Dependent Ligand Exchange on the Surfaces of Colloidal Indium Phosphide Quantum Dots. *ACS Nano* **2021**, *15* (1), 1407–1420.

(58) Ibáñez, M.; Korkosz, R. J.; Luo, Z.; Riba, P.; Cadavid, D.; Ortega, S.; Cabot, A.; Kanatzidis, M. G. Electron Doping in Bottom-up Engineered Thermoelectric Nanomaterials through HCl-Mediated Ligand Displacement. *J. Am. Chem. Soc.* **2015**, *137* (12), 4046–4049.

(59) Liu, Y.; Gibbs, M.; Puthussery, J.; Gaik, S.; Ihly, R.; Hillhouse, H. W.; Law, M. Dependence of Carrier Mobility on Nanocrystal Size and Ligand Length in PbSe Nanocrystal Solids. *Nano Lett.* **2010**, *10* (5), 1960–1969.

(60) Ibáñez, M.; Genç, A.; Hasler, R.; Liu, Y.; Dobrozhan, O.; Nazarenko, O.; De La Mata, M.; Arbiol, J.; Cabot, A.; Kovalenko, M. V. Tuning Transport Properties in Thermoelectric Nanocomposites through Inorganic Ligands and Heterostructured Building Blocks. *ACS Nano* **2019**, *13* (6), 6572–6580.

(61) Zeng, B.; Palui, G.; Zhang, C.; Zhan, N.; Wang, W.; Ji, X.; Chen, B.; Mattoussi, H. Characterization of the Ligand Capping of Hydrophobic CdSe-ZnS Quantum Dots Using NMR Spectroscopy. *Chem. Mater.* **2018**, *30* (1), 225–238.

(62) Boles, M. A.; Talapin, D. V. Binary Assembly of PbS and Au Nanocrystals: Patchy PbS Surface Ligand Coverage Stabilizes the CuAu Superlattice. *ACS Nano* **2019**, *13* (5), 5375–5384.

(63) Moreels, I.; Justo, Y.; De Geyter, B.; Haustraete, K.; Martins, J. C.; Hens, Z. Size-Tunable, Bright, and Stable PbS Quantum Dots: A Surface Chemistry Study. *ACS Nano* **2011**, *5* (3), 2004–2012.

(64) Kessler, M. L.; Dempsey, J. L. Mapping the Topology of PbS Nanocrystals through Displacement Isotherms of Surface-Bound Metal Oleate Complexes. *Chem. Mater* **2020**, *32*, 44.

(65) Leemans, J.; Dümbgen, K. C.; Minjauw, M. M.; Zhao, Q.; Vantomme, A.; Infante, I.; Detavernier, C.; Hens, Z. Acid-Base Mediated Ligand Exchange on Near-Infrared Absorbing, Indium-Based III-V Colloidal Quantum Dots. *J. Am. Chem. Soc.* **2021**, *143* (11), 4290–4301.

(66) Hanrahan, M. P.; Stein, J. L.; Park, N.; Cossairt, B. M.; Rossini, A. J. Elucidating the Location of Cd^{2+} in Post-Synthetically Treated InP Quantum Dots Using Dynamic Nuclear Polarization ^{31}P and ^{113}Cd Solid-State NMR Spectroscopy. *J. Phys. Chem. C* **2021**, *125* (5), 2956–2965.

(67) De Keukeleere, K.; Coucke, S.; De Canck, E.; Van Der Voort, P.; Delpech, F.; Coppel, Y.; Hens, Z.; Van Driessche, I.; Owen, J. S.; De Roo, J. Stabilization of Colloidal Ti, Zr, and Hf Oxide Nanocrystals by Protonated Tri-n-Octylphosphine Oxide (TOPO) and Its Decomposition Products. *Chem. Mater.* **2017**, *29* (23), 10233–10242.

(68) Thomson, J. W.; Nagashima, K.; Macdonald, P. M.; Ozin, G. A. From Sulfur–Amine Solutions to Metal Sulfide Nanocrystals: Peering into the Oleylamine–Sulfur Black Box. *J. Am. Chem. Soc.* **2011**, *133* (13), 5036–5041.

(69) Frenette, L. C.; Krauss, T. D. Uncovering Active Precursors in Colloidal Quantum Dot Synthesis. *Nat. Commun.* **2017**, *8* (1).

(70) Liu, H.; Owen, J. S.; Alivisatos, A. P. Mechanistic Study of Precursor Evolution in Colloidal Group II-VI Semiconductor Nanocrystal Synthesis. *J. Am. Chem. Soc.* **2007**, *129* (2), 305–312.

(71) Sridaeng, D.; Limsirinawa, A.; Sirojpornphasut, P.; Chawiwannakorn, S.; Chantarasiri, N. Metal Acetylacetonate-Amine and Metal Nitrate-Amine Complexes as Low-Emission Catalysts for Rigid Polyurethane Foam Preparation. *J. Appl. Polym. Sci.* **2015**, *132* (31), 42332.

(72) Dhaene, E.; Billet, J.; Bennett, E.; Van Driessche, I.; De Roo, J. The Trouble with ODE: Polymerization during Nanocrystal Synthesis. *Nano Lett.* **2019**, *19* (10), 7411–7417.

(73) Yu, T.; Joo, J.; Park, Y. Il; Hyeon, T. Large-Scale Nonhydrolytic Sol-Gel Synthesis of Uniform-Sized Ceria Nanocrystals with Spherical, Wire, and Tadpole Shapes. *Angew. Chemie - Int. Ed.* **2005**, *44* (45), 7411–7414.

(74) Calcabrini, M.; Van den Eynden, D.; Ribot, S. S.; Pokratath, R.; Llorca, J.; De Roo, J.; Ibáñez, M. Ligand Conversion in Nanocrystal Synthesis: The Oxidation of Alkylamines to Fatty Acids by Nitrate. *JACS Au* **2021**, *1* (11), 1898–1903.

(75) Valdez, C. N.; Schimpf, A. M.; Gamelin, D. R.; Mayer, J. M. Low Capping Group Surface Density on Zinc Oxide Nanocrystals. *ACS Nano* **2014**, *8* (9), 9463–9470.

(76) De Roo, J.; Yazdani, N.; Drijvers, E.; Lauria, A.; Maes, J.; Owen, J. S.; Van Driessche, I.; Niederberger, M.; Wood, V.; Martins, J. C.; Infante, I.; Hens, Z. Probing Solvent-Ligand Interactions in Colloidal Nanocrystals by the NMR Line Broadening. *Chem. Mater.* **2018**, *30* (15), 5485–5492.

(77) Baranov, D.; Lynch, M. J.; Curtis, A. C.; Carollo, A. R.; Douglass, C. R.; Mateo-Tejada, A. M.; Jonas, D. M. Purification of Oleylamine for Materials Synthesis and Spectroscopic Diagnostics for Trans Isomers. *Chem. Mater.* **2019**, *31* (4), 1223–1230.

(78) Southern, T. M.; Wendlandt, W. W. The Thermal Decomposition of Metal Complexes-XX. Some Amine Copper(II) Nitrate Complexes. *J. Inorg. Nucl. Chem.* **1970**, *32* (12), 3783–3792.

(79) Moldoveanu, S. C. Pyrolysis of Amines and Imines. In *Techniques and Instrumentation in Analytical Chemistry*; Moldoveanu, S. C., Ed.; Elsevier, 2010; Vol. 28, pp 349–364.

(80) Hiramatsu, H.; Osterloh, F. E. A Simple Large-Scale Synthesis of Nearly Monodisperse Gold and Silver Nanoparticles with Adjustable Sizes and with Exchangeable Surfactants. *Chem. Mater.* **2004**, *16* (13), 2509–2511.

(81) Kobayashi, S.; Nagayama, S. Aldehydes vs Aldimines. Unprecedented Reactivity in Their Enolate Addition Reactions. *J. Org. Chem.* **1997**, *62* (2), 232–233.

(82) Clayden, J.; Greeves, N.; Warren, S. *Organic Chemistry*, 2nd ed.; Oxford: New York, 2012.

(83) Chen, Y.; Landes, N. T.; Little, D. J.; Beaulac, R. Conversion Mechanism of Soluble Alkylamide Precursors for the Synthesis of Colloidal Nitride Nanomaterials. *J. Am. Chem. Soc.* **2018**, *140* (33), 10421–10424.

(84) Layer, R. W. The Chemistry of Imines. *Chem. Rev.* **1963**, *63* (5), 489–510.

(85) Rawalay, S. S.; Shechter, H. Oxidation of Primary, Secondary, and Tertiary Amines with Neutral Permanganate. A Simple Method for Degrading Amines to Aldehydes and Ketones. *J. Org. Chem.* **1967**, *32* (10), 3129–3131.

(86) De Roo, J.; Van Driessche, I.; Martins, J. C.; Hens, Z. Colloidal Metal Oxide Nanocrystal Catalysis by Sustained Chemically Driven Ligand Displacement. *Nat. Mater.* **2016**, *15* (5), 517–521.

(87) Mourdikoudis, S.; Liz-Marzán, L. M. Oleylamine in Nanoparticle Synthesis. *Chem. Mater.* **2013**, *25* (9), 1465–1476.

(88) Li, Z.; Ji, Y.; Xie, R.; Grisham, S. Y.; Peng, X. Correlation of CdS Nanocrystal Formation with Elemental Sulfur Activation and Its Implication in Synthetic Development. *J. Am. Chem. Soc.* **2011**, *133* (43), 17248–17256.

(89) Kadzutu-Sithole, R.; Machogo-Phao, L. F. E.; Kolokoto, T.; Zimuwandeyi, M.; Gqoba, S. S.; Mubiayi, K.

P.; Moloto, M. J.; Van Wyk, J.; Moloto, N. Elucidating the Effect of Precursor Decomposition Time on the Structural and Optical Properties of Copper (I) Nitride Nanocubes. *RSC Adv.* **2020**, *10* (56), 34231–34246.

(90) Chen, M.; Feng, Y. G.; Wang, X.; Li, T. C.; Zhang, J. Y.; Qian, D. J. Silver Nanoparticles Capped by Oleylamine: Formation, Growth, and Self-Organization. *Langmuir* **2007**, *23* (10), 5296–5304.

(91) Zevalkink, A.; Smiadak, D. M.; Blackburn, J. L.; Ferguson, A. J.; Chabinyc, M. L.; Delaire, O.; Wang, J.; Kovnir, K.; Martin, J.; Schelhas, L. T.; Sparks, T. D.; Kang, S. D.; Dylla, M. T.; Snyder, G. J.; Ortiz, B. R.; Toberer, E. S. A Practical Field Guide to Thermoelectrics: Fundamentals, Synthesis, and Characterization. *Appl. Phys. Rev.* **2018**, *5* (2), 21303.

(92) Chandra, S.; Biswas, K. Realization of High Thermoelectric Figure of Merit in Solution Synthesized 2D SnSe Nanoplates via Ge Alloying. *J. Am. Chem. Soc.* **2019**, *141* (15), 6141–6145.

(93) Ibáñez, M.; Luo, Z.; Genç, A.; Piveteau, L.; Ortega, S.; Cadavid, D.; Dobrozhan, O.; Liu, Y.; Nachtegaal, M.; Zebarjadi, M.; Arbiol, J.; Kovalenko, M. V.; Cabot, A. High-Performance Thermoelectric Nanocomposites from Nanocrystal Building Blocks. *Nat. Commun.* **2016**, *7* (1), 10766.

(94) Park, S. H.; Jo, S.; Kwon, B.; Kim, F.; Ban, H. W.; Lee, J. E.; Gu, D. H.; Lee, S. H.; Hwang, Y.; Kim, J. S.; Hyun, D. Bin; Lee, S.; Choi, K. J.; Jo, W.; Son, J. S. High-Performance Shape-Engineerable Thermoelectric Painting. *Nat. Commun.* **2016**, *7*.

(95) Jo, S.; Choo, S.; Kim, F.; Heo, S. H.; Son, J. S. Ink Processing for Thermoelectric Materials and Power-Generating Devices. *Adv. Mater.* **2019**, *31* (20), 1804930.

(96) Liu, Y.; Zhang, Y.; Ortega, S.; Ibáñez, M.; Lim, K. H.; Grau-Carbonell, A.; Martí-Sánchez, S.; Ng, K. M.; Arbiol, J.; Kovalenko, M. V.; Cadavid, D.; Cabot, A.; Ho Lim, K.; Grau-Carbonell, A.; Martí-Sánchez, S.; Ming Ng, K.; Arbiol, J.; V. Kovalenko, M.; Cadavid, D.; Cabot, A. No Title. *Nano Lett.* **2018**, *18* (4), 2557–2563.

(97) Liu, Y.; Zhang, Y.; Lim, K. H.; Ibáñez, M.; Ortega, S.; Li, M.; David, J.; Martí-Sánchez, S.; Ng, K. M.; Arbiol, J.; Kovalenko, M. V.; Cadavid, D.; Cabot, A. High Thermoelectric Performance in Crystallographically Textured N-Type $Bi_2Te_{3-x}Se_x$ Produced from Asymmetric Colloidal Nanocrystals. *ACS Nano* **2018**, *12* (7), 7174–7184.

(98) Inorganic Nanocrystals and Surfaces: An Overview. In *RSC Nanoscience and Nanotechnology*; The Royal Society of Chemistry, 2021; Vol. 2021-Janua, pp 1–46.

(99) Ibáñez, M.; Zamani, R.; Gorsse, S.; Fan, J.; Ortega, S.; Cadavid, D.; Ramon Morante, J.; Arbiol, J.; Cabot, A. Core–Shell Nanoparticles As Building Blocks for the Bottom-Up Production of Functional Nanocomposites: PbTe–PbS Thermoelectric Properties. *ACS Nano* **2013**, *7* (3), 2573–2586.

(100) Scheele, M.; Oeschler, N.; Meier, K.; Kornowski, A.; Klinke, C.; Weller, H. Synthesis and Thermoelectric Characterization of Bi_2Te_3 Nanoparticles. *Adv. Funct. Mater.* **2009**, *19* (21), 3476–3483.

(101) Son, J. S.; Zhang, H.; Jang, J.; Poudel, B.; Waring, A.; Nally, L.; Talapin, D. V. All-Inorganic Nanocrystals as a Glue for BiSbTe Grains: Design of Interfaces in Mesostructured Thermoelectric Materials. *Angew. Chemie - Int. Ed.* **2014**, *53* (29), 7466–7470.

(102) Lou, X.; Li, S.; Chen, X.; Zhang, Q.; Deng, H.; Zhang, J.; Li, D.; Zhang, X.; Zhang, Y.; Zeng, H.; Tang, G. Lattice Strain Leads to High Thermoelectric Performance in Polycrystalline SnSe. *ACS Nano* **2021**, *15* (5), 8204–8215.

(103) Han, G.; Popuri, S. R.; Greer, H. F.; Zhang, R.; Ferre-Llin, L.; Bos, J. W. G.; Zhou, W.; Reece, M. J.; Paul, D. J.; Knox, A. R.; Gregory, D. H. Topotactic Anion-Exchange in Thermoelectric Nanostructured Layered Tin Chalcogenides with Reduced Selenium Content. *Chem. Sci.* **2018**, *9* (15), 3828–3836.

(104) Li, S.; Lou, X.; Li, X.; Zhang, J.; Li, D.; Deng, H.; Liu, J.; Tang, G. Realization of High Thermoelectric Performance in Polycrystalline Tin Selenide through Schottky Vacancies and Endotaxial Nanostructuring. *Chem. Mater.* **2020**, *32* (22), 9761–9770.

(105) Tang, G.; Wei, W.; Zhang, J.; Li, Y.; Wang, X.; Xu, G.; Chang, C.; Wang, Z.; Du, Y.; Zhao, L. D. Realizing

High Figure of Merit in Phase-Separated Polycrystalline Sn1-XPbxSe. *J. Am. Chem. Soc.* **2016**, *138* (41), 13647–13654.

(106) Li, M.; Liu, Y.; Zhang, Y.; Han, X.; Zhang, T.; Zuo, Y.; Xie, C.; Xiao, K.; Arbiol, J.; Llorca, J.; Ibáñez, M.; Liu, J.; Cabot, A. Effect of the Annealing Atmosphere on Crystal Phase and Thermoelectric Properties of Copper Sulfide. *ACS Nano* **2021**, *15* (3), 4967–4978.

(107) Wei, W.; Chang, C.; Yang, T.; Liu, J.; Tang, H.; Zhang, J.; Li, Y.; Xu, F.; Zhang, Z.; Li, J. F.; Tang, G. Achieving High Thermoelectric Figure of Merit in Polycrystalline SnSe via Introducing Sn Vacancies. *J. Am. Chem. Soc.* **2018**, *140* (1), 499–505.

(108) Gong, Y.; Chang, C.; Wei, W.; Liu, J.; Xiong, W.; Chai, S.; Li, D.; Zhang, J.; Tang, G. Extremely Low Thermal Conductivity and Enhanced Thermoelectric Performance of Polycrystalline SnSe by Cu Doping. *Scr. Mater.* **2018**, *147*, 74–78.

(109) Liu, J. J.; Wang, P.; Wang, M.; Xu, R.; Zhang, J.; Liu, J. J.; Li, D.; Liang, N.; Du, Y.; Chen, G.; Tang, G. Achieving High Thermoelectric Performance with Pb and Zn Codoped Polycrystalline SnSe via Phase Separation and Nanostructuring Strategies. *Nano Energy* **2018**, *53*, 683–689.

(110) Shi, X.; Liu, W.; Wu, A.; Nguyen, V. T.; Gao, H.; Sun, Q.; Moshwan, R.; Zou, J.; Chen, Z. Optimization of Sodium Hydroxide for Securing High Thermoelectric Performance in Polycrystalline $Sn_{1-x}Se$ via Anisotropy and Vacancy Synergy. *InfoMat* **2020**, *2* (6), 1201–1215.

(111) Shi, X.; Chen, Z. G.; Liu, W.; Yang, L.; Hong, M.; Moshwan, R.; Huang, L.; Zou, J. Achieving High Figure of Merit in P-Type Polycrystalline $Sn_{0.98}Se$ via Self-Doping and Anisotropy-Strengthening. *Energy Storage Mater.* **2018**, *10* (September 2017), 130–138.

(112) Min, Y.; Roh, J. W.; Yang, H.; Park, M.; Kim, S. Il; Hwang, S.; Lee, S. M.; Lee, K. H.; Jeong, U. Surfactant-Free Scalable Synthesis of Bi_2Te_3 and Bi_2Se_3 Nanoflakes and Enhanced Thermoelectric Properties of Their Nanocomposites. *Adv. Mater.* **2013**, *25* (10), 1425–1429.

(113) Han, G.; Popuri, S. R. R.; Greer, H. F. F.; Bos, J.-W. G. G. W. G.; Zhou, W.; Knox, A. R. R.; Montecucco, A.; Siviter, J.; Man, E. A. A.; Macauley, M.; Paul, D. J. J.; Li, W. G.; Paul, M. C. C.; Gao, M.; Sweet, T.; Freer, R.; Azough, F.; Baig, H.; Sellami, N.; Mallick, T. K. K.; Gregory, D. H. H. Facile Surfactant-Free Synthesis of p-Type SnSe Nanoplates with Exceptional Thermoelectric Power Factors. *Angew. Chemie Int. Ed.* **2016**, *55* (22), 6433–6437.

(114) Shi, X.; Zheng, K.; Hong, M.; Liu, W.; Moshwan, R.; Wang, Y.; Qu, X.; Chen, Z. G.; Zou, J. Boosting the Thermoelectric Performance of P-Type Heavily Cu-Doped Polycrystalline SnSe via Inducing Intensive Crystal Imperfections and Defect Phonon Scattering. *Chem. Sci.* **2018**, *9* (37), 7376–7389.

(115) Wang, H.; Liu, X.; Zhang, B.; Huang, L.; Yang, M.; Zhang, X.; Zhang, H.; Wang, G.; Zhou, X.; Han, G. General Surfactant-Free Synthesis of Binary Silver Chalcogenides with Tuneable Thermoelectric Properties. *Chem. Eng. J.* **2020**, *393*, 124763.

(116) Han, C.; Li, Z.; Lu, G. Q. (Max); Xue Dou, S. Robust Scalable Synthesis of Surfactant-Free Thermoelectric Metal Chalcogenide Nanostructures. *Nano Energy* **2015**, *15*, 193–204.

(117) Rosen, E. L.; Sawvel, A. M.; Milliron, D. J.; Helms, B. A. Influence of Surface Composition on Electronic Transport through Naked Nanocrystal Networks. *Chem. Mater.* **2014**, *26* (7), 2214–2217.

(118) Niu, Z.; Li, Y. Removal and Utilization of Capping Agents in Nanocatalysis. *Chemistry of Materials*. American Chemical Society January 14, 2014, pp 72–83.

(119) Doris, S. E.; Lynch, J. J.; Li, C.; Wills, A. W.; Urban, J. J.; Helms, B. A. Mechanistic Insight into the Formation of Cationic Naked Nanocrystals Generated under Equilibrium Control. *J. Am. Chem. Soc.* **2014**, *136* (44), 15702–15710.

(120) Xu, R.; Huang, L.; Zhang, J.; Li, D.; Liu, J.; Liu, J.; Fang, J.; Wang, M.; Tang, G. Nanostructured SnSe Integrated with Se Quantum Dots with Ultrahigh Power Factor and Thermoelectric Performance from Magnetic Field-Assisted Hydrothermal Synthesis. *J. Mater. Chem. A* **2019**, *7* (26), 15757–15765.

(121) Shi, X.; Wu, A.; Feng, T.; Zheng, K.; Liu, W.; Sun, Q.; Hong, M.; Pantelides, S. T.; Chen, Z.-G. G.; Zou, J. High Thermoelectric Performance in P-Type Polycrystalline Cd-Doped SnSe Achieved by a Combination of Cation Vacancies and Localized Lattice Engineering. *Adv. Energy Mater.* **2019**, *9* (11), 1803242.

(122) Shi, X.; Wu, A.; Liu, W.; Moshwan, R.; Wang, Y.; Chen, Z.-G. G.; Zou, J. Polycrystalline SnSe with Extraordinary Thermoelectric Property via Nanoporous Design. *ACS Nano* **2018**, *12* (11), 11417–11425.

(123) Li, M.; Liu, Y.; Zhang, Y.; Zuo, Y.; Li, J.; Lim, K. H.; Cadavid, D.; Ng, K. M.; Cabot, A. Crystallographically Textured SnSe Nanomaterials Produced from the Liquid Phase Sintering of Nanocrystals. *Dalt. Trans.* **2019**, *48* (11), 3641–3647.

(124) Hong, M.; Chen, Z. G.; Yang, L.; Chasapis, T. C.; Kang, S. D.; Zou, Y.; Auchterlonie, G. J.; Kanatzidis, M. G.; Snyder, G. J.; Zou, J. Enhancing the Thermoelectric Performance of $SnSe_{1-x}Te_x$ Nanoplates through Band Engineering. *J. Mater. Chem. A* **2017**, *5* (21), 10713–10721.

(125) Lee, Y. K.; Luo, Z.; Cho, S. P.; Kanatzidis, M. G.; Chung, I. Surface Oxide Removal for Polycrystalline SnSe Reveals Near-Single-Crystal Thermoelectric Performance. *Joule* **2019**, *3* (3), 719–731.

(126) Nakano, K.; Sato, T.; Tazaki, M.; Takagi, M. Self-Assembled Monolayer Formation from Decaneselenol on Polycrystalline Gold as Characterized by Electrochemical Measurements, Quartz-Crystal Microbalance, XPS, and IR Spectroscopy. *Langmuir* **2000**, *16* (5), 2225–2229.

(127) Riha, S. C.; Johnson, D. C.; Prieto, A. L. Cu_2Se Nanoparticles with Tunable Electronic Properties Due to a Controlled Solid-State Phase Transition Driven by Copper Oxidation and Cationic Conduction. *J. Am. Chem. Soc.* **2011**, *133* (5), 1383–1390.

(128) Zhu, D.; Tang, A.; Kong, Q.; Zeng, B.; Yang, C.; Teng, F. Roles of Sulfur Sources in the Formation of Alloyed $Cu_{2-x}S_ySe_{1-y}$ Nanocrystals: Controllable Synthesis and Tuning of Plasmonic Resonance Absorption. *J. Phys. Chem. C* **2017**, *121* (29), 15922–15930.

(129) Zhu, D.; Wang, L.; Liu, Z.; Tang, A. Effects of Surface Ligands on Localized Surface Plasmon Resonance and Stabilization of $Cu_{2-x}Se$ Nanocrystals. *Appl. Surf. Sci.* **2020**, *509*, 145327.

(130) Stern, O. Zur Theorie Der Elektrolytischen Doppelschicht. *Zeitschrift für Elektrochemie und Angew. Phys. Chemie* **1924**, *30* (21–22), 508–516.

(131) Ge, Z.-H. H.; Song, D.; Chong, X.; Zheng, F.; Jin, L.; Qian, X.; Zheng, L.; Dunin-Borkowski, R. E.; Qin, P.; Feng, J.; Zhao, L.-D. D. Boosting the Thermoelectric Performance of (Na,K)-Codoped Polycrystalline SnSe by Synergistic Tailoring of the Band Structure and Atomic-Scale Defect Phonon Scattering. *J. Am. Chem. Soc.* **2017**, *139* (28), 9714–9720.

(132) Cojocaru-Mirédin, O.; Abdellaoui, L.; Nagli, M.; Zhang, S.; Yu, Y.; Scheu, C.; Raabe, D.; Wuttig, M.; Amouyal, Y. Role of Nanostructuring and Microstructuring in Silver Antimony Telluride Compounds for Thermoelectric Applications. *ACS Appl. Mater. Interfaces* **2017**, *9* (17), 14779–14790.

(133) Yu, Y.; Zhou, C.; Zhang, S.; Zhu, M.; Wuttig, M.; Scheu, C.; Raabe, D.; Snyder, G. J.; Gault, B.; Cojocaru-Mirédin, O. Revealing Nano-Chemistry at Lattice Defects in Thermoelectric Materials Using Atom Probe Tomography. *Materials Today*. Elsevier B.V. January 1, 2020, pp 260–274.

(134) Hellman, O. C.; Vandenbroucke, J. A.; Rüsing, J.; Isheim, D.; Seidman, D. N. Analysis of Three-Dimensional Atom-Probe Data by the Proximity Histogram. *Microsc. Microanal.* **2000**, *6* (5), 437–444.

(135) Cantwell, P. R.; Tang, M.; Dillon, S. J.; Luo, J.; Rohrer, G. S.; Harmer, M. P. Grain Boundary Complexions. *Acta Mater.* **2014**, *62* (1), 1–48.

(136) Anderson, P. M.; Hirth, J. P.; Lothe, J. *Theory of Dislocations*, 3rd ed.; Cambridge University Press: Cambridge, 2017.

(137) Ravi, K. V. On the Observation of Bardeen-Herring Sources in Silicon. *Metall. Trans.* **1972**, *3* (5), 1311–1313.

(138) Chen, Z.; Ge, B.; Li, W.; Lin, S.; Shen, J.; Chang, Y.; Hanus, R.; Snyder, G. J.; Pei, Y. Vacancy-Induced Dislocations within Grains for High-Performance PbSe Thermoelectrics. *Nat. Commun.* **2017**, *8* (1),

13828.

(139) Chen, Z.; Jian, Z.; Li, W.; Chang, Y.; Ge, B.; Hanus, R.; Yang, J.; Chen, Y.; Huang, M.; Snyder, G. J.; Pei, Y. Lattice Dislocations Enhancing Thermoelectric PbTe in Addition to Band Convergence. *Adv. Mater.* **2017**, *29* (23), 1606768.

(140) Legros, M.; Dehm, G.; Arzt, E.; Balk, T. J. Observation of Giant Diffusivity along Dislocation Cores. *Science* **2008**, *319* (5870), 1646–1649.

(141) Yu, Y.; Zhang, S.; Mio, A. M.; Gault, B.; Sheskin, A.; Scheu, C.; Raabe, D.; Zu, F.; Wuttig, M.; Amouyal, Y.; Cojocaru-Mirédin, O. Ag-Segregation to Dislocations in PbTe-Based Thermoelectric Materials. *ACS Appl. Mater. Interfaces* **2018**, *10* (4), 3609–3615.

(142) Yamini, S. A.; Ikeda, T.; Lalonde, A.; Pei, Y.; Dou, S. X.; Snyder, G. J. Rational Design of P-Type Thermoelectric PbTe: Temperature Dependent Sodium Solubility. *J. Mater. Chem. A* **2013**, *1* (31), 8725–8730.

(143) He, J.; Blum, I. D.; Wang, H.-Q.; Girard, S. N.; Doak, J.; Zhao, L.-D.; Zheng, J.-C.; Casillas, G.; Wolverton, C.; Jose-Yacaman, M.; Seidman, D. N.; Kanatzidis, M. G.; Dravid, V. P. Morphology Control of Nanostructures: Na-Doped PbTe–PbS System. *Nano Lett.* **2012**, *12* (11), 5979–5984.

(144) Yamini, S. A.; Mitchell, D. R. G.; Gibbs, Z. M.; Santos, R.; Patterson, V.; Li, S.; Pei, Y. Z.; Dou, S. X.; Jeffrey Snyder, G. Heterogeneous Distribution of Sodium for High Thermoelectric Performance of P-Type Multiphase Lead-Chalcogenides. *Adv. Energy Mater.* **2015**, *5* (21), 1501047.

(145) Biswas, K.; He, J.; Blum, I. D.; Wu, C. I.; Hogan, T. P.; Seidman, D. N.; Dravid, V. P.; Kanatzidis, M. G. High-Performance Bulk Thermoelectrics with All-Scale Hierarchical Architectures. *Nature* **2012**, *489* (7416), 414–418.

(146) Konno, H.; Yamamoto, Y. Ylide-Metal Complexes. XIII. An X-Ray Photoelectron Spectroscopic Study of Bis(Dimethylsulfoxonium Methylide)Gold Chloride. *Bull. Chem. Soc. Jpn.* **1987**, *60* (7), 2561–2564.

(147) Bourgeat-Lami, E.; Di Renzo, F.; Fajula, F.; Mutin, P. H.; Des Courieres, T. Mechanism of the Thermal Decomposition of Tetraethylammonium in Zeolite β. *J. Phys. Chem.* **1992**, *96* (9), 3807–3811.

(148) Berr, S. S.; Coleman, M. J.; Jones, R. R. M.; Johnson, J. S. Small-Angle Neutron Scattering Study of the Structural Effects of Substitution of Tetramethylammonium for Sodium as the Counterion in Dodecyl Sulfate Micelles. *J. Phys. Chem.* **1986**, *90* (24), 6492–6499.

(149) Sangster, J.; Pelton, A. D. D. The Na-Se (Sodium-Selenium) System. *J. Phase Equilibria* **1997**, *18* (2), 185–189.

(150) Kang, S.-J. L. *Sintering*, 1st ed.; Castro, R., van Benthem, K., Eds.; Engineering Materials; Springer Berlin Heidelberg: Oxford, 2013; Vol. 35.

(151) Sutter-Fella, C. M.; Stückelberger, J. A.; Hagendorfer, H.; La Mattina, F.; Kranz, L.; Nishiwaki, S.; Uhl, A. R.; Romanyuk, Y. E.; Tiwari, A. N. Sodium Assisted Sintering of Chalcogenides and Its Application to Solution Processed $Cu_2ZnSn(S,Se)_4$ Thin Film Solar Cells. *Chem. Mater.* **2014**, *26* (3), 1420–1425.

(152) Braunger, D.; Hariskos, D.; Bilger, G.; Rau, U.; Schock, H. W. Influence of Sodium on the Growth of Polycrystalline $Cu(In,Ga)Se_2$ Thin Films. *Thin Solid Films* **2000**, *361*, 161–166.

(153) Johnson, M.; Baryshev, S. V.; Thimsen, E.; Manno, M.; Zhang, X.; Veryovkin, I. V.; Leighton, C.; Aydil, E. S. Alkali-Metal-Enhanced Grain Growth in Cu_2ZnSnS_4 Thin Films. *Energy Environ. Sci.* **2014**, *7* (6), 1931–1938.

(154) Musker, W. K. A Reinvestigation of the Pyrolysis of Tetramethylammonium Hydroxide. *J. Am. Chem. Soc.* **1964**, *86* (5), 960–961.

(155) Huang, L.; Han, G.; Zhang, B.; Gregory, D. H. Anion-Exchange Synthesis of Thermoelectric Layered $SnS_{0.1}Se_{0.9-x}Te_x$ Nano/Microstructures in Aqueous Solution: Complexity and Carrier Concentration. *J. Mater. Chem. C* **2019**, *7* (25), 7572–7579.

(156) Wei, T. R.; Tan, G.; Zhang, X.; Wu, C. F.; Li, J. F.; Dravid, V. P.; Snyder, G. J.; Kanatzidis, M. G. Distinct Impact of Alkali-Ion Doping on Electrical Transport Properties of Thermoelectric p-Type Polycrystalline SnSe. *J. Am. Chem. Soc.* **2016**, *138* (28), 8875–8882.

(157) Luo, Y.; Cai, S.; Hua, X.; Chen, H.; Liang, Q.; Du, C.; Zheng, Y.; Shen, J.; Xu, J.; Wolverton, C.; Dravid, V. P.; Yan, Q.; Kanatzidis, M. G. High Thermoelectric Performance in Polycrystalline SnSe Via Dual-Doping with Ag/Na and Nanostructuring With Ag_8SnSe_6. *Adv. Energy Mater.* **2019**, *9* (2), 1803072.

(158) Chere, E. K.; Zhang, Q.; Dahal, K.; Cao, F.; Mao, J.; Ren, Z. Studies on Thermoelectric Figure of Merit of Na-Doped p-Type Polycrystalline SnSe. *J. Mater. Chem. A* **2016**, *4* (5), 1848–1854.

(159) Zhao, L. D.; Tan, G.; Hao, S.; He, J.; Pei, Y.; Chi, H.; Wang, H.; Gong, S.; Xu, H.; Dravid, V. P.; Uher, C.; Snyder, G. J.; Wolverton, C.; Kanatzidis, M. G. Ultrahigh Power Factor and Thermoelectric Performance in Hole-Doped Single-Crystal SnSe. *Science* **2016**, *351* (6269), 141–144.

(160) Zhao, L.-D. D.; Lo, S.-H. H.; Zhang, Y.; Sun, H.; Tan, G.; Uher, C.; Wolverton, C.; Dravid, V. P.; Kanatzidis, M. G. Ultralow Thermal Conductivity and High Thermoelectric Figure of Merit in SnSe Crystals. *Nature* **2014**, *508* (7496), 373–377.

(161) Shi, G.; Kioupakis, E. Quasiparticle Band Structures and Thermoelectric Transport Properties of P-Type SnSe. *J. Appl. Phys.* **2015**, *117* (6), 065103.

(162) Zhou, Y.; Li, W.; Wu, M.; Zhao, L.-D.; He, J.; Wei, S.-H.; Huang, L. Influence of Defects on the Thermoelectricity in SnSe: A Comprehensive Theoretical Study. *Phys. Rev. B* **2018**, *97* (24), 245202.

(163) Lee, Y. K.; Ahn, K.; Cha, J.; Zhou, C.; Kim, H. S.; Choi, G.; Chae, S. I.; Park, J. H.; Cho, S. P.; Park, S. H.; Sung, Y. E.; Lee, W. B.; Hyeon, T.; Chung, I. Enhancing P-Type Thermoelectric Performances of Polycrystalline SnSe via Tuning Phase Transition Temperature. *J. Am. Chem. Soc.* **2017**, *139* (31), 10887–10896.

(164) Snyder, G. J.; Snyder, A. H.; Wood, M.; Gurunathan, R.; Snyder, B. H.; Niu, C. Weighted Mobility. *Adv. Mater.* **2020**, *32* (25), 2001537.

(165) Seto, J. Y. W. The Electrical Properties of Polycrystalline Silicon Films. *J. Appl. Phys.* **2008**, *46* (12), 5247.

(166) Slade, T. J.; Grovogui, J. A.; Kuo, J. J.; Anand, S.; Bailey, T. P.; Wood, M.; Uher, C.; Snyder, G. J.; Dravid, V. P.; Kanatzidis, M. G. Understanding the Thermally Activated Charge Transport in $NaPb_mSbQ_{M+2}$(Q = S, Se, Te) Thermoelectrics: Weak Dielectric Screening Leads to Grain Boundary Dominated Charge Carrier Scattering. *Energy Environ. Sci.* **2020**, *13* (5), 1509–1518.

(167) Jiang, C. S.; Noufi, R.; AbuShama, J. A.; Ramanathan, K.; Moutinho, H. R.; Pankow, J.; Al-Jassim, M. M. Local Built-in Potential on Grain Boundary of Cu(In,Ga)Se_2 Thin Films. *Appl. Phys. Lett.* **2004**, *84* (18), 3477–3479.

(168) Li, J. B.; Chawla, V.; Clemens, B. M. Investigating the Role of Grain Boundaries in CZTS and CZTSSe Thin Film Solar Cells with Scanning Probe Microscopy. *Adv. Mater.* **2012**, *24* (6), 720–723.

(169) Gayner, C.; Amouyal, Y. Energy Filtering of Charge Carriers: Current Trends, Challenges, and Prospects for Thermoelectric Materials. *Adv. Funct. Mater.* **2020**, *30* (18), 1901789.

(170) Martin, J.; Wang, L.; Chen, L.; Nolas, G. S. Enhanced Seebeck Coefficient through Energy-Barrier Scattering in PbTe Nanocomposites. *Phys. Rev. B - Condens. Matter Mater. Phys.* **2009**, *79* (11).

(171) Yan, Y.; Jiang, C. S.; Noufi, R.; Wei, S. H.; Moutinho, H. R.; Al-Jassim, M. M. Electrically Benign Behavior of Grain Boundaries in Polycrystalline $CuInSe_2$ Films. *Phys. Rev. Lett.* **2007**, *99* (23), 235504.

(172) Shi, X.-L.; Zheng, K.; Liu, W.-D.; Wang, Y.; Yang, Y.-Z.; Chen, Z.-G.; Zou, J. Realizing High Thermoelectric Performance in N-Type Highly Distorted Sb-Doped SnSe Microplates via Tuning High Electron Concentration and Inducing Intensive Crystal Defects. *Adv. Energy Mater.* **2018**, *8* (21), 1800775.

(173) Chang, C.; Wu, M.; He, D.; Pei, Y.; Wu, C.-F. F.; Wu, X.; Yu, H.; Zhu, F.; Wang, K.; Chen, Y.; Huang, L.; Li, J.-F. F.; He, J.; Zhao, L.-D. D. 3D Charge and 2D Phonon Transports Leading to High Out-of-Plane ZT in n-Type SnSe Crystals. *Science* **2018**, *360* (6390), 778–783.

(174) Tan, G.; Zhao, L.-D.; Kanatzidis, M. G. Rationally Designing High-Performance Bulk Thermoelectric Materials. *Chem. Rev.* **2016**, *116* (19), 12123–12149.

(175) Liu, Y.; Ibáñez, M. Tidying up the Mess. *Science* **2021**, *371* (6530), 678 LP – 679.

(176) Zhao, L. D.; Chang, C.; Tan, G.; Kanatzidis, M. G. SnSe: A Remarkable New Thermoelectric Material. *Energy Environ. Sci.* **2016**, *9* (10), 3044–3060.

(177) Chen, Z. G.; Shi, X.; Zhao, L. D.; Zou, J. High-Performance SnSe Thermoelectric Materials: Progress and Future Challenge. *Prog. Mater. Sci.* **2018**, *97*, 283–346.

(178) Banik, A.; Roychowdhury, S.; Biswas, K. The Journey of Tin Chalcogenides towards High-Performance Thermoelectrics and Topological Materials. *Chem. Commun.* **2018**, *54* (50), 6573–6590.

(179) Shi, X.; Tao, X.; Zou, J.; Chen, Z. High-Performance Thermoelectric SnSe: Aqueous Synthesis, Innovations, and Challenges. *Adv. Sci.* **2020**, *7* (7), 1902923.

(180) Qin, B.; Zhang, Y.; Wang, D.; Zhao, Q.; Gu, B.; Wu, H.; Ye, B.; Pennycook, S. J.; Zhao, L.; Zhang, H.; Ye, B.; Pennycook, S. J.; Zhao, L. Ultrahigh Average ZT Realized in P-Type SnSe Crystalline Thermoelectrics through Producing Extrinsic Vacancies Ultrahigh Average ZT Realized in p -Type SnSe Crystalline Thermoelectrics through Producing Extrinsic Vacancies. **2020**.

(181) Shi, W.; Gao, M.; Wei, J.; Gao, J.; Fan, C.; Ashalley, E.; Li, H.; Wang, Z. Tin Selenide (SnSe): Growth, Properties, and Applications. *Adv. Sci.* **2018**, *5* (4), 1700602.

(182) Qin, B.; Wang, D.; Liu, X.; Qin, Y.; Dong, J.-F.; Luo, J.; Li, J.-W.; Liu, W.; Tan, G.; Tang, X.; Li, J.-F.; He, J.; Zhao, L.-D. Momentum and Energy Multiband Alignment Enable Power Generation and Thermoelectric Cooling. *Science* **2021**, eabi8668.

(183) Xiao, Y.; Zhao, L. D. Seeking New, Highly Effective Thermoelectrics. *Science* **2020**, *367* (6483), 1196–1197.

(184) Isotta, E.; Toriyama, M. Y.; Adekoya, A. H.; Shupp, R.; Snyder, G. J.; Zevalkink, A. Effect of Sn Oxides on the Thermal Conductivity of Polycrystalline SnSe. *Mater. Today Phys.* **2023**, *31*, 100967.

(185) Zhou, C.; Lee, Y. K.; Yu, Y.; Byun, S.; Luo, Z.-Z.; Lee, H.; Ge, B.; Lee, Y.-L.; Chen, X.; Lee, J. Y.; Cojocaru-Mirédin, O.; Chang, H.; Im, J.; Cho, S.-P.; Wuttig, M.; Dravid, V. P.; Kanatzidis, M. G.; Chung, I. Polycrystalline SnSe with a Thermoelectric Figure of Merit Greater than the Single Crystal. *Nat. Mater.* **2021**.

(186) Liang, S.; Xu, J.; Noudem, J. G.; Wang, H.; Tan, X.; Liu, G.-Q. Q.; Shao, H.; Yu, B.; Yue, S.; Jiang, J. Thermoelectric Properties of Textured Polycrystalline $Na_{0.03}Sn_{0.97}Se$ Enhanced by Hot Deformation. *J. Mater. Chem. A* **2018**, *6* (46), 23730–23735.

(187) Chen, Y. X.; Ge, Z. H.; Yin, M.; Feng, D.; Huang, X. Q.; Zhao, W.; He, J. Understanding of the Extremely Low Thermal Conductivity in High-Performance Polycrystalline SnSe through Potassium Doping. *Adv. Funct. Mater.* **2016**, *26* (37), 6836–6845.

(188) Chen, C. L.; Wang, H.; Chen, Y. Y.; Day, T.; Snyder, G. J. Thermoelectric Properties of P-Type Polycrystalline SnSe Doped with Ag. *J. Mater. Chem. A* **2014**, *2* (29), 11171–11176.

(189) Wang, X.; Xu, J.; Liu, G.-Q.; Tan, X.; Li, D.; Shao, H.; Tan, T.; Jiang, J. Texturing Degree Boosts Thermoelectric Performance of Silver-Doped Polycrystalline SnSe. *NPG Asia Mater.* **2017**, *9* (8), e426–e426.

(190) Zhang, L.; Wang, J.; Sun, Q.; Qin, P.; Cheng, Z.; Ge, Z.; Li, Z.; Dou, S. Three-Stage Inter-Orthorhombic Evolution and High Thermoelectric Performance in Ag-Doped Nanolaminar SnSe Polycrystals. *Adv. Energy Mater.* **2017**, *7* (19), 1700573.

(191) Lin, C. C.; Lydia, R.; Yun, J. H.; Lee, H. S.; Rhyee, J. S. Extremely Low Lattice Thermal Conductivity and Point Defect Scattering of Phonons in Ag-Doped $(SnSe)_{1-x}(SnS)_x$ Compounds. *Chem. Mater.* **2017**, *29* (12), 5344–5352.

(192) Wang, H. X.; Mao, L. S.; Tan, X. J.; Liu, G. Q.; Xu, J. T.; Shao, H. Z.; Hu, H. Y.; Jiang, J. Nontrivial

Thermoelectric Behavior in Cubic SnSe Driven by Spin-Orbit Coupling. *Nano Energy* **2018**, *51* (April), 649–655.

(193) McCarthy, C. L.; Webber, D. H.; Schueller, E. C.; Brutchey, R. L. Solution-Phase Conversion of Bulk Metal Oxides to Metal Chalcogenides Using a Simple Thiol-Amine Solvent Mixture. *Angew. Chemie - Int. Ed.* **2015**, *54* (29), 8378–8381.

(194) Dolzhnikov, D. S.; Zhang, H.; Jang, J.; Son, J. S.; Panthani, M. G.; Shibata, T.; Chattopadhyay, S.; Talapin, D. V. Composition-Matched Molecular "Solders" for Semiconductors. *Science* **2015**, *347* (6220), 425 LP – 428.

(195) H. Hudson, M.; S. Dolzhnikov, D.; S. Filatov, A.; M. Janke, E.; Jang, J.; Lee, B.; Sun, C.; V. Talapin, D.; Hudson, M. H.; Dolzhnikov, D. S.; Filatov, A. S.; Janke, E. M.; Jang, J.; Lee, B.; Sun, C.; Talapin, D. V.; H. Hudson, M.; S. Dolzhnikov, D.; S. Filatov, A.; M. Janke, E.; Jang, J.; Lee, B.; Sun, C.; V. Talapin, D. New Forms of CdSe: Molecular Wires, Gels, and Ordered Mesoporous Assemblies. *J. Am. Chem. Soc.* **2017**, *139* (9), 3368–3377.

(196) McCarthy, C. L.; Brutchey, R. L. Solution Processing of Chalcogenide Materials Using Thiol-Amine "Alkahest" Solvent Systems. *Chem. Commun.* **2017**, *53* (36), 4888–4902.

(197) Webber, D. H.; Brutchey, R. L. Alkahest for V_2VI_3 Chalcogenides: Dissolution of Nine Bulk Semiconductors in a Diamine-Dithiol Solvent Mixture. *J. Am. Chem. Soc.* **2013**, *135* (42), 15722–15725.

(198) Chen, D.; Ghoneim, T.; Kulkarni, Y. Effect of Pinning Particles on Grain Boundary Motion from Interface Random Walk. *Appl. Phys. Lett.* **2017**, *111* (16), 161606.

(199) Nes, E.; Ryum, N.; Hunderi, O. On the Zener Drag. *Acta Metall.* **1985**, *33* (1), 11–22.

(200) Manohar, P. A.; Ferry, M.; Chandra, T. Five Decades of the Zener Equation. *ISIJ Int.* **1998**, *38* (9), 913–924.

(201) Rollett, A.; Humphreys, F.; Rohrer, G. S.; Hatherly, M. *Recrystallization and Related Annealing Phenomena: Second Edition*; Elsevier Ltd, 2004.

(202) Leute, V.; Menge, D. Thermodynamic Investigations of the Quasibinary Systems (CdKSn1-K)Te, (CdKSn1-K)Se, And Sn(SeLTe1-L). *Zeitschrift fur Phys. Chemie* **1992**, *176*, 47–64.

(203) Leute, V.; Menge, D. Thermodynamic Investigations of the Quasibinary Systems $(Cd_KSn_{1-K})Te$, $(Cd_KSn_{1-K})Se$, And $Sn(Se_LTe_{1-L})$. *Zeitschrift fur Phys. Chemie* **1992**, *176* (1), 47–64.

(204) Kh, A. N.; Bankina, V. F.; Poretskaya, L. V; Shelimova, L. E.; Skudnova, E. V. Semiconducting II–VI, IV–VI and V–VI Compounds. *NY Plenum Press* **1969**, *249*, 14.

(205) Shen, W. P.; Kwok, H. S. Highly Doped P-Type and n-Type ZnS, ZnSe, CdS and CdSe Thin Films Growth by Pulsed Laser Deposition. *Mater. Res. Soc. Symp. - Proc.* **1994**, *340*, 457–463.

(206) Kuo, J. J.; Kang, S. D.; Imasato, K.; Tamaki, H.; Ohno, S.; Kanno, T.; Snyder, G. J. Grain Boundary Dominated Charge Transport in Mg3Sb2-Based Compounds. *Energy Environ. Sci.* **2018**, *11* (2), 429–434.

(207) Wei, T.-R.; Wu, C.-F.; Zhang, X.; Tan, Q.; Sun, L.; Pan, Y.; Li, J.-F. Thermoelectric Transport Properties of Pristine and Na-Doped $SnSe_{1-x}Te_x$ Polycrystals. *Phys. Chem. Chem. Phys.* **2015**, *17* (44), 30102–30109.

(208) Zong, P. A.; Hanus, R.; Dylla, M.; Tang, Y.; Liao, J.; Zhang, Q.; Snyder, G. J.; Chen, L. Skutterudite with Graphene-Modified Grain-Boundary Complexion Enhances ZT Enabling High-Efficiency Thermoelectric Device. *Energy Environ. Sci.* **2017**, *10* (1), 183–191.

(209) Guo, R.; Wang, X.; Kuang, Y.; Huang, B. First-Principles Study of Anisotropic Thermoelectric Transport Properties of IV-VI Semiconductor Compounds SnSe and SnS. *Phys. Rev. B - Condens. Matter Mater. Phys.* **2015**, *92* (11), 115202.

(210) Shi, D.; Adinolfi, V.; Comin, R.; Yuan, M.; Alarousu, E.; Buin, A.; Chen, Y.; Hoogland, S.; Rothenberger, A.; Katsiev, K.; Losovyj, Y.; Zhang, X.; Dowben, P. A.; Mohammed, O. F.; Sargent, E. H.; Bakr, O. M. Low Trap-State Density and Long Carrier Diffusion in Organolead Trihalide Perovskite Single Crystals. *Science*

2015, *347* (6221), 519–522.

(211) Maculan, G.; Sheikh, A. D.; Abdelhady, A. L.; Saidaminov, M. I.; Haque, M. A.; Murali, B.; Alarousu, E.; Mohammed, O. F.; Wu, T.; Bakr, O. M. $CH_3NH_3PbCl_3$ Single Crystals: Inverse Temperature Crystallization and Visible-Blind UV-Photodetector. *J. Phys. Chem. Lett.* **2015**, *6* (19), 3781–3786.

(212) Saidaminov, M. I.; Abdelhady, A. L.; Murali, B.; Alarousu, E.; Burlakov, V. M.; Peng, W.; Dursun, I.; Wang, L.; He, Y.; MacUlan, G.; Goriely, A.; Wu, T.; Mohammed, O. F.; Bakr, O. M. High-Quality Bulk Hybrid Perovskite Single Crystals within Minutes by Inverse Temperature Crystallization. *Nat. Commun.* **2015**, *6* (1), 23955.

(213) Manser, J. S.; Christians, J. A.; Kamat, P. V. Intriguing Optoelectronic Properties of Metal Halide Perovskites. *Chem. Rev.* **2016**, *116* (21), 12956–13008.

(214) Fang, H. H.; Adjokatse, S.; Wei, H.; Yang, J.; Blake, G. R.; Huang, J.; Even, J.; Loi, M. A. Ultrahigh Sensitivity of Methylammonium Lead Tribromide Perovskite Single Crystals to Environmental Gases. *Sci. Adv.* **2016**, *2* (7), e1600534.

(215) Sutton, R. J.; Eperon, G. E.; Miranda, L.; Parrott, E. S.; Kamino, B. A.; Patel, J. B.; Hörantner, M. T.; Johnston, M. B.; Haghighirad, A. A.; Moore, D. T.; Snaith, H. J. Bandgap-Tunable Cesium Lead Halide Perovskites with High Thermal Stability for Efficient Solar Cells. *Adv. Energy Mater.* **2016**, *6* (8), 1502458.

(216) McMeekin, D. P.; Sadoughi, G.; Rehman, W.; Eperon, G. E.; Saliba, M.; Hörantner, M. T.; Haghighirad, A.; Sakai, N.; Korte, L.; Rech, B.; Johnston, M. B.; Herz, L. M.; Snaith, H. J. A Mixed-Cation Lead Mixed-Halide Perovskite Absorber for Tandem Solar Cells. *Science* **2016**, *351* (6269), 151–155.

(217) Liu, X. K.; Xu, W.; Bai, S.; Jin, Y.; Wang, J.; Friend, R. H.; Gao, F. Metal Halide Perovskites for Light-Emitting Diodes. *Nat. Mater.* **2020**, *20*, 10–21.

(218) Noculak, A.; Noculak, A.; Morad, V.; Morad, V.; McCall, K. M.; Yakunin, S.; Shynkarenko, Y.; Yakunin, S.; Shynkarenko, Y.; Wörle, M.; Kovalenko, M. V. Bright Blue and Green Luminescence of Sb(III) in Double Perovskite Cs_2MInCl_6(M = Na, K) Matrices. *Chem. Mater.* **2020**, *32* (12), 5118–5124.

(219) Jena, A. K.; Kulkarni, A.; Miyasaka, T. Halide Perovskite Photovoltaics: Background, Status, and Future Prospects. *Chem. Rev.* **2019**, *119* (5), 3036–3103.

(220) Brenner, P.; Bar-On, O.; Jakoby, M.; Allegro, I.; Richards, B. S.; Paetzold, U. W.; Howard, I. A.; Scheuer, J.; Lemmer, U. Continuous Wave Amplified Spontaneous Emission in Phase-Stable Lead Halide Perovskites. *Nat. Commun.* **2019**, *10* (1), 1–7.

(221) Akkerman, Q. A.; Rainò, G.; Kovalenko, M. V; Manna, L. Genesis, Challenges and Opportunities for Colloidal Lead Halide Perovskite Nanocrystals. *Nat. Mater.* **2018**, *17* (5), 394–405.

(222) Bertolotti, F.; Protesescu, L.; Kovalenko, M. V.; Yakunin, S.; Cervellino, A.; Billinge, S. J. L.; Terban, M. W.; Pedersen, J. S.; Masciocchi, N.; Guagliardi, A. Coherent Nanotwins and Dynamic Disorder in Cesium Lead Halide Perovskite Nanocrystals. *ACS Nano* **2017**, *11* (4), 3819–3831.

(223) Aebli, M.; Benin, B. M.; McCall, K. M.; Morad, V.; Thöny, D.; Grützmacher, H.; Kovalenko, M. V. White CsPbBr3: Characterizing the One-Dimensional Cesium Lead Bromide Polymorph. *Helv. Chim. Acta* **2020**, *103* (7), e2000080.

(224) Piveteau, L.; Aebli, M.; Yazdani, N.; Millen, M.; Korosec, L.; Krieg, F.; Benin, B. M.; Morad, V.; Piveteau, C.; Shiroka, T.; Comas-Vives, A.; Copéret, C.; Lindenberg, A. M.; Wood, V.; Verel, R.; Kovalenko, M. V. Bulk and Nanocrystalline Cesium Lead-Halide Perovskites as Seen by Halide Magnetic Resonance. *ACS Cent. Sci.* **2020**, *6* (7), 1138–1149.

(225) Yin, J.; Maity, P.; De Bastiani, M.; Dursun, I.; Bakr, O. M.; Brédas, J. L.; Mohammed, O. F. Molecular Behavior of Zero-Dimensional Perovskites. *Sci. Adv.* **2017**, *3* (12), e1701793.

(226) Akkerman, Q. A.; Manna, L. What Defines a Halide Perovskite? *ACS Energy Lett.* **2020**, *5* (2), 604–610.

(227) Kovalenko, M. V; Protesescu, L.; Bodnarchuk, M. I. Properties and Potential Optoelectronic Applications of Lead Halide Perovskite Nanocrystals. *Science* **2017**, *358* (6364), 745–750.

(228) Li, Y.; Huang, H.; Xiong, Y.; Kershaw, S. V.; Rogach, A. L. Reversible Transformation between $CsPbBr_3$ and Cs_4PbBr_6 Nanocrystals. *CrystEngComm* **2018**, *20* (34), 4900–4904.

(229) Palazon, F.; Urso, C.; De Trizio, L.; Akkerman, Q.; Marras, S.; Locardi, F.; Nelli, I.; Ferretti, M.; Prato, M.; Manna, L. Postsynthesis Transformation of Insulating Cs_4PbBr_6 Nanocrystals into Bright Perovskite $CsPbBr_3$ through Physical and Chemical Extraction of CsBr. *ACS Energy Lett.* **2017**, *2* (10), 2445–2448.

(230) Wu, L.; Hu, H.; Xu, Y.; Jiang, S.; Chen, M.; Zhong, Q.; Yang, D.; Liu, Q.; Zhao, Y.; Sun, B.; Zhang, Q.; Yin, Y. From Nonluminescent Cs_4PbX_6 (X = Cl, Br, I) Nanocrystals to Highly Luminescent $CsPbX_3$ Nanocrystals: Water-Triggered Transformation through a CsX-Stripping Mechanism. *Nano Lett.* **2017**, *17* (9), 5799–5804.

(231) Palazon, F.; Almeida, G.; Akkerman, Q. A.; De Trizio, L.; Dang, Z.; Prato, M.; Manna, L. Changing the Dimensionality of Cesium Lead Bromide Nanocrystals by Reversible Postsynthesis Transformations with Amines. *Chem. Mater.* **2017**, *29* (10), 4167–4171.

(232) Liu, Z.; Bekenstein, Y.; Ye, X.; Nguyen, S. C.; Swabeck, J.; Zhang, D.; Lee, S. T.; Yang, P.; Ma, W.; Alivisatos, A. P. Ligand Mediated Transformation of Cesium Lead Bromide Perovskite Nanocrystals to Lead Depleted Cs_4PbBr_6 Nanocrystals. *J. Am. Chem. Soc.* **2017**, *139* (15), 5309–5312.

(233) Zhang, X.; Wu, X.; Liu, X.; Chen, G.; Wang, Y.; Bao, J.; Xu, X.; Liu, X.; Zhang, Q.; Yu, K.; Wei, W.; Liu, J.; Xu, J.; Jiang, H.; Wang, P.; Wang, X. Heterostructural $CsPbX_3$-PbS (X = Cl, Br, I) Quantum Dots with Tunable Vis-NIR Dual Emission. *J. Am. Chem. Soc.* **2020**, *142* (9), 4464–4471.

(234) Miranti, R.; Shin, D.; Septianto, R. D.; Ibáñez, M.; Kovalenko, M. V; Matsushita, N.; Iwasa, Y.; Bisri, S. Z. Exclusive Electron Transport in Core@Shell PbTe@PbS Colloidal Semiconductor Nanocrystal Assemblies. *ACS Nano* **2020**, *14* (3), 3242–3250.

(235) Balazs, D. M.; Bijlsma, K. I.; Fang, H.-H. H.; Dirin, D. N.; Döbeli, M.; Kovalenko, M. V.; Loi, M. A. Stoichiometric Control of the Density of States in PbS Colloidal Quantum Dot Solids. *Sci. Adv.* **2017**, *3* (9), eaao1558.

(236) Gilmore, R. H.; Lee, E. M. Y.; Weidman, M. C.; Willard, A. P.; Tisdale, W. A. Charge Carrier Hopping Dynamics in Homogeneously Broadened PbS Quantum Dot Solids. *Nano Lett.* **2017**, *17* (2), 893–901.

(237) Shulga, A. G.; Kahmann, S.; Dirin, D. N.; Graf, A.; Zaumseil, J.; Kovalenko, M. V; Loi, M. A. Electroluminescence Generation in PbS Quantum Dot Light-Emitting Field-Effect Transistors with Solid-State Gating. *ACS Nano* **2018**, *12* (12), 12805–12813.

(238) Speirs, M. J.; Balazs, D. M.; Dirin, D. N.; Kovalenko, M. V.; Loi, M. A. Increased Efficiency in Pn-Junction PbS QD Solar Cells via NaHS Treatment of the p-Type Layer. *Appl. Phys. Lett.* **2017**, *110* (10), 103904.

(239) Stavrinadis, A.; Pradhan, S.; Papagiorgis, P.; Itskos, G.; Konstantatos, G. Suppressing Deep Traps in PbS Colloidal Quantum Dots via Facile Iodide Substitutional Doping for Solar Cells with Efficiency >10%. *ACS Energy Lett.* **2017**, *2* (4), 739–744.

(240) Wang, Y.; Liu, Z.; Huo, N.; Li, F.; Gu, M.; Ling, X.; Zhang, Y.; Lu, K.; Han, L.; Fang, H.; Shulga, A. G.; Xue, Y.; Zhou, S.; Yang, F.; Tang, X.; Zheng, J.; Antonietta Loi, M.; Konstantatos, G.; Ma, W. Room-Temperature Direct Synthesis of Semi-Conductive PbS Nanocrystal Inks for Optoelectronic Applications. *Nat. Commun.* **2019**, *10* (1), 1–8.

(241) Nienhaus, L.; Wu, M.; Geva, N.; Shepherd, J. J.; Wilson, M. W. B.; Bulović, V.; Van Voorhis, T.; Baldo, M. A.; Bawendi, M. G. Speed Limit for Triplet-Exciton Transfer in Solid-State PbS Nanocrystal-Sensitized Photon Upconversion. *ACS Nano* **2017**, *11* (8), 7848–7857.

(242) Saran, R.; Curry, R. J. Lead Sulphide Nanocrystal Photodetector Technologies. *Nat. Photonics* **2016**, *10* (2), 81–92.

(243) Tang, H.; Zhong, J.; Chen, W.; Shi, K.; Mei, G.; Zhang, Y.; Wen, Z.; Müller-Buschbaum, P.; Wu, D.; Wang, K.; Sun, X. W. Lead Sulfide Quantum Dot Photodetector with Enhanced Responsivity through a Two-Step Ligand-Exchange Method. *ACS Appl. Nano Mater.* **2019**, *2* (10), 6135–6143.

(244) Xu, B.; Feng, T.; Li, Z.; Pantelides, S. T.; Wu, Y. Constructing Highly Porous Thermoelectric Monoliths with High-Performance and Improved Portability from Solution-Synthesized Shape-Controlled Nanocrystals. *Nano Lett.* **2018**, *18* (6), 4034–4039.

(245) Ibáñez, M.; Hasler, R.; Liu, Y.; Dobrozhan, O.; Nazarenko, O.; Cadavid, D.; Cabot, A.; Kovalenko, M. V. Tuning P-Type Transport in Bottom-Up-Engineered Nanocrystalline Pb Chalcogenides Using Alkali Metal Chalcogenides as Capping Ligands. *Chem. Mater.* **2017**, *29* (17), 7093–7097.

(246) Dalpian, G. M.; Chelikowsky, J. R. Self-Purification in Semiconductor Nanocrystals. *Phys. Rev. Lett.* **2006**, *96* (22), 226802.

(247) Norris, D. J.; Efros, A. L.; Erwin, S. C. Doped Nanocrystals. *Science* **2008**, *319* (5871), 1776–1779.

(248) Oh, S. J.; Berry, N. E.; Choi, J.-H. H.; Gaulding, E. A.; Paik, T.; Hong, S.-H. H.; Murray, C. B.; Kagan, C. R. Stoichiometric Control of Lead Chalcogenide Nanocrystal Solids to Enhance Their Electronic and Optoelectronic Device Performance. *ACS Nano* **2013**, *7* (3), 2413–2421.

(249) Buonsanti, R.; Milliron, D. J. Chemistry of Doped Colloidal Nanocrystals. *Chem. Mater.* **2013**, *25* (8), 1305–1317.

(250) Du, M. H.; Erwin, S. C.; Efros, A. L. Trapped-Dopant Model of Doping in Semiconductor Nanocrystals. *Nano Lett.* **2008**, *8* (9), 2878–2882.

(251) Yazdani, N.; Andermatt, S.; Yarema, M.; Farto, V.; Bani-Hashemian, M. H.; Volk, S.; Lin, W. M. M.; Yarema, O.; Luisier, M.; Wood, V. Charge Transport in Semiconductors Assembled from Nanocrystal Quantum Dots. *Nat. Commun.* **2020**, *11* (1), 1–9.

(252) Ning, Z.; Voznyy, O.; Pan, J.; Hoogland, S.; Adinolfi, V.; Xu, J.; Li, M.; Kirmani, A. R.; Sun, J. P.; Minor, J.; Kemp, K. W.; Dong, H.; Rollny, L.; Labelle, A.; Carey, G.; Sutherland, B.; Hill, I.; Amassian, A.; Liu, H.; Tang, J.; Bakr, O. M.; Sargent, E. H. Air-Stable n-Type Colloidal Quantum Dot Solids. *Nat. Mater.* **2014**, *13* (8), 822–828.

(253) Nugraha, M. I.; Kumagai, S.; Watanabe, S.; Sytnyk, M.; Heiss, W.; Loi, M. A.; Takeya, J. Enabling Ambipolar to Heavy N-Type Transport in PbS Quantum Dot Solids through Doping with Organic Molecules. *ACS Appl. Mater. Interfaces* **2017**, *9* (21), 18039–18045.

(254) Robin, A.; Livache, C.; Ithurria, S.; Lacaze, E.; Dubertret, B.; Lhuillier, E. Surface Control of Doping in Self-Doped Nanocrystals. *ACS Appl. Mater. Interfaces* **2016**, *8* (40), 27122–27128.

(255) Choi, M. J.; García de Arquer, F. P.; Proppe, A. H.; Seifitokaldani, A.; Choi, J.; Kim, J.; Baek, S. W.; Liu, M.; Sun, B.; Biondi, M.; Scheffel, B.; Walters, G.; Nam, D. H.; Jo, J. W.; Ouellette, O.; Voznyy, O.; Hoogland, S.; Kelley, S. O.; Jung, Y. S.; Sargent, E. H. Cascade Surface Modification of Colloidal Quantum Dot Inks Enables Efficient Bulk Homojunction Photovoltaics. *Nat. Commun.* **2020**, *11* (1), 1–9.

(256) Wang, H.; Butler, D. J.; Straus, D. B.; Oh, N.; Wu, F.; Guo, J.; Xue, K.; Lee, J. D.; Murray, C. B.; Kagan, C. R. Air-Stable $CuInSe_2$ Nanocrystal Transistors and Circuits via Post-Deposition Cation Exchange. *ACS Nano* **2019**, *13* (2), 2324–2333.

(257) Chakraborty, P.; Jin, Y.; Barrows, C. J.; Dunham, S. T.; Gamelin, D. R. Kinetics of Isovalent (Cd^{2+}) and Aliovalent (In^{3+}) Cation Exchange in $Cd_{1-x}Mn_xSe$ Nanocrystals. *J. Am. Chem. Soc.* **2016**, *138* (39), 12885–12893.

(258) Liu, Y.; Cadavid, D.; Ibáñez, M.; Ortega, S.; Martí-Sánchez, S.; Dobrozhan, O.; Kovalenko, M. V.; Arbiol, J.; Cabot, A. Thermoelectric Properties of Semiconductor-Metal Composites Produced by Particle Blending. *APL Mater.* **2016**, *4* (10), 104813.

(259) Urban, J. J.; Talapin, D. V.; Shevchenko, E. V.; Kagan, C. R.; Murray, C. B. Synergism in Binary Nanocrystal Superlattices Leads to Enhanced P-Type Conductivity in Self-Assembled PbTe/Ag_2Te Thin Films. *Nat. Mater.* **2007**, *6* (2), 115–121.

(260) Zhao, D.; Huang, J.; Qin, R.; Yang, G.; Yu, J. Efficient Visible–Near-Infrared Hybrid Perovskite:PbS Quantum Dot Photodetectors Fabricated Using an Antisolvent Additive Solution Process. *Adv. Opt.*

Mater. **2018**, *6* (23), 1–9.

(261) Liu, C.; Peng, H.; Wang, K.; Wei, C.; Wang, Z.; Gong, X. PbS Quantum Dots-Induced Trap-Assisted Charge Injection in Perovskite Photodetectors. *Nano Energy* **2016**, *30* (July), 27–35.

(262) Piatkowski, P.; Masi, S.; Galar, P.; Gutiérrez, M.; Ngo, T. T.; Mora-Seró, I.; Douhal, A. Deciphering the Role of Quantum Dot Size in the Ultrafast Charge Carrier Dynamics at the Perovskite-Quantum Dot Interface. *J. Mater. Chem. C* **2020**, *8* (42), 14834–14844.

(263) Gong, X.; Yang, Z.; Walters, G.; Comin, R.; Ning, Z.; Beauregard, E.; Adinolfi, V.; Voznyy, O.; Sargent, E. H. Highly Efficient Quantum Dot Near-Infrared Light-Emitting Diodes. *Nat. Photonics* **2016**, *10* (4), 253–257.

(264) Ning, Z.; Gong, X.; Comin, R.; Walters, G.; Fan, F.; Voznyy, O.; Yassitepe, E.; Buin, A.; Hoogland, S.; Sargent, E. H. Quantum-Dot-in-Perovskite Solids. *Nature* **2015**, *523* (7560), 324–328.

(265) Yang, Z.; Janmohamed, A.; Lan, X.; Pelayo García De Arquer, F.; Voznyy, O.; Yassitepe, E.; Kim, G.-H.; Ning, Z.; Gong, X.; Comin, R.; Sargent, E. H. Colloidal Quantum Dot Photovoltaics Enhanced by Perovskite Shelling. *Nano Lett* **2015**, *15*, 51.

(266) Liu, M.; Chen, Y.; Tan, C. S.; Quintero-Bermudez, R.; Proppe, A. H.; Munir, R.; Tan, H.; Voznyy, O.; Scheffel, B.; Walters, G.; Kam, A. P. T.; Sun, B.; Choi, M. J.; Hoogland, S.; Amassian, A.; Kelley, S. O.; García de Arquer, F. P.; Sargent, E. H. Lattice Anchoring Stabilizes Solution-Processed Semiconductors. *Nature* **2019**, *570* (7759), 96–101.

(267) Sytnyk, M.; Yakunin, S.; Schö, W.; Lechner, R. T.; Burian, M.; Ludescher, L.; Killilea, N. A.; Yousefiamin, A.; Kriegner, D.; Stangl, J.; Groiss, H.; Heiss, W.; Schöfberger, W.; Lechner, R. T.; Burian, M.; Ludescher, L.; Killilea, N. A.; Yousefiamin, A.; Kriegner, D.; Stangl, J.; Groiss, H.; Heiss, W. Quasi-Epitaxial Metal-Halide Perovskite Ligand Shells on PbS Nanocrystals. *ACS Nano* **2017**, *11* (2), 1246–1256.

(268) Wang, H.; Schechtel, E.; Pei, Y.; Snyder, G. J. High Thermoelectric Effinciency of N-Type PbS. *Adv. Energy Mater.* **2013**, *3* (4), 488–495.

(269) Zhang, Q.; Wang, B.; Zheng, W.; Kong, L.; Wan, Q.; Zhang, C.; Li, Z.; Cao, X.; Liu, M.; Li, L. Ceramic-like Stable $CsPbBr_3$ Nanocrystals Encapsulated in Silica Derived from Molecular Sieve Templates. *Nat. Commun.* **2020**, *11* (1), 1–9.

(270) Palazon, F.; Di Stasio, F.; Lauciello, S.; Krahne, R.; Prato, M.; Manna, L. Evolution of $CsPbBr_3$ Nanocrystals upon Post-Synthesis Annealing under an Inert Atmosphere. *J. Mater. Chem. C* **2016**, *4* (39), 9179–9182.

(271) Palazon, F.; Dogan, S.; Marras, S.; Locardi, F.; Nelli, I.; Rastogi, P.; Ferretti, M.; Prato, M.; Krahne, R.; Manna, L. From $CsPbBr_3$ Nano-Inks to Sintered $CsPbBr_3$-$CsPb_2Br_5$ Films via Thermal Annealing: Implications on Optoelectronic Properties. *J. Phys. Chem. C* **2017**, *121* (21), 11956–11961.

(272) Tang, J.; Kemp, K. W.; Hoogland, S.; Jeong, K. S.; Liu, H.; Levina, L.; Furukawa, M.; Wang, X.; Debnath, R.; Cha, D.; Chou, K. W.; Fischer, A.; Amassian, A.; Asbury, J. B.; Sargent, E. H. Colloidal-Quantum-Dot Photovoltaics Using Atomic-Ligand Passivation. *Nat. Mater.* **2011**, *10* (10), 765–771.

(273) Tang, J.; Brzozowski, L.; Barkhouse, D. A. R.; Wang, X.; Debnath, R.; Wolowiec, R.; Palmiano, E.; Levina, L.; Pattantyus-Abraham, A. G.; Jamakosmanovic, D.; Sargent, E. H. Quantum Dot Photovoltaics in the Extreme Quantum Confinement Regime: The Surface-Chemical Origins of Exceptional Air- and Light-Stability. *ACS Nano* **2010**, *4* (2), 869–878.

(274) Rabenau, A.; Rau, H. Über Sulfidhalogenide Des Bleis Und Das Pb_4SeBr_6. *Zeitschrift für Anorg. und Allg. Chemie* **1969**, *369* (3–6), 295–305.

(275) German, R. M.; Rabin, B. H. Enhanced Sintering through Second Phase Additions. *Powder Metall.* **1985**, *28* (1), 7–12.

(276) Zovas, P. E.; German, R. M.; Hwang, K. S.; Li, C. J. Activated and Liquid-Phase Sintering—Progress and Problems. *J. Miner. Met. Mater. Soc.* **1983**, *35* (1), 28–33.

(277) Zhang, H.; Dasbiswas, K.; Ludwig, N. B.; Han, G.; Lee, B.; Vaikuntanathan, S.; Talapin, D. V. Stable

Colloids in Molten Inorganic Salts. *Nature* **2017**, *542* (7641), 328–331.

(278) Toso, S.; Toso, S.; Akkerman, Q. A.; Martín-García, B.; Prato, M.; Zito, J.; Infante, I.; Infante, I.; Dang, Z.; Moliterni, A.; Giannini, C.; Bladt, E.; Lobato, I.; Ramade, J.; Bals, S.; Bals, S.; Buha, J.; Spirito, D.; Mugnaioli, E.; Gemmi, M.; Manna, L.; Gemmi, M. Nanocrystals of Lead Chalcohalides: A Series of Kinetically Trapped Metastable Nanostructures. *J. Am. Chem. Soc.* **2020**, *142* (22), 10198–10211.

(279) Snyder, G. J.; Toberer, E. S. Complex Thermoelectric Materials. *Nat. Mater.* **2008**, *7* (2), 105–114.

(280) Kovalenko, M. V; Spokoyny, B.; Lee, J. S.; Scheele, M.; Weber, A.; Perera, S.; Landry, D.; Talapin, D. V. Semiconductor Nanocrystals Functionalized with Antimony Telluride Zintl Ions for Nanostructured Thermoelectrics. *J. Am. Chem. Soc.* **2010**, *132* (19), 6686–6695.

(281) Liu, Y.; Zhang, Y.; Ortega, S.; Ibáñez, M.; Ho Lim, K.; Grau-Carbonell, A.; Martí-Sánchez, S.; Ming Ng, K.; Arbiol, J.; V. Kovalenko, M.; Cadavid, D.; Cabot, A. Crystallographically Textured Nanomaterials Produced from the Liquid Phase Sintering of BixSb2–XTe3 Nanocrystal Building Blocks. *Nano Lett.* **2018**, *18* (4), 2557–2563.

(282) Ibáñez, M.; Zamani, R.; LaLonde, A.; Cadavid, D.; Li, W.; Shavel, A.; Arbiol, J.; Morante, J. R.; Gorsse, S.; Snyder, G. J.; Cabot, A. $Cu_2ZnGeSe_4$ Nanocrystals: Synthesis and Thermoelectric Properties. *J. Am. Chem. Soc.* **2012**, *134* (9), 4060–4063.

(283) Xu, B.; Agne, M. T.; Feng, T.; Chasapis, T. C.; Ruan, X.; Zhou, Y.; Zheng, H.; Bahk, J. H.; Kanatzidis, M. G.; Snyder, G. J.; Wu, Y. Nanocomposites from Solution-Synthesized PbTe-BiSbTe Nanoheterostructure with Unity Figure of Merit at Low-Medium Temperatures (500-600 K). *Adv. Mater.* **2017**, *29* (10).